Politechnika Wrocławska

FIELD OF SCIENCE: Natural Sciences

DISCIPLINE OF SCIENCE: Physical Sciences

DOCTORAL DISSERTATION

Determination of the Exciton Fine Structure in Two-Dimensional Metal-Halide Perovskites

Ms. Katarzyna Posmyk, MSc., Eng.

Supervisors:
Dr hab. inż. Michał Baranowski, associate professor
Prof. dr Paulina Płochocka

Keywords: Semiconductors, 2D materials, Perovskites, Metal-Halide Perovskites, 2D perovskites, Excitons, Exciton Fine Structure.

WROCŁAW 2025

THÈSE

En vue de l'obtention du

DOCTORAT DE L'UNIVERSITÉ DE TOULOUSE
Spécialité : Physique de la Matière

Présentée et soutenue par
Katarzyna Posmyk

Determination of the Exciton Fine Structure in Two-Dimensional Metal-Halide Perovskites

---

Ecole doctorale : Science de la Matière
Unité de recherche : Laboratoire National des Champs Magnétiques Intenses
Directeurs de Thèse : Paulina PŁOCHOCKA, Michał BARANOWSKI

Determination of the Exciton Fine Structure in Two-Dimensional Metal-Halide Perovskites

Abstract:

In recent years, two-dimensional (2D) hybrid lead halide perovskites emerged as an interesting alternative for optoelectronic and photovoltaic applications. Due to both quantum and dielectric confinement, the exciton binding energy in these materials is greatly enhanced and can reach up to a few hundreds of milielectronvolts. This makes 2D perovskites attractive objects for the investigation of exciton physics, since all excitonic effects are greatly enhanced in this system. It also results in significant splitting of states within the exciton fine structure, which can have a dramatic impact on the performance of light emitters or other devices based on these 2D materials.

Using polarisation-resolved optical spectroscopy techniques combined with the use of an external magnetic field, the exciton fine structure was investigated. The study was performed on a series of archetypical 2D perovskite compounds $(\mathrm{PEA})_2(\mathrm{MA})_{n-1}\mathrm{Pb}_n\mathrm{I}_{3n+1}$ with an increasing number of octahedra layers n within a slab, *i.e.* increasing width of the quantum well.

For the compound with n=1 the full exciton fine structure was revealed, including the dark state. The energy ordering and spacing between the states was determined, providing strong experimental evidence and resolving the ongoing dispute in literature.

Further magneto-optical studies on the perovskite compounds with n=2, 3 and 4 shown the evolution of the energy of the bright *in plane*-oriented excitonic states with respect to the magnetic field. This allowed extracting the values of the bright excitonic g-factors, as well as the values of the diamagnetic shift with respect to the number of inorganic layers.

The results presented in this work provide valuable information about the evolution of the optoelectronic properties of 2D perovskites when passing from 2D to 3D limit, as the quantum well thickness increases. These findings serve as a solid benchmark for theoretical modelling of phenomena in 2D perovskites. It also contributes to better understanding of the properties of these fascinating materials.

Keywords: Semiconductors, 2D materials, Perovskites, Metal-Halide Perovskites, 2D perovskites, Excitons, Exciton Fine Structure.

Wyznaczenie Struktury Subtelnej Ekscytonu w Dwuwymiarowych Perowskitach typu Metal-Halogen

Abstrakt:

W ostatnich latach dwuwymiarowe (2D) hybrydowe perowskity typu metal-halogen pojawiły się jako interesująca alternatywa dla zastosowań optoelektronicznych i fotowoltaicznych. Dzięki silnemu uwięzieniu kwantowemu i dielektrycznemu (ang. *quantum and dielectric confinement*) energia wiązania ekscytonu w tych materiałach jest znacznie zwiększona i może osiągać wartości rzędu kilkuset milielektronowoltów. Czyni to 2D perowskity atrakcyjnym obiektem badań fizyki ekscytonów, ponieważ wszystkie efekty związane z tymi kwazicząstkami są w tym układzie silnie wzmocnione. Prowadzi to również do istotnego rozszczepienia stanów w strukturze subtelnej ekscytonu, co może mieć kluczowy wpływ na działanie emiterów światła oraz innych urządzeń opartych na tych specyficznych materiałach 2D.

Za pomocą technik spektroskopii optycznej z rozdzielczością polaryzacyjną, w połączeniu z zastosowaniem zewnętrznego pola magnetycznego, w ramach niniejszej pracy zbadana została struktura subtelna ekscytonu. Badania przeprowadzono na serii archetypicznych związków perowskitowych 2D $(\mathrm{PEA})_2(\mathrm{MA})_{n-1}\mathrm{Pb}_n\mathrm{I}_{3n+1}$ o rosnącej liczbie warstw oktaedrów n w warstwie, *tj.* przy zwiększającej się szerokości studni kwantowej.

Dla związku o $n = 1$ wyznaczono pełną strukturę subtelną ekscytonu, w tym stan ciemny. Określono energie wszystkich stanów ekscytonowych oraz odstępy między nimi, dostarczając danych eksperymentalnych i tym samym rozstrzygając trwającą w literaturze dyskusję na ten temat.

Dalsze badania magneto-optyczne związków perowskitowych o $n = 2, 3$ i 4 wykazały ewolucję energii jasnych, zorientowanych w płaszczyźnie stanów ekscytonowych w zależności od pola magnetycznego. Pozwoliło to na wyznaczenie wartości g-czynników dla jasnych ekscytonów, a także wartości przesunięcia diamagnetycznego w funkcji liczby nieorganicznych warstw n.

Przedstawione w tej pracy wyniki dostarczają cennych informacji na temat ewolucji właściwości optoelektronicznych perowskitów 2D w przejściu od granicy 2D do 3D, wraz ze wzrostem grubości studni kwantowej. Stanowią one solidny punkt odniesienia dla modelowania zjawisk zachodzących w perowskitach 2D. Przyczyniają się także do lepszego zrozumienia właściwości tych fascynujących materiałów.

Słowa kluczowe: Półprzewodniki, Materiały 2D, Perowskity, Perowskity Metal-Halogen, Perowskity 2D, Ekscytony, Struktura Subtelna Ekscytonu.

Détermination de la structure fine des excitons dans les pérovskites bidimensionnelles aux halogénures métalliques

Abstract:

Au cours des dernières années, les pérovskites hybrides bidimensionnelles (2D) à base de plomb et d'halogènes ont émergées comme une alternative intéressante pour les applications optoélectroniques et photovoltaïques. En raison du confinement quantique et diélectrique, l'énergie de liaison des excitons dans ces matériaux est très élevée et peut atteindre plusieurs centaines de millielectronvolts. Cela rend les pérovskites 2D particulièrement attrayantes pour l'étude de la physique des excitons, puisque tous les effets excitioniques y sont considérablement amplifiés. Il en résulte également un important dédoublement des états au sein de la structure fine de l'exciton, ce qui peut avoir un impact déterminant sur les performances des émetteurs de lumière ou d'autres dispositifs basés sur ces matériaux 2D.

À l'aide de techniques de spectroscopie optique résolues en polarisation, combinées à l'utilisation d'un champ magnétique externe, la structure fine des excitons a été étudiée. L'étude a été menée sur une série de composés pérovskites 2D archétypaux de type $(\mathrm{PEA})_2(\mathrm{MA})_{n-1}\mathrm{Pb}_n\mathrm{I}_{3n+1}$, présentant un nombre croissant de couches d'octaèdres n dans une couche, c'est-à-dire une épaisseur croissante du puit quantique.

Pour le composé avec $n = 1$, la structure fine complète de l'exciton a été révélée, incluant l'état sombre. L'ordre énergétique et l'espacement entre les états ont été déterminés, à l'aide de solides preuves expérimentales et résolvant le débat en cours dans la littérature.

Des études magnéto-optiques complémentaires sur les composés pérovskites avec $n = 2, 3$ et 4 ont montré l'évolution de l'énergie des états excitioniques brillants, orientés dans le plan, en fonction du champ magnétique. Cela a permis d'extraire les valeurs des facteurs g des excitons brillants ainsi que celles du coéfficient diamagnétique en fonction du nombre de couches inorganiques.

Les résultats présentés dans ce travail apportent des informations précieuses sur l'évolution des propriétés optoélectroniques des pérovskites 2D lors du passage de la limite 2D à la limite 3D, à mesure que l'épaisseur du puit quantique augmente. Ces résultats constituent une référence solide pour la modélisation théorique des phénomènes dans les pérovskites 2D. Ils contribuent également à une meilleure compréhension des propriétés de ces matériaux fascinants.

Mots-clés: Semi-conducteurs, Matériaux 2D, Pérovskites, Pérovskites Halogénures de Plomb, Pérovskites 2D, Excitons, Structure Fine de l'Exciton.

Acknowledgements

I wish to express my sincere and heartfelt gratitude towards all of the people who contributed to the completion of my Ph.D. dissertation and helped me throughout the realisation of my doctoral programme. I wholeheartedly appreciate the support I received along the way, facing many challenges and obstacles.

I am deeply grateful to my supervisors, **Michał Baranowski** and **Paulina Płochocka**, for their guidance, mentorship and many inspiring discussions we shared. Thank you for all your efforts during this time, for all the opportunities I received, and for helping me grow as a scientist and as a person.

My thanks also go to the members of my research group. Your help was invaluable in carrying out numerous tasks and overcoming difficulties. Thank you for keeping me company during this journey and for many insightful discussions. Sharing both the laboratory and the office space with you was a pleasure and I am glad to have the opportunity to work alongside you.

I also wish to acknowledge the research groups of Prof. William A. Tisdale, Prof. Adam Babiński, Prof. Maciej Molas and Prof. Mirosław Mączka for succesful collaboration, welcoming me in their laboratories and kindly sharing samples of materials for me to study. The results obtained thanks to these collaborations became part of this dissertation, which I greatly appreciate.

I am grateful to the engineers at LNCMI for their constant technical support, as well as the administration of the laboratory for helping me navigate the organisation of my stays in France.

I would like to sincerely thank my family and friends for their unwavering support throughout this journey. Especially I would like to thank my mom Urszula for inspiring me to pursue this challenge many years ago, for always believing in me and my abilities, even in times of doubt and hardships.

I acknowledge the NCN Sonata project: “Electronic properties and polaronic effects in lead halide perovskite nanoplatelets,” the French Government Scholarship for cotutelle PhD students, and the Polish-U.S. Fulbright Commission within the Junior Research Award Programme for financially supporting my research.

Lastly, I would like to thank my younger self, who decided to go through this experience in pursuit of growth and finding her own way.

List of Acronyms

1D	One-Dimensional
2D	Two-Dimensional
2DP	Two-Dimensional Perovskites
3D	Three-Dimensional
ACI	Alternating Cations in the Interlayer Space phase
BA	Buthylamine, Buthylammonium cation
CB	Conduction Band
CBM	Conduction Band Minimum
CD	Circular Dichroism
CW	Continuous Wave
DJ	Dion–Jacobson phase
DOLP	Degree of Linear Polarization
eV	electronvolts
FA	Formamidine, Formamidinium cation
FSS	Fine Structure Splitting
FX	Free Exciton
GaAs	Gallium Arsenide
HI	Hydroiodic Acid
$\mathbf{H_3PO_2}$	Hypophosphorous Acid
HWP	Half Wave Plate
LED	Light Emitting Diode
LHe	Liquid Helium
LN	Liquid Nitrogen
LO	Longitudinal Optical phonons
MA	Methylamine, Methylammonium cation

MAI	Methylammonium Iodide
meV	milielectronvolts
MHP	Metal-Halide Perovskites
PEA	Phenylethylamine, Phenylethylammonium cation
PEPI	Phenylethylammonium Lead Iodide
PbI_2	Lead Iodide (II)
PbO	Lead Oxide (II)
PL	Photoluminescence
QWP	Quarter Wave Plate
R	Reflectance
RD	Ruddlesden–Popper phase
RT	Room Temperature T=293 K
SOC	Spin-Orbit Coupling
TMD	Transition Metal Dichalcogenide
VB	Valence Band
VBM	Valence Band Maximum
X	Exciton
XRD	X-ray Diffraction
λ	Wavelength
π_x, π_y	Linear Polarisation
σ^+, σ^-	Circular Polarisation

Contents

Chapter 1

Metal-Halide Perovskites and their Two-Dimensional Derivatives

1.1 Metal-Halide Perovskites

Modern technologies and devices used worldwide, such as computers, sensors, or smartphones, are created on the basis of semiconducting materials. For this reason, a lot of research effort has been put into understanding the physics behind the properties of semiconductors, as well as the material development. Furthermore, the growing energy consumption and demand for electricity, together with the issues related to climate change and global warming, warrant a turn towards renewable energy sources. To combat these challenges, even better semiconductors need to be developed, leading to a constant search for novel, alternative materials.

Metal-halide perovskites (MHP) are a unique type of semiconducting material. In recent years, they have shown great promise for real-life optoelectronic applications, such as energy harvesting [Kojima 2009, Lee 2012, Green 2014, Jung 2015, Rong 2018, Liu 2023] and light emission [Fakharuddin 2022, Xiong 2023, Sun 2023, Yang 2023, Cao 2023, Xing 2024], becoming an object of extensive investigation. This progress was possible because of the specific set of properties displayed by MHP, which could make them superior in some areas to those of currently commercially used semiconductors.

The reason behind the vast amount of time and effort invested into perovskite research is an unprecedented development rate of devices constructed with MHP as an active region. More specifically, a perovskite-based solar cell has reached a conversion efficiency comparable to crystalline silicone, in a fraction of the time required to achieve this for the more mature, already well-developed technology (Fig. 1.1). This explosive progress rate has shown the enormous application potential of MHP and has led to extensive studies and the development of this specific group of semiconducting materials [Green 2014]. Improvement in fabrication methods, as well as optimisation of the process and variation in chemical composition, led to the obtaining of a cell conversion efficiency above 25 % (current record - **26.7 %**) [Kopidakis 2024, Green 2024, Liu 2019, Ma 2023]. Intense studies of these materials also led to the exploration of different potential applications of perovskites, such as light emitters and detectors [Chen 2018b]. Another example of a potential MHP application, due to a heavy metal cation present in the structure, is the development of perovskite scintillators [Moseley 2021, Wibowo 2023].

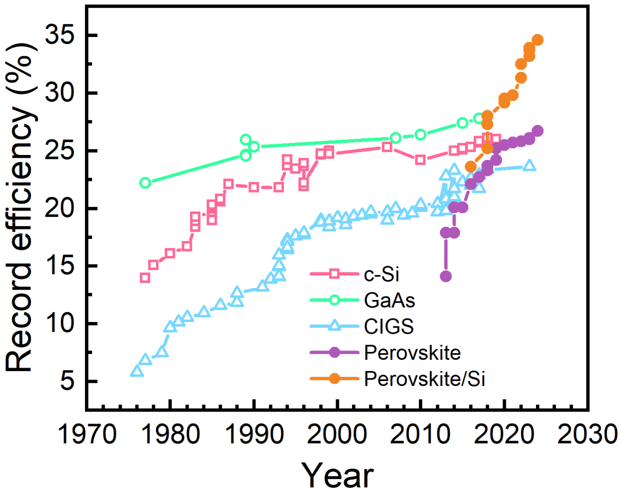

Figure 1.1: Conversion efficiencies of solar cells based on different materials in years 1977 - 2024. Adapted from [Kopidakis 2024].

All of these development directions take advantage of a unique set of perovskite properties, primarily a high yield and relatively short emission lifetimes (a few nanoseconds). In general, MHP display multiple properties attractive from the point of view of potential applications, such as:

- **direct band gap**, which allows efficient absorption and emission of light [Hoke 2015]. It is possible to tune the energy of the band gap over the whole visible region of the electromagnetic spectrum by adjusting the chemical composition of a perovskite (mainly halide ions)[Ou 2019]. This is especially attractive for the construction of devices, such as tandem solar cell, covering the broad spectral range [Liu 2024], as well as light emitting diodes [Fakharuddin 2022, Xiong 2023];

- **fabrication by chemical synthesis** - relatively lower in cost and the energy consumption, which are required, for example, for Czochralski's method or epitaxial methods. Due to the complex apparatus systems required in such methods, generating extreme process conditions, epitaxy is an extremely costly procedure. Moreover, the chemical synthesis process is faster than epitaxial growth, which is an advantage when it comes to mass-scale fabrication. Furthermore, perovskite synthesis does not require lattice constant matching between the substrate and the grown material, as it is a very important problem to consider otherwise [Zheleva 1994, Bett 1999]. This enables placing the perovskite materials on various types of substrates, such as glass or flexible foils [Gao 2022, Li 2022, Tian 2024], which extends the scope of possible applications;

- **defect tolerance** - devices based on MHP exhibit surprisingly high efficiency, despite the fact that the fabrication via chemical synthesis usually introduces the defects to the crystal structure. In addition, perovskites are usually placed in the device in the form of a polycrystalline film, with a grain size in a range of 1-100 μm. Both of these facts point to rather poor structural quality, and yet perovskites perform well in terms of optoelectronics. Often times they are called *"defect tolerant materials"*, where defect states form within the electronic bands or near their edges, instead of states located deep within the band gap [Brandt 2015, Ball 2016, Brandt 2017, Kim 2020].

All of these intriguing properties of MHP point to the potential of devices based on these materials. Not only they are cheaper to produce, but the relative ease of adaptation for various applications makes perovskites very attractive novel materials. Moreover, direct band gap and efficient light absorption mean that the active perovskite layer can be thin, opening doors for a wide range of applications unattainable for traditional semiconductors, such as semi-transparent and flexible photovoltaic panels [Li 2022], which can be integrated into windows and building facades easier than those of silicone ones.

Research into perovskite materials explores multiple directions, both very application-orientated and more fundamental. MHP have been shown to be extremely interesting and significantly different from more commonly known "classical" materials such as sillicone, gallium nitride, or gallium arsenide. Perovskite crystals are ionic, not covalently bound, and approximately 10 times softer than crystalline silicone (20 GPa for perovskites [Spina 2017] vs 130-188 GPa for sillicone [Hopcroft 2010]). The soft, ionic nature of perovskites leads to the strong interactions of charge carriers and vibrations of the crystal lattice. It shapes the optical response and strongly influences their optoelectronic properties [Wright 2016, Buizza 2021].

Another branch of perovskite research turns towards their structural derivatives. There are multiple types of perovskite materials of lowered dimensionality, starting from two-dimensional (2D), "planar" structures [Pedesseau 2016], through one-dimensional (1D) nanoribbons [Kamminga 2016], all the way to zero-dimensional (0D) perovskite quantum dots [Protesescu 2015], showing prominent confinement effects. The object of this work is a 2D perovskite compound, studied in a context of its fundamental physical properties. Due to significant spatial and dielectric confinement, 2D perovskites are a material system where charge carriers form strongly bound excitons, existing all the way from cryogenic to room temperatures and above. They provide an excellent framework for studying the physics of excitons, as all of the effects are prominent and are relatively easily observable in experiments. However, it was shown that this type of structure can also be used successfully in multiple optoelectronic devices, such as solar cells (with stability in ambient conditions superior to three-dimensional (3D) perovskites [Smith 2014, Liao 2017], field effect transistors [Kagan 1999, Matsushima 2016], photodetectors [Tan 2016], or light-emitting diodes (LEDs) [Yuan 2016, Liang 2016]. 2D perovskites (2DP) display all of the perovskite qualities described above and present even more ways to structurally alter their optical properties, pushing material engineering to a level unattainable in the case of epitaxial semiconductors. Moreover, 2DP have shown improved stability under ambient conditions, which is a crucial aspect for any perovskite-based devices [Wygant 2019, Schlipf 2019].

In order to effectively harness the enormous potential of perovskite materials, it is crucial to understand the physical processes behind the extraordinary performance. Furthermore, studying MHP on a fundamental level provides insight into a system vastly different from the well-established classical semiconductors, forcing different approaches and modification of models describing physical phenomena occurring within.

1.1.1 Crystal Structure of Metal-Halide Perovskites

The term "perovskite" refers to a wide variety of materials, all of which share a characteristic crystal structure shown in Fig. 1.2 (a). They are described by a general chemical formula ABX_3, where A and B denote, respectively, monovalent and bivalent cations, and X is a monovalent anion – oxygen or halogen. B cation is surrounded by halide ions, forming octahedra-shaped units (Fig. 1.2 (b)), with a small cation A filling the space between them.

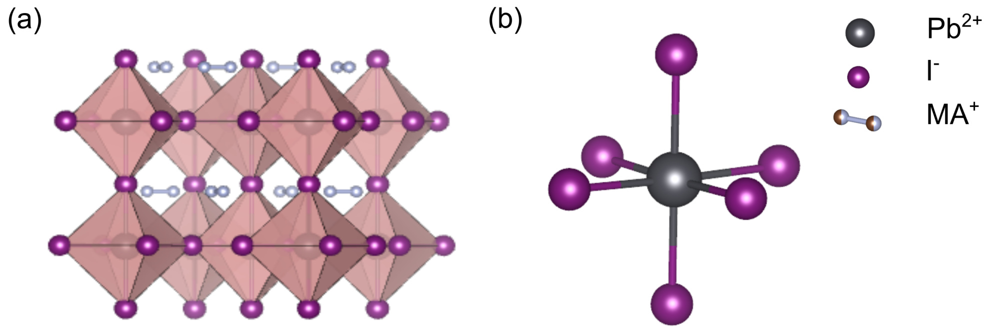

Figure 1.2: (a) Crystal structure of a typical representative of 3D perovskite methylammonium lead iodide $MAPbI_3$. (b) Single octahedron unit composed of lead and iodine ions. Visualised using VESTA software [Momma 2011] using crystallographic data after [Dang 2015]. Hydrogen atoms omitted for clarity.

In the case of MHP, the cation in position A is usually a small organic molecule, such as methylammonium (MA^+) or formamidinium (FA^+), or an inorganic cation such as caesium (Cs^+). The cation in position B is usually a bivalent lead (Pb^{2+}) or tin (Sn^{2+}), while an anion in position X is a halogen - iodine, bromine, or chlorine (I^-, Br^-, Cl^-).

The structural stability of a perovskite crystal is defined by the *Goldschmidt tolerace factor t* [Goldschmidt 1927], defined as:

$$t = \frac{(R_A + R_B)}{\sqrt{2}(R_B + R_X)}, \tag{1.1}$$

as well as the octahedral factor μ [Li 2008]:

$$\mu = \frac{R_B}{R_A}, \tag{1.2}$$

where:

$R_{A/B/X}$ – radii of the A,B and X ions, respectively.

In order to obtain a stable perovskite structure, the parameters mentioned above need to be in the range [Li 2008]:

$$0.8 \leq t \leq 1.0, \quad 0.44 \leq \mu \leq 0.9 \tag{1.3}$$

These factors provide constraints on the size of possible building blocks of a perovskite material. It is especially relevant in case of the cation in the A position – in simple terms, a molecule in this position needs to be small enough to fit in between the octahedra units, otherwise the perovskite structure cannot be sustained. For example, in the case of lead iodide compounds, the limit on the radius of the cation at the A site is 2.6 Å [Mitzi 2001]. However, placing a molecule that is too large in that position may also be intentional and lead to the creation of derivative crystal structures. This particular case is a way to create 2D perovskites, as well as other derivatives.

1.1.2 Two-Dimensional Perovskites

The structure of a 2D perovskite can be conceptually derived from a 3D, “bulk” case. This kind of structure forms when the cation in position A is too large to fit between the octahedra cages and to meet the Goldschmidt tolerance factor (Eq. 1.1, as shown in Fig. 1.3). The crystal structure can no longer be sustained, and it results in formation of layers of octahedral units, surrounded from both sides by large organic cations. These additional organic molecules are inherently hydrophobic, which shields the octahedral units from the ambient conditions. It is quite a significant feature, as perovskites are generally prone to degradation under atmospheric conditions (especially humidity is a factor) due to the instability of the cations of Pb^{2+} or Sn^{2+} [Philippe 2015, Leijtens 2017, Lanzetta 2021]. The presence of a large organic *spacer* counteracts this issue and renders the 2D perovskite structure more stable [Yang 2018, Wygant 2019, Liu 2019, Vasileiadou 2021a, Vasileiadou 2021b, Zhao 2022].

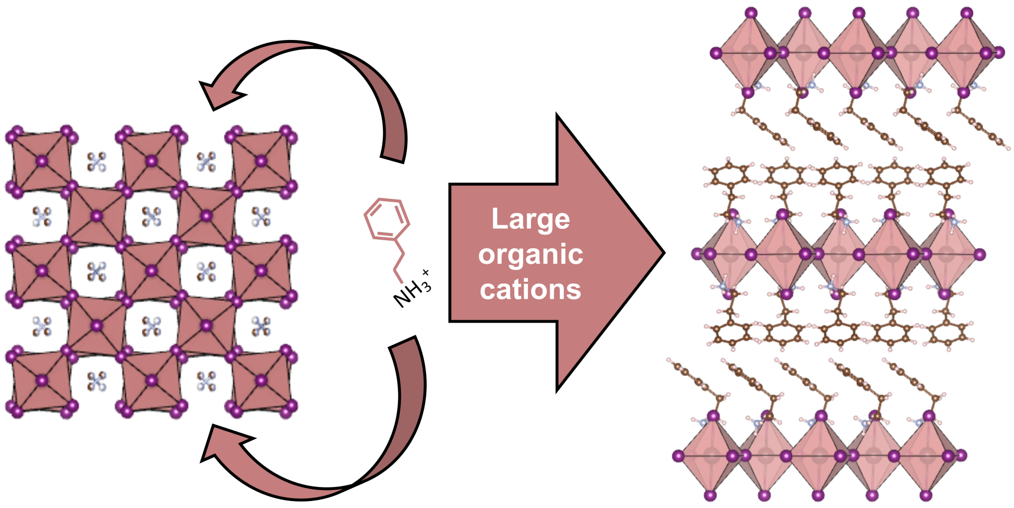

Figure 1.3: Schematic presentation of transition from bulk, 3D structure to 2D system, obtained by placing a large organic molecule in the spaces between octahedra units (A-site cation).

In general, 2D perovskites can be described as n layers of organic-inorganic octahedra surrounded from both sides by organic spacers [Mao 2018b]. Such a structure is periodic in a direction perpendicular to the plane of octahedra layers. The choice of a large organic component is very broad; many different cations have been reported to form a stable 2D perovskite structure. The size restrictions are not as rigorous as in the case of 3D perovskites: the organic ligand must fit between corner-sharing octahedral units, but rather than the size of the functional group -NH_3^+, more important is its positive charge and ability to form hydrogen bonds [Mao 2018b]. There are many molecules that fulfil this criteria, so there are many possibilities of forming a stable 2D perovskite structure. It is yet another way to adjust the properties of the material, as these varying cations lead to the formation of several compounds [Li 2021].

1.1.3 Types of 2D Perovskites

The most commonly found structures of 2D perovskites are the so-called <100>-oriented, categorised by the crystallographic plane of the original 3D structure, where the large organic cation separates the octahedra. Among the <100>-oriented 2D perovskites, three phases can be distinguished (Fig. 1.4):

- **Ruddlesden-Popper** (RP) [Ruddlesden 1957, Ruddlesden 1958], shown in the Fig. 1.4 (a); each inorganic octahedra layer is separated by two organic ligand molecules, each of them bound to a different octahedra layer; between organic cations there are only weak van der Waals interactions, no rigid binding. The octahedral units in the adjacent layers are shifted by half of a unit cell. The organic cations in this phase can be quite long. Typical representatives of this phase are phenylethylammonium (PEA) lead iodide or buthylamonnium (BA) lead iodide, further discussed in the section 1.1.3.1.

- **Dion-Jacobson** (DJ) [Dion 1981, Jacobson 1985], shown in the Fig. 1.4 (b); each organic cation is bound to two neighbouring inorganic octahedra layers; organic part is usually shorter than in the case of RP phase. In this case, inorganic layers are stacked exactly on top of each other, as opposed to the RP phase. An example of a 2D perovskite in the DJ phase is 3-(aminomethyl)piperidinium (3AMP) methylammonium lead iodide [Mao 2018a].

- **Alternating cations in the interlayer space** (ACI) [Soe 2017], shown in Fig. 1.4 (c); novel type of structure, combining the characteristics of RP and DJ phases. As the name suggests, two types of organic cations occupy the interlayer space between inorganic units, in the alternating way. A reported example of such structure is guanidinium methylammonium lead iodide. Compared to the RP phase, ACI displays different stacking motif and higher symmetry.

The RP phase is the most commonly found and used in optoelectronic applications [Chen 2018b]. It is also the one studied within this work; hence all further remarks and descriptions will refer to this specific phase, unless otherwise stated.

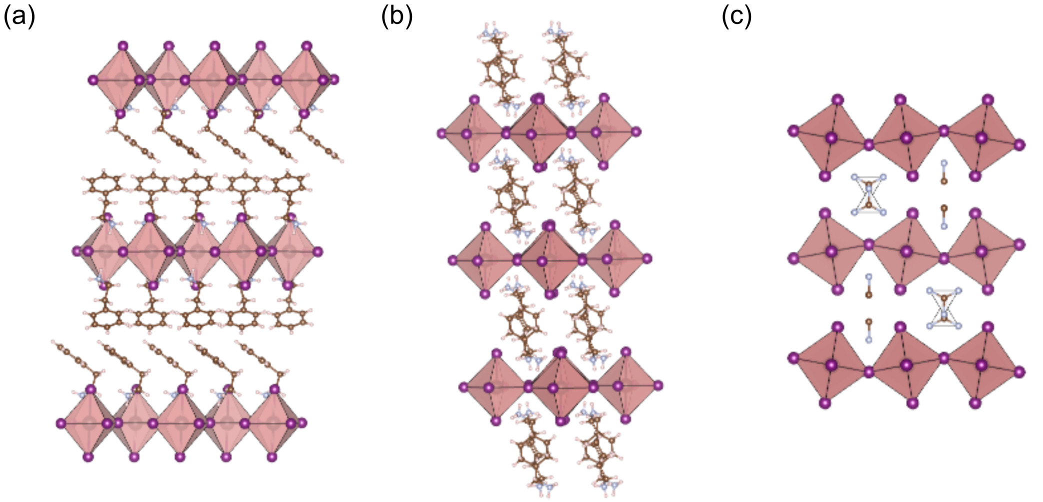

Figure 1.4: Models of crystal structure of 2D perovskites in three different phases: (a) Ruddlesden–Popper [Du 2017], (b) Dion–Jacobson [Fu 2023] and (c) alternating cations in the interlayer space [Soe 2017]. All models visualised using VESTA software [Momma 2011].

1.1.3.1 Ruddlesden-Popper Phase – van der Waals Crystals

The general chemical formula describing the 2D perovskite in RP phase is $L_2A_{n-1}B_nX_{3n+1}$, where L - large organic molecule (*spacer*, typically buthylammonium, BA, or phenylethylammonium, PEA), A is a small organic cation (typically methylammonium, MA, or formamidinium, FA), B denotes the bivalent metal cation (lead Pb^{2+} or tin Sn^{2+}), X denotes the halide anions and n denotes the number of octahedra layers $[MX_6]^{4-}$. A schematic of such a crystal structure is shown in Fig. 1.5, for n in the range from 1 to 4.

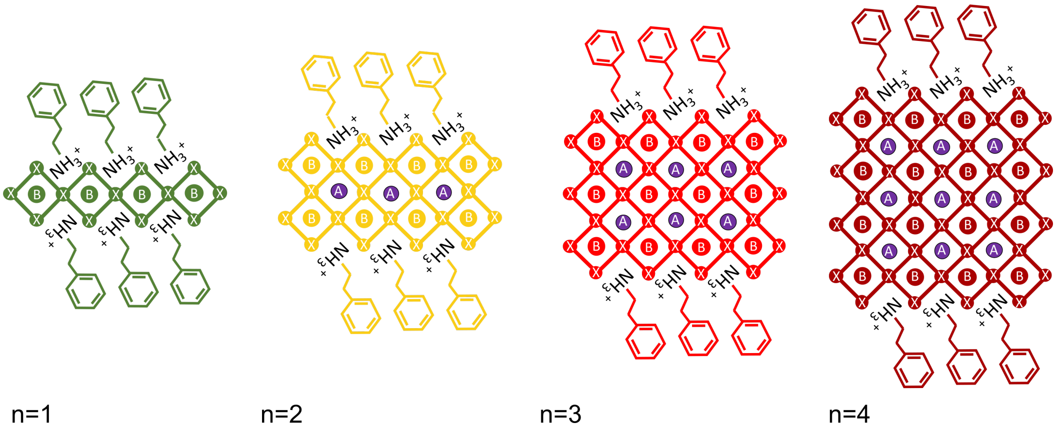

Figure 1.5: Schematic of 2D perovskite structure with the varying number of the inorganic octahedra layers n.

It is important to note that the *spacer* molecules between two adjacent layers interact with each other only through van der Waals interactions, making 2D perovskites in RP phase van der Waals crystals. As such, it is possible to mechanically exfoliate them [Niu 2014] and stack them with any layered material of the van der Waals family (such as transition metal dichalcogenides, TMDs), creating heterostructures with exciting new properties [Yang 2019, Wang 2020, Karpińska 2022].

1.1.4 Tuning the Perovskite Properties by Modification of the Materials' Chemical Composition

The unprecedented extent of possible modification and adjustment of the properties of MHP has pushed the envelope in the design of semiconductor-based devices. The relative ease of these modifications stems directly from the perovskite structure and the fact that it is fabricated by wet-chemistry methods. These materials have a direct band gap, which can be manipulated by controlling the content of appropriate halide anions (I-Br, Br-Cl) (Fig. 1.6 (a) [Ou 2019]) or choosing between lead or tin cation [Gao 2014].

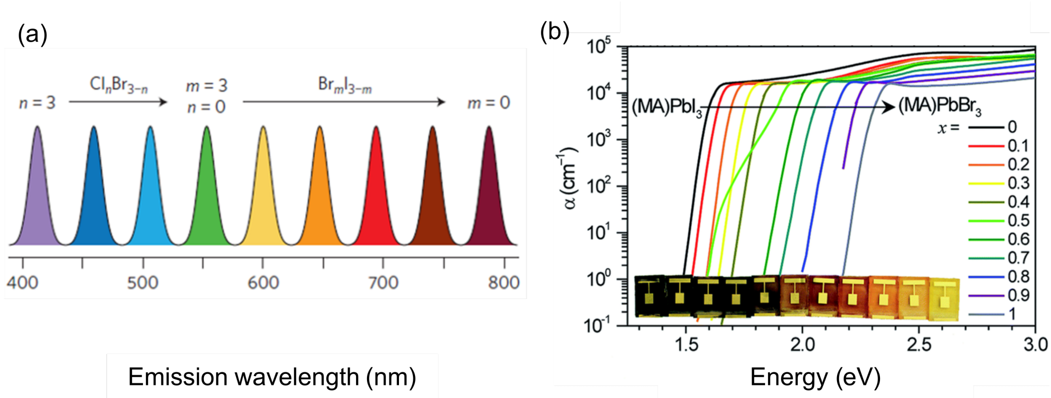

Figure 1.6: (a) Tunability of the wavelength of photons emitted by perovskite depending on the content of a given halide anion, covering the entire visible range of electromagnetic spectrum. Adapted from [Ou 2019]. (b) Absorption coefficient of the representative perovskite $(MA)Pb(Br_xI_{1-x})_3$ for a variable parameter x denoting the bromine content in the structure. Adapted from [Hoke 2015].

As shown in Fig. 1.6 (b), MHP show strong absorption of electromagnetic radiation, with the absorption coefficient reaching values above $10^4\,\mathrm{cm}^{-1}$ already for energies of 0.1 eV above the energy gap [Hoke 2015]. With increasing bromine and then chlorine content, the energy gap shifts from near infrared to ultraviolet, covering the entire visible range of electromagnetic radiation (390 - 790 nm range, which can be further extended to near infrared by substituting the lead cation with a tin cation at the position B [Sutherland 2016]). A direct band gap means that a perovskite active layer as thick as 500 nm absorbs almost 100% of incident light. This fact coupled with the ease of tuning the gap is the main reason why MHP are attractive from the point of view of optoelectronic applications.

Perovskites often undergo temperature-dependent phase transitions [Poglitsch 1987, Baikie 2013]. In many cases, perovskite structure has a very high, cubic symmetry at higher temperatures, which gets lower as the temperature goes down [Whitfield 2016, Galkowski 2017, Chen 2018a]. For example, in the case of a staple perovskite material – methylethylammonium lead iodide, $MAPbI_3$ – its crystal structure is cubic above 330 K, then transitions to tetragonal phase. Further cooling leads to another phase transition around 160 K, where the structure becomes orthorhombic [Poglitsch 1987, Whitfield 2016]. Schematic of this process is shown in Fig. 1.7. The symmetry of the crystal has a dramatic impact on the optoelectronic properties of a perovskite material. This is not surprising considering the fact that perovskite crystals are ionic, which leads to non-uniform local charge distribution.

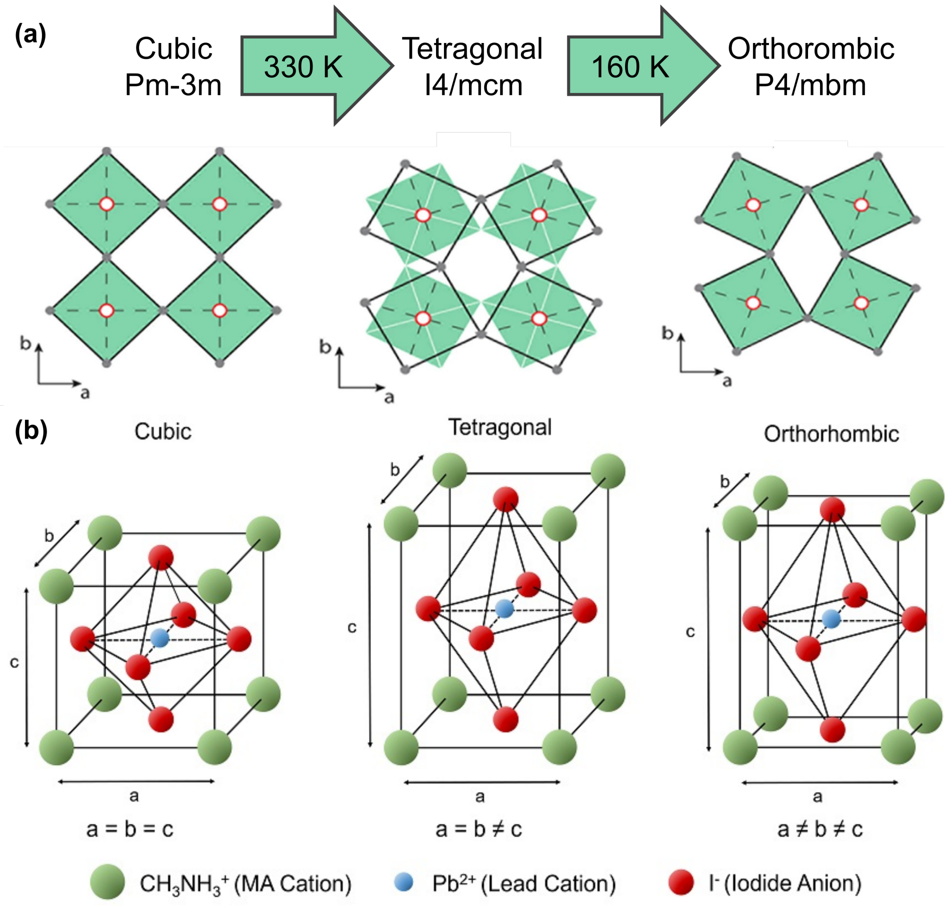

Figure 1.7: (a) Schematic of a phase transition process occuring in a perovskite structure with decreasing temperature, shown on an example of $MAPbI_3$ compound. Adapted from [Whitfield 2016]. (b) Unit cells of perovskite $MAPbI_3$ structure in different phases. Adapted from [Thomson 2018].

Another way of influencing the properties of MHP is by modifying the organic part of the lattice, typically the molecules in position A of the structure. The deliberate choice of molecules that are too large to meet the Goldschmidt tolerance factor (Eq.,1.1) may lead to the formation of perovskite derivative structures of lower dimensionality, such as 2D perovskites. Moreover, adjusting the conditions of the synthesis process and mediating the precipitation rate of ions (by adding organic ligands) leads to the formation of perovskite nanocrystals of various morphology, for example: cube-shaped [Protesescu 2015, Akkerman 2018], pseudo-spheroidal [Akkerman 2022] or nanoplatelets [Akkerman 2016, Weidman 2016, Otero-Martínez 2022], where size-confinement effects play an important part and allow for even further fine-tuning of optoelectronic properties.

In case of 2D perovskites, it is possible to modify the optoelectronic properties of the material in even more ways than in 3D perovskites, allowing for even more precise tailoring for the current needs. For example, by changing the number of inorganic octahedra layers n in a structure, one can tune the width of the quantum wells, effectively changing the optical and electronic band gap (Fig. 1.8, [Blancon 2018]). This is possible by adjusting the amount of reagents during the synthesis process [Paritmongkol 2019].

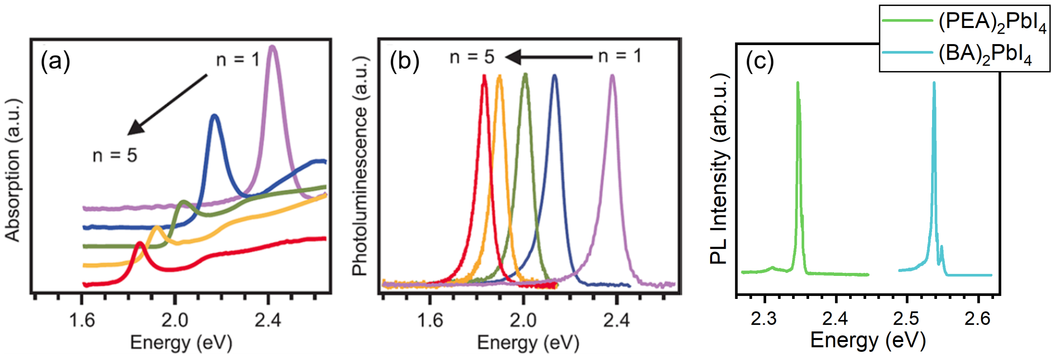

Figure 1.8: Optical spectra of (a) absorption and (b) photoluminescence for a 2D perovskite $(BA)_2(MA)_{n-1}PbI_{3n+1}$ for n in a range from 1 to 5, showing the red-shift of the optical transition with the increasing number of layers. Adapted from [Blancon 2018]. (c) Optical absorption spectra of 2D perovskites $(PEA)_2PbI_4$ and $(BA)_2PbI_4$, illustrating the influence of the dielectric environment of the quantum well (i.e., influence of a *spacer* choice) on the band gap.

Another "tuning knob" enabling the modification of properties in these materials is the choice of the large organic cation. A variety of potential *spacers* has been shown to form a stable 2D perovskite structure [Li 2021]. The ability to tune the excitonic properties comes from the change in the dielectric environment provided by the organic part. By changing the *spacer*, it is possible to control the band gap of the material and consequently, the emission energy (Fig. 1.8 (c), [Hong 1992]).

Interestingly, due to the soft, ionic nature of the perovskite lattice, the choice of organic molecule can impact the properties of 2D perovskites in yet another way – by influencing the octahedral distortion, which directly impacts the band structure of the perovskite material [Knutson 2005]. A schematic of the distortion of perovskite octahedral units is shown in Fig. 1.9. In the case of the inorganic lead iodide framework, the cross-sectional area between octahedral units is approximately 40 Å^2 [Mitzi 2001]; If the area of the organic ligand is smaller than that, the structure can accommodate the difference by tilting the octahedral units. Buthylammine is an example of such a small molecule, as it is aliphatic with a simple, relatively short, hydrocarbon chain. Hence a good example of a 2D perovskite with a significantly distorted structure is buthylammonium lead iodide $(BA)_2PbI_4$ (Fig. 1.9 (a)).

The way to assess the magnitude of the distortion is to quantify the specific angles defined within the crystal structure (shown in Fig. 1.9 (b)): β, an angle between the Pb-I-Pb bonds between the corner-sharing octahedra, defines the in-plane distortion. δ, an angle between the Pb-I bond and the normal to the 2D plane, defines the out-of-plane distortion. The distortions influence the overlap between the atomic orbitals, shaping the band structure of the material. As a consequence, by choosing the appropriate cation it is possible to tune the band gap of the perovskite [Hong 1992], the effective mass of charge carriers [Dyksik 2020, Peksa 2024] and even the exciton - phonon interaction [Straus 2016, Ni 2017]. Often, the choice of *spacer* will determine whether or not there will be a temperature-dependent phase transition present in the structure, which influences its symmetry [Billing 2007, Lemmerer 2012, Billing 2008].

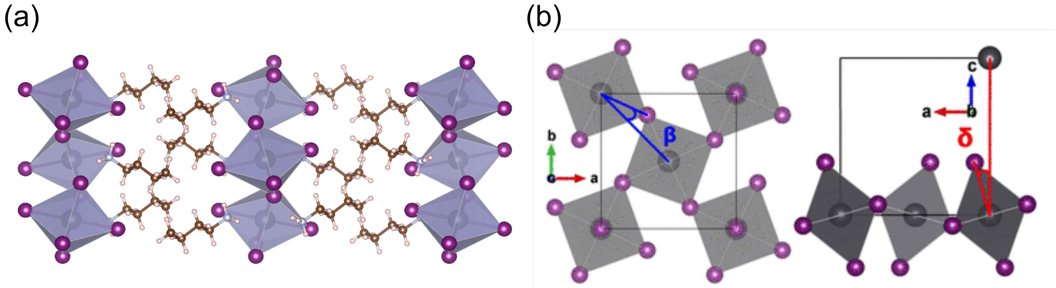

Figure 1.9: (a) Model of a crystal structure of 2D perovskite $(BA)_2PbI_4$ in low temperature, orthorombic phase. This compound displays significant octahedral distortions. Visualised using VESTA software [Momma 2011] with the crystallographic data after [Menahem 2021]. (b) Schematic showing the definition of two distortion angles, β and δ, commonly used to assess the octahedral distortion in and out of 2D plane of the crystal. Adapted from [Pedesseau 2016].

A very interesting case of tuning the properties of 2D perovskites is an incorporation of chiral organic molecules as *spacers* [Ahn 2017]. So-called *chiral MHP* became of interest in recent years due to their unique optoelectronic properties. Such addition introduces helical distortions to the inorganic framework, effectively transferring the chiral property from the organic sublattice [Jana 2020, Lu 2020]. This results in distinct circular dichroism, which is a valuable trait for applications. For example, chiroptical ability allows for the detection of circularly polarised light [Chen 2019].

All in all, the 2D perovskites are a very interesting material group for further study. They are more stable in the ambient conditions compared to the 3D perovskites, due to the presence of large, hydrophobic organic molecules in their crystal structure, effectively shielding the inorganic framework [Wygant 2019].

1.2 Band Structure of Metal-Halide Perovskites

MHPs are semiconductors with a direct energy band gap, which, depending on the crystal symmetry, can be present at different points of the Brillouin zone. For the cubic and tetragonal phase, it is located in the R point [Even 2013, Whitfield 2016] as shown in Fig. 1.10 (a). For the orthorhombic phase it is present in the M point [Whitfield 2016, Quarti 2020], and in the case of the low-symmetry 2D perovskites, in the Γ point [Tanaka 2005, Quarti 2024] (Fig. 1.10 (a)). However, qualitatively, the band structure near the band gap does not vary across all these different phases. Often the MHP band structure is called “inverted” when compared to the III-V compounds, because of the reversed order of one s-type and three p-type states, which form the conduction band.

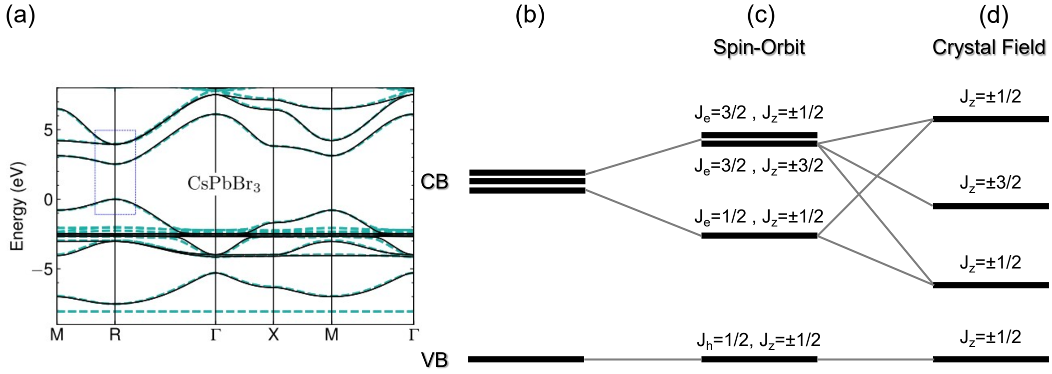

Figure 1.10: (a) Band structure calculated for $CsPbBr_3$ in a cubic phase, showing a direct band gap in the R point of the Brillouin zone. Adapted from [Kirstein 2022a]. (b) Character (s-like or p-like) of valence and conduction bands. (c) Spin-orbit coupling leads to splitting of the electronic states with different angular momentum J_e, into lower ($J_e=\pm1/2$) and upper band ($J_e=\pm3/2$). (d) Influence of the crystal field on the band structure, further splitting electronic states with z-components of the angular momentum $J_z=\pm1/2$ and $J_z=\pm3/2$. Adapted from [Tanaka 2005].

The states at the band edge originate from the molecular orbitals of atoms forming $[BX_6]^{4-}$ octahedra units. The valence band is mainly composed of *s* orbitals from heavy metal B cations, hybridised with *p* orbitals from halide X anions (σ antibonding hybridised orbital). Because of that, the valence band has a mainly s-like character (singular band), where holes have total angular momentum $J_h = \pm1/2$. The conduction band consists of the metal *p* orbitals hybridised with halide *s* orbitals (σ antibonding and π antibonding orbitals) [Umebayashi 2003, Kirstein 2022a]. It has p-like character, with three bands present – light electrons, heavy electrons and spin-orbit coupled band (Fig. 1.10 (b)). Spin-orbit coupling (SOC) is strong in case of MHP, mainly due to the presence of heavy metal ions. SOC splits off the electronic states with total angular momentum $J_e = \pm1/2$ down in energy from the states with $J_e = \pm3/2$, to the conduction band edge (Fig. 1.10 (c)). Including the SOC effects in any band structure considerations is therefore imperative to correctly describe the perovskite optoelectronic properties [Even 2013]. Lowering the symmetry of the crystal structure, *e.g.* caused by a phase transition, introduces crystal field, which influences the band structure by further splitting in energy the electronic states with different z-components of the angular momentum J_z [Tanaka 2005] (Fig. 1.10 (d)).

1.3 Excitons in Two-Dimensional Perovskites

1.3.1 Classification of Excitons

An **exciton** is a quasiparticle consisting of an electron and a hole, bound by the Coulomb interaction. It is one of the most basic excitations in a perfect semiconductor. Excitons are electrically neutral quasiparticles, so they can transport energy without transporting the electrical charge. They can be created as a result of the absorption of a photon by the excitonic state or by band-to-band absorption and subsequent relaxation and binding of an electron and a hole. Depending on the material system, these quasiparticles can have significantly different properties. In particular, looking at the relation between exciton size, described by its wave function radius, and the size of the unit cell in the considered semiconductor, two types of excitons can be distinguished (Fig. 1.11):

- **Wannier-Mott**: loosely bound, spanning over multiple unit cells (hundreds of angstroms). It is possible to describe them using the effective mass model. In this approach, the exciton is similar to the hydrogen-like system and can be approximated as such. The small exciton binding energy (versus the hydrogen atom) is due to the screening effect: the exciton exists in a crystal, so the influence of the crystal lattice on the Coulomb interaction between carriers cannot be ignored. The environment is not a vacuum, so the relative dielectric constant ε is greater than 1. Wannier-Mott exciton is usually found in most inorganic, "classical" semiconductors (*e.g.* gallium arsenide, GaAs) [Wannier 1937, Mott 1938];

- **Frenkel**: confined in a range of couple unit cells, or a single molecule. Such excitons are strongly bound; large spatial confinement is present in such a system. As charge carriers are more localised, one needs to consider molecular orbitals (highest occupied - HOMO, and lowest unoccupied - LUMO) in this case. Typically found in materials with a relatively low dielectric constant, usually organic semiconductors and molecular crystals (*e.g.* halide salts, such as NaCl) [Frenkel 1931].

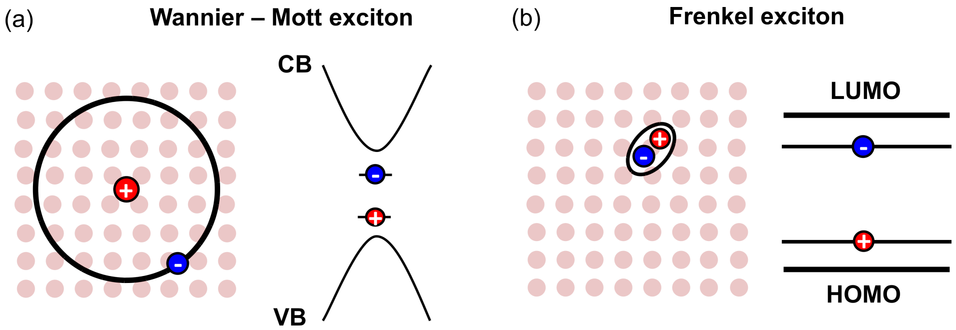

Figure 1.11: Schematic presentation of two kinds of excitons: (a) Wannier-Mott type, and (b) Frenkel type. Adapted from [Kéna-Cohen 2010].

1.3.2 Description of Wannier-Mott Excitons

Multiple models have been invoked to describe the motion of charge carriers and excitons in semiconductors. Among them, used successfully in the case of optical properties, is the so-called **effective mass model**. It simplifies the complex problem of charge carriers moving within a medium, by treating them as they were free particles with modified mass. In this way, including the relative dielectric permittivity of the material and the modified, effective mass accounts for the influence of the surrounding carriers, as well as the periodic potential of the crystal lattice.

Within the framework of the effective mass approximation, the Wannier-Mott type exciton – electron and hole correlated via Coulomb interaction – is modelled after the Bohr hydrogen atom, but instead of electron mass m_e, one uses the effective reduced mass of carriers, defined as:

$$\frac{1}{m_r^*} = \frac{1}{m_e^*} + \frac{1}{m_h^*} = \frac{m_e^* + m_h^*}{m_e^* m_h^*}. \tag{1.4}$$

where:

$m^*_{e/h}$ – effective masses of electrons and holes.

In the hydrogen atom problem, the positive charge – proton – is assumed to have an infinite mass, and electron is orbiting around it. In the case of an exciton, both carriers have more comparable masses, thus the movement of their centre of mass is considered instead, as well as the relative movement of electron and a hole.

This problem can be described in an analogous way to the hydrogen atom (with known solutions) by Hamiltonian [Yu 2010]:

$$H = -\Big(\frac{\hbar^2}{2m_e^*}\Big)\nabla_e^2 - \Big(\frac{\hbar^2}{2m_h^*}\Big)\nabla_h^2 - \frac{e^2}{4\pi\varepsilon_0\varepsilon_r|\mathbf{r}_e - \mathbf{r}_h|}, \tag{1.5}$$

where:

$\hbar$ – reduced Planck's constant,
∇ – nabla operator for electron and hole spatial coordinates,
$\mathbf{r}_e$ - $\mathbf{r}_h$ – difference between electron and hole spatial coordinates,
e – elementary charge, $e = 1.6 \cdot 10^{19}$ C,
ε_0 – dielectric constant of the vacuum,
ε_r – relative dielectric permittivity of the considered crystal.

Attractive nature of the Coulomb interaction between charge carriers, described by the third term of the Eq. 1.5, leads to a reduction of the exciton's energy, compared to the sum of energies of unbound, "free" carriers. As such, excitonic energy levels appear below the band gap energy E_g, as shown in Fig. 1.12 (b).

The energy difference between the free carriers' continuum and bound excitonic states is called an **exciton binding energy** and is defined as:

$$E_B = E_g - E_X, \tag{1.6}$$

where:

E_g – band gap of the material,
E_X – energy of the excitonic state.

Excitons can also exist in exited states, analogous to Rydberg states in a hydrogen atom. Effective mass acts as a renormalisation factor, and in the case of a 3D system, the energy of an n-th state is described by the formula:

$$E_n = E_g - \frac{R}{n^2} \tag{1.7}$$

where:

R – effective exciton Rydberg energy,
n – number of the respective excitonic state.

Effective exciton Rydberg energy is defined as:

$$R = \frac{m_r^* R_0}{m_0 \varepsilon_r^2}, \tag{1.8}$$

where:

m_0 – free electron mass,
R_0 – hydrogen atom Rydberg energy constant, $R_0 = 13.6$ eV

The most probable distance between an electron and a hole is called an exciton **Bohr radius**. It is analogous to the Bohr radius of the hydrogen atom, but modified by the material properties of a semiconductor. It is defined as:

$$a_B = \frac{4\pi\varepsilon_0\varepsilon\hbar^2}{m_r^* e^2} \tag{1.9}$$

and can be also interpreted as the size of the exciton's wavefunction. In classical semiconductors, it has values ranging from tens to hundreds of angstroms: for GaAs a_B=112 Å, for InP a_B=113 Å, for CdTe a_B=70 Å, or for GaN $a_B = 24$ Å, compared to 0.5 Å for the hydrogen atom [Yu 2010].

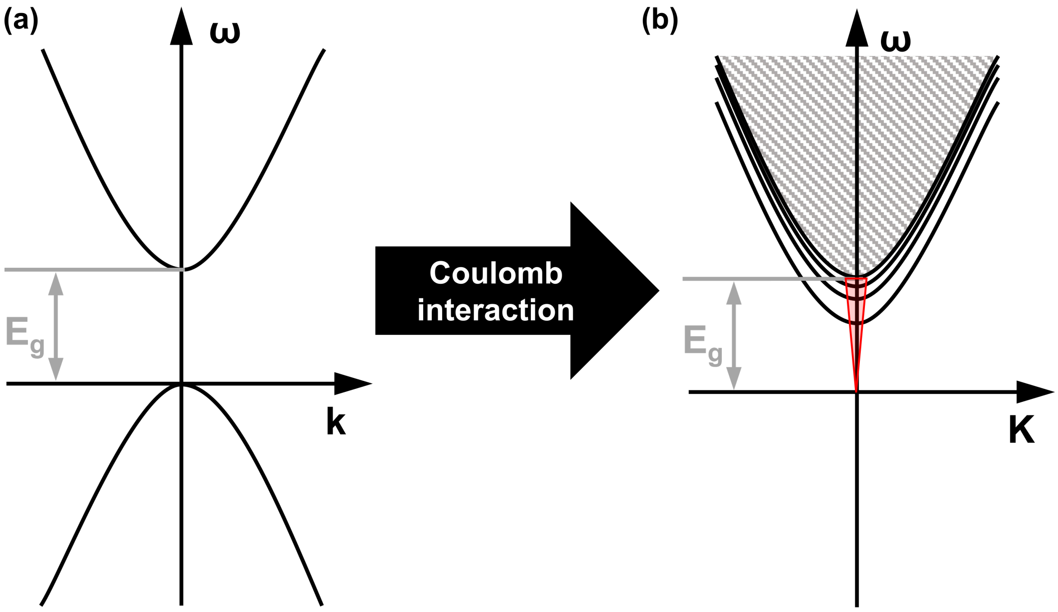

Figure 1.12: Comparison of the dispersion relation for the case of one-electron picture (a) and excitons (b). Bound excitonic states appear below the electronic band gap; due to the attractive nature of Coulomb interaction between electrons and holes, their bound states have reduced energy. Red lines denote the dispersion of photons. It is defined as ω = ck – linear, and in the considered energy range, extremely steep. Adapted from: [Singh 2007]

There is a difference between the description of excitation in the image of electrons and holes and the description taking into account their Coulomb interaction. As shown in Fig. 1.12 (a), excitation induces the transfer of an electron from the valence band to the conduction band and leaves a hole in the valence band. In the case of the excitonic description (Fig. 1.12 (b)), the ground state is the absence of excitons, and the excited state is the presence of an exciton. In this approach, transforming from two- to one-body problem gives the Hamiltonian with two components, first describing the movement of the exciton's centre of mass, which has a solution in form of a plane wave. The second one is describing the relative movement of electron and a hole [Singh 2007]. Thus, the exciton's energy states are described by the following expression:

$$E_n(\mathbf{K}) = E_n + \frac{\hbar^2}{2(m_e^* + m_h^*)}\mathbf{K}^2, \tag{1.10}$$

where:

K – exciton's centre of mass momentum,

and the second term in this expression is describing the exciton moving through a medium. Excitons are characterised by a continuous density of states, but direct optical transitions are allowed only for states with zero momentum and kinetic energy, in order to maintain the principle of the conservation of momentum. It is because, by comparison to the excitons, photons carry negligible momentum (as shown by the red lines in Fig. 1.12(b)).

1.3.3 Effects of Quantum and Dielectric Confinement

By reducing the dimensionality of the material, one can expect that the exciton binding energy will increase because of the spatial confinement of the charge carriers. For comparison, the binding energy eigenvalues for the 3D case are described by:

$$E_n = -\frac{m_r^* e^4}{2\hbar^2}\frac{1}{n^2}. \tag{1.11}$$

The eigenvalues for the 2D case and the exciton's Bohr radius are given by [Yang 1991]:

$$E_n = -\frac{m_r^* e^4}{2\hbar^2}\frac{1}{(n-\frac{1}{2})^2}, \quad a_{B(2D)} = \frac{4\pi\varepsilon_0\varepsilon\hbar^2}{2m_r^* e^2} \tag{1.12}$$

From the equations above, one can deduce that the binding energy increases 4 times when going from a three- to a two-dimensional system. At the same time, the Bohr radius for the 2D case decreases twofold.

The perfect 2D system practically does not exist; epitaxial quantum wells are very far from idealised 2D systems. In such case, with narrowing of the well, one can observe an increase in the exciton binding energy; however, for very thin wells, the trend is broken by leakage of wave functions to the barriers (due to their finite height) and never increases fourfold in relation to the binding energy in the bulk material.

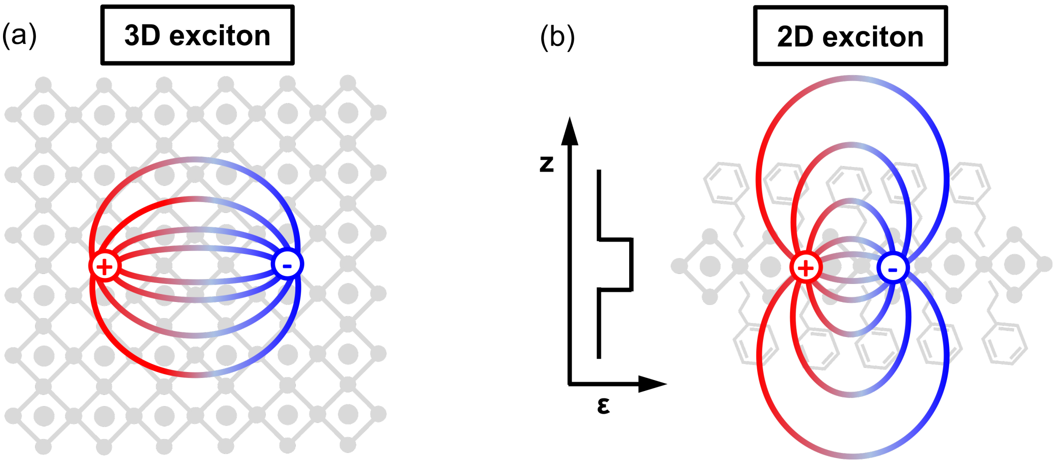

Figure 1.13: Comparison of the distribution of the electrostatic field lines for the exciton in (a) a bulk and (b) 2D crystal. Due to the contrast of dielectric constants between well and its environment ($\varepsilon_{well} > \varepsilon_{barrier}$), the interaction between charge carriers is enhanced due to the reduced dielectric screening in the barrier. Adapted from: [Chernikov 2014].

A significantly different behaviour is observed in the case of van der Waals crystals such as 2D perovskites. In this case, the condition of the existence of infinite barriers is fulfilled better than in the case of epitaxial wells. However, another effect occurs additionally; it is related to the abrupt change (decrease) of the dielectric constant in the organic barrier region. It is not as drastic in the case of epitaxial quantum wells of III-V materials, where both the barrier and the well material are characterised by similar dielectric permittivity, so the contrast is not as striking. This reduced screening in the barrier region effectively causes the electric field outside the well region to be less screened, resulting in stronger mutual attraction of the electron and hole (Fig. 1.13).

Due to the dielectric screening being limited to the 2D plane, the exciton binding energy increases significantly more than one would expect from the above-mentioned reduction in the dimensionality of the system alone. It can reach values of the order of several hundred meV. This effect occurs not only in the case of 2D perovskites, where there is a contrast in dielectric constants between the well and barrier regions, but also, for example, in transition metal dichalcogenides (TMD), where the dielectric screening is determined by the vacuum, the substrate or additional encapsulating layers [Chernikov 2014, Zhu 2020].

The electron-hole interaction in an inhomogeneous dielectric medium cannot be accurately described by the Coulomb potential. Strongly confined 2D systems are usually approximated by the so-called Rytova-Keldysh potential [Rytova 2018, Keldysh 1979], which can be successfully applied for TMD [Chernikov 2014]. It is defined as:

$$V_{eh}(r) = -\frac{e^2}{8\varepsilon_0 r_0}\left[H_0\left(\frac{\varepsilon_{\mathrm{avg}} r}{r_0}\right) - Y_0\left(\frac{\varepsilon_{\mathrm{avg}} r}{r_0}\right)\right] \tag{1.13}$$

where:

r – exciton radius,
r_0 – screening length,
H_0/Y_0 – Struve/Bessel functions,
ε_0 – dielectric constant of the vacuum,
ε_r – average dielectric constant of the top and bottom environment.

It strongly depends on the dielectric environment of the material, including its influence on the interaction between charge carriers in 2D systems, making this model more realistic. Not only does this result in large exciton binding energies, but also it modifies the energies of the excited states. Their distribution no longer follows the Rydberg rule of $E_n \propto -\frac{1}{n^2}$, which is especially apparent for lower values of n. The energy of higher excited states decreases more slowly than in the model using Coulomb's potential.

Rytova-Keldysh potential was used to model excitons in 2D perovskites [Feldstein 2020]. However, its accuracy in this case is brought into question, especially for compounds with a higher number of octahedra layers n [Blancon 2018].

The topic of excitons in 2D metal-halide perovskites is very complex because both quantum and dielectric confinement play an important role, as well as properties arising from the soft, polar nature of perovskites. The description is non-trivial, as there are multiple factors strongly shaping the optical properties of 2D perovskites.

1.3.4 Description of Excitons in Metal-Halide Perovskites

The effective mass model, shown in the subsection 1.3.2, has been successfully used to describe the properties of many semiconductors. However, the polar nature of the crystal lattice and strong exciton-phonon coupling render the use of the Coulomb potential in the Schrödinger equation too much of a simplified approach. Therefore, in the case of MHP, it can be treated mostly as an approximation. There are significant discrepancies between the predictions of the model and the experimental results [Baranowski 2020]. As discussed previously in Section 1.1.1, the perovskite crystal lattice is ionic and relatively soft. When fundamental electronic properties of MHP are considered, their polar nature is usually omitted, which then leads to discrepancies between predicted and observed behaviour. The soft ionic perovskite lattice is a factor that strongly differentiates these unique materials from their more "traditional" counterparts, like GaAs. In such a structure, it is imperative to consider not only the present charge carriers but also the importance of **phonons** – quasi-particles representing the collective vibrational movement of atoms within the crystal lattice [Fox 2010].

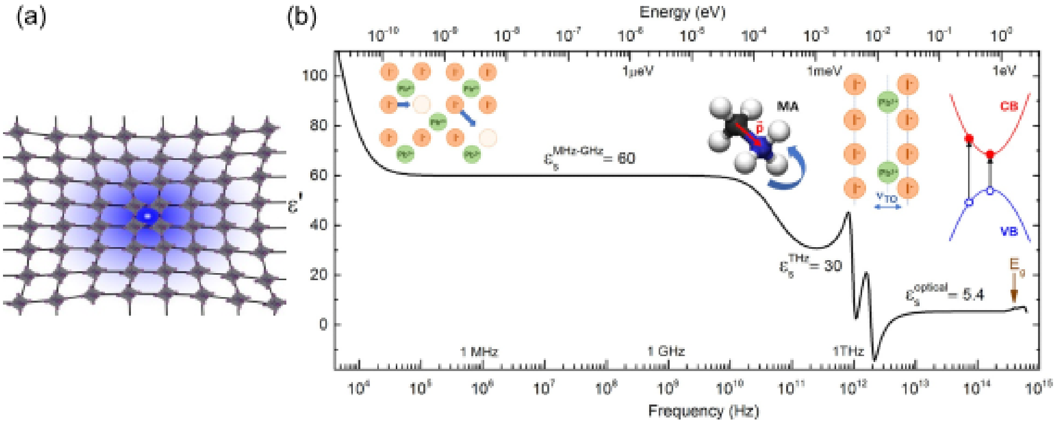

Figure 1.14: (a) Schematic presentation of a polaron as a charge carrier "dressed" in the local lattice polarisation. Adapted from [Schilcher 2021]. (b) Real part of the dielectric permittivity ε as a function of the frequency. Explicitly highlighted three regions of interest: high frequency ($4-8\cdot10^{14}$ Hz), associated with electronic inter-band transitions - ε_∞. Features around THz range originate from optical phonon resonances - ε_s. Low frequency regime, associated with migration of iodide ions. Adapted from [Herz 2018].

In the case of polar semiconductors, longitudinal optical (LO) phonons produce a macroscopic electric field, which interacts with the charge carriers via Coulomb interactions. This long-range coupling is a phenomenon known as **Fröhlich interaction** [Yu 2010]. As a result, the properties of MHP should be described in terms of **polarons** – coupled electronic and LO phonon states. They can be understood as charge carriers “dressed” by the local lattice polarisation (Fig. 1.14(a)).

Polaronic effects can dramatically influence the optoelectronic properties of the material: the charge-carrier interaction explains the reduced carrier mobilities, despite their low effective masses [Zhu 2015, Sendner 2016, Frost 2017]. It may also lead to renormalisation of the band gap [Fan 1967] and, in extreme cases, to self-trapping of excitons [Williams 1990, Munson 2018].

The magnitude of the charge carrier - LO phonon interaction is described by the dimentionless Fröhlich coupling constant α, defined as [Devreese 1996]:

$$\alpha = \frac{e^2}{\hbar}\left(\frac{1}{\varepsilon_\infty}-\frac{1}{\varepsilon_s}\right)\sqrt{\frac{m_{e,h}^2}{2E_{LO}}} = \frac{e^2}{\hbar}\frac{1}{\varepsilon^*}\sqrt{\frac{m_{e,h}^2}{2E_{LO}}} \tag{1.14}$$

where:

e – elementary charge,
$\hbar$ – reduced Planck’s constant,
$m_{e,h}$ – effective mass of charge carriers,
E_{LO} – energy of the optical phonon mode,
ε – frequency-dependent dielectric permittivity.

The difference $\left(\frac{1}{\varepsilon_\infty}-\frac{1}{\varepsilon_s}\right)=\frac{1}{\varepsilon^*}$ accounts for screening of charge carriers, where ε_∞ is dielectric permittivity at “‘optical” frequency, and ε_s is the “static” dielectric permittivity. “Optical” is a frequency range associated with electronic interband transitions; “static” in this case refers to a lower, THz frequency range associated with phonon resonances of the inorganic lattice.

Coupling of carriers to the lattice manifests in the enhancement of their effective mass, which can be approximated as [Feynman 1955]:

$$m_{e,h}^* = m_{e,h}\left(1+\frac{\alpha}{6}\right) \tag{1.15}$$

At this point, it is important to also consider the dielectric response of MHP. Fig. 1.14 (b) shows the real part of the dielectric permittivity of $\mathrm{MAPbI_3}$ at room temperature [Herz 2018]. ε is strongly dependent on the frequency (as opposed to the “classical” semiconductors [Moore 1996]). In other words, there is a significant difference between “static”, $\varepsilon_s = 30$ and “optical”, $\varepsilon_\infty = 5.4$ values of dielectric permittivity. Such a striking difference points at more complex picture of the magnitude of dielectric screening of carriers and highlights the fact that the Fröhlich interaction cannot be ignored in the case of MHP. The contrast between static and optical ε values gives a significant value of the Eq. 1.14 term $\left(\frac{1}{\varepsilon_\infty}-\frac{1}{\varepsilon_s}\right)=\frac{1}{\varepsilon^*}$. Moreover, the relatively soft crystal lattice results in lower energies of optical phonon modes [Leguy 2016, Létoublon 2016, Sendner 2016]. Both of these facts lead to a higher α than in other semiconductors, and thus significantly increased effective mass of carriers (as seen in Eq. 1.15).

The point described above is important when it comes to the description of excitons in this material system. The answer to a question – which value of the dielectric constant should be assumed in the Eq. 1.5 – becomes complicated, as the dielectric permittivity of MHP is strongly frequency dependent, and Fröhlich coupling between charge carriers and crystal lattice cannot be omitted. It is possible to model this system still using the hydrogen atom framework, but with modified potential placed in the Shrödinger's equation in place of a Coulomb potential:

$$\hat{H}\phi = E\phi = -\frac{\mathbf{p}^2}{2m_r^*}\phi + V(R)\phi = E\phi \tag{1.16}$$

where:

$\mathbf{p}$ – momentum operator,
$V(R)$ – potential,
E – energy of the eigenstates.

Alternative potentials, including terms that account for the polaronic effects in MHP, were proposed [Bajaj 1974, Haken 1958, Pollmann 1977]. These models have been shown to more accurately describe their optical properties observed experimentally (in the case of 3D perovskites) [Baranowski 2020, Baranowski 2024].

Given all of the above, the problem of excitons in 2D perovskites becomes quite complex, with multiple factors shaping their properties. At the same time, because of large values of the binding energy reaching hundreds of millielectronvolts, excitons are present up to the room temperature. As such, excitonic effects dominate the optical response of 2DP, and understanding them is imperative to correctly describe the physical phenomena occurring in this system. The models used so far have proven to be too simple to reproduce the experimental findings; it is especially difficult to model 2DP compounds with a higher number of octahedra layers in the structure [Blancon 2018]. In such systems, the dielectric permittivity does not only display a strong frequency dependence [Herz 2018], but also a spatial one - in a 2DP layered structure, the dielectric permittivity of the inorganic and organic parts is significantly different, providing the dielectric confinement to the charge carriers (as shown in Fig. 1.13) [Pedesseau 2016]. This fact adds yet another layer of complexity to the problem of excitons in 2D perovskites. A model that includes image charges, self-energy corrections, and coupling of charge carriers to the crystal lattice was recently proposed as an attempt to account for all of the effects described above [Movilla 2023]. Furthermore, experimental investigations of the optical properties of 2D perovskites are essential, as by obtaining these data it is possible to verify the accuracy of the existing theories.

1.3.5 Exciton Fine Structure

The exciton fine structure results from the exchange interaction between the electron and the hole [Bir 1974, Bayer 2002] and reflects the fundamental symmetry of the system. The exchange interaction lifts the degeneracy between the bright and dark exciton states. The names "bright" and "dark" in this case refer to the possible coupling to photons, upholding the principle of conservation of angular momentum (*i.e.* if the total angular momentum of such excitonic state equals ±1). The low symmetry of the crystal leads to the anisotropy of the exchange interaction ($J_{x/y/x}$), as described by the equation [Yu 2016]:

$$H_{ex} = J_z \sigma_z^e \sigma_z^h + J_x \sigma_x^e \sigma_x^h + J_y \sigma_y^e \sigma_y^h, \tag{1.17}$$

where $\sigma_{x/y/x}^{e/h}$ represents the spin operators for electrons and holes, defined as:

$$\sigma_x = \begin{pmatrix} 0 & 1 \\ 1 & 0 \end{pmatrix}, \quad \sigma_y = \begin{pmatrix} 0 & -i \\ i & 0 \end{pmatrix}, \quad \sigma_z = \begin{pmatrix} 1 & 0 \\ 0 & -1 \end{pmatrix} \tag{1.18}$$

The exchange hamiltonian (Eq. 1.17) can be expressed by using wavevectors of the following basis:

$$\begin{aligned} |\psi_1\rangle &= \tfrac{1}{\sqrt{2}}\Big(|{\downarrow}\rangle_e |{\uparrow}\rangle_h - |{\uparrow}\rangle_e |{\downarrow}\rangle_h\Big), \\ |\psi_2\rangle &= \tfrac{1}{\sqrt{2}}\Big(|{\downarrow}\rangle_e |{\uparrow}\rangle_h + |{\uparrow}\rangle_e |{\downarrow}\rangle_h\Big), \\ |\psi_3\rangle &= |{\downarrow}\rangle_e |{\downarrow}\rangle_h , \\ |\psi_4\rangle &= |{\uparrow}\rangle_e |{\uparrow}\rangle_h . \end{aligned} \tag{1.19}$$

where:

$$|{\uparrow}\rangle = \begin{pmatrix} 1 \\ 0 \end{pmatrix}, \quad |{\downarrow}\rangle = \begin{pmatrix} 0 \\ 1 \end{pmatrix}, \tag{1.20}$$

and the indices e/h refer to electrons and holes, respectively. These wavevectors represent four excitonic states, originating from four possible combinations of electrons and holes at the bandedges. As discussed in section 1.2, perovskites are direct-band-gap semiconductors, and the band-edge states consist of metal and halide orbitals. *Ab initio* calculations of band structure for 2D perovskites [Giorgi 2018, Filip 2022, Quarti 2024] show the same thing, which is not that surprising, considering the fact that the inorganic framework does not change when transforming from 3D to 2D case (Fig. 1.3). Thus, the holes in the VBM have the angular momentum equal to ± 1/2, the same as the electrons in the lowest CBM. This leads to four possible combinations of an exciton (Fig. 1.15) - one with a total angular momentum J=0 and three with J=1. ψ_1 is the optically inactive singlet state, ψ_2 is the optically active triplet bright state with the dipole moment oriented along the c axis of the crystal, perpendicular to the 2D material plane. ψ_3 and ψ_4 are triplet bright states with their dipole moments oriented within the plane of the 2D crystal.

The exchange Hamiltonian, written in the above basis, has a form:

$$H_{ex} = \begin{pmatrix} -J_z - J_x - J_y & 0 & 0 & 0 \\ 0 & -J_z + J_x + J_y & 0 & 0 \\ 0 & 0 & J_z & J_x - J_y \\ 0 & 0 & J_x - J_y & J_z \end{pmatrix} \tag{1.21}$$

Its eigenstates and eigenvalues (energies of the excitonic states) are the following:

$$\begin{aligned} |D\rangle &= \frac{1}{\sqrt{2}}\left(|{\downarrow}\rangle_e |{\uparrow}\rangle_h - |{\uparrow}\rangle_e |{\downarrow}\rangle_h\right) = |\psi_1\rangle\,, \quad E_D = -J_z - J_x - J_y \\ |Z\rangle &= \frac{1}{\sqrt{2}}\left(|{\downarrow}\rangle_e |{\uparrow}\rangle_h + |{\uparrow}\rangle_e |{\downarrow}\rangle_h\right) = |\psi_2\rangle\,, \quad E_Z = -J_z + J_x + J_y \\ |Y\rangle &= \frac{1}{\sqrt{2}}\left(|{\downarrow}\rangle_e |{\downarrow}\rangle_h + |{\uparrow}\rangle_e |{\uparrow}\rangle_h\right) = \frac{1}{\sqrt{2}}\left(|\psi_3\rangle + |\psi_4\rangle\right), \quad E_Y = J_z + |J_x - J_y| \\ |X\rangle &= \frac{1}{\sqrt{2}}\left(|{\downarrow}\rangle_e |{\downarrow}\rangle_h - |{\uparrow}\rangle_e |{\uparrow}\rangle_h\right) = \frac{1}{\sqrt{2}}\left(|\psi_3\rangle - |\psi_4\rangle\right), \quad E_X = J_z - |J_x - J_y| \end{aligned} \tag{1.22}$$

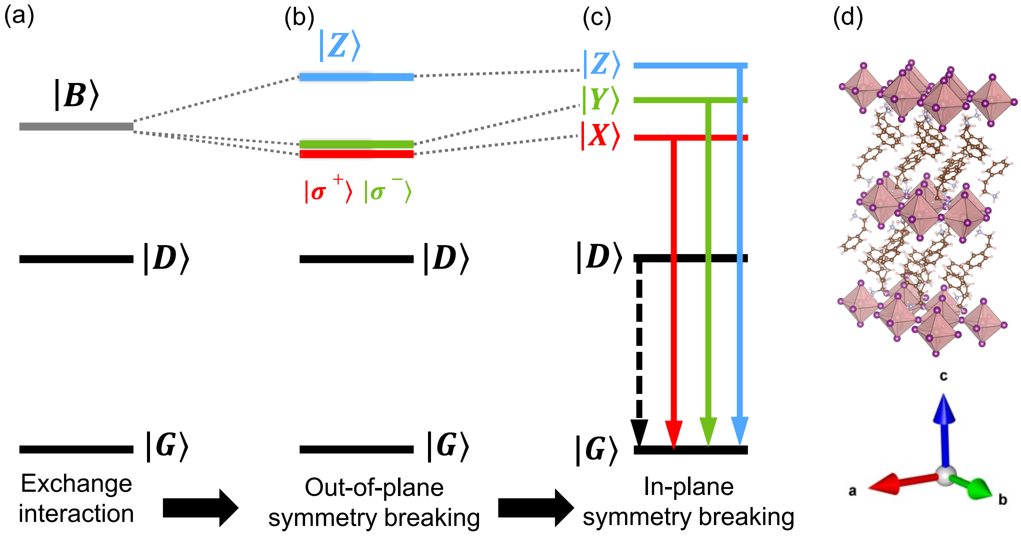

Figure 1.15: Schematic of an evolution of the exciton fine structure in a realistic material systems, including both (a) exchange interaction between spins of charge carriers and (b-c) influence of the crystal field as the symmetry of the material is lowered. (d) Orientations of the crystal axes within the 2DP structure.

In case of an isotropic system (cubic crystal symmetry), $J_x = J_y = J_z$. Thus, as shown by the Eq. 1.22, bright states $|X\rangle, |Y\rangle, |Z\rangle$ remain of the same energy, however the degeneracy between them and the dark state $|D\rangle$ is lifted. In other words, the exchange interaction between charges splits the bright states from the dark states (Fig. 1.15 (a)). If the crystal symmetry is lowered (which *e.g.* can be due to the phase transitions in which the perovskite crystals can undergo [Møller 1957, Poglitsch 1987]), the degeneracy between the bright states is abolished. Due to the 2D nature of crystals, the symmetry is broken in the direction perpendicular to the crystal plane. In case of such 2D system (or in 3D case with tetragonal symmetry), $J_x = J_y \neq J_z$. This separates the state in which the dipole moment is oriented perpendicular to the crystal plane from the states in which the dipole moments are oriented in the crystal plane (Fig. 1.15 (b)).

If the structure has a symmetry *in plane*, then the term $J_x - J_y = 0$, and there is no "mixing" of states. All basis states (Eq. 1.19) are eigenstates, and the *in plane* states $|\psi_3\rangle$ and $|\psi_4\rangle$ are coupling to the right- and left-handed circularly polarised light. In the case where the *in plane* symmetry of the 2D perovskite is broken, then the $J_x \neq J_y$ and the degeneracy of the bright states will be completely lifted (Fig. 1.15 (c)). The two *in plane* bright states are a "mix" of circularly polarised basis states $|\psi_3\rangle$ and $|\psi_4\rangle$, as shown in Eq. 1.22. As superposition of right- and left-handed circularly polarised waves results in linearly polarised states, $|X\rangle$ and $|Y\rangle$ states will couple to two orthogonal linear polarisations of light. The Hamiltonian of such fully non-degenerate system, including the exchange interaction, can then be finally written as:

$$
\begin{aligned}
H_{(D,Z,X,Y)} &= \begin{pmatrix} E_D & 0 & 0 & 0 \\ 0 & E_Z & 0 & 0 \\ 0 & 0 & E_X & 0 \\ 0 & 0 & 0 & E_Y \end{pmatrix} \\
&= \begin{pmatrix} -J_z - J_x - J_y & 0 & 0 & 0 \\ 0 & -J_z + J_x + J_y & 0 & 0 \\ 0 & 0 & J_z - |J_x - J_y| & 0 \\ 0 & 0 & 0 & J_z + |J_x - J_y| \end{pmatrix}.
\end{aligned}
\tag{1.23}
$$

The fine structure splitting can have dramatic consequences for light emitters operating in the excitonic recombination regime because the lowest excitonic state is usually dark and, as such, provides a channel for efficient nonradiative recombination. The significant value of dark-bright state splitting reduces the device efficiency as a result of the preferential occupancy of the dark state in thermodynamic equilibrium. Therefore, understanding the properties of excitons in 2D materials is not only a matter of scientific curiosity, but this knowledge can help develop deterministic strategies to improve the design and performance of potential devices. The exciton fine structure, or more precisely, its bright states, is also the subject of intensive research due to its key role in very sophisticated devices, such as single or entangled photon emitters [Bayer 2002, Plumhof 2012, Huber 2018] for use in quantum telecommunications.

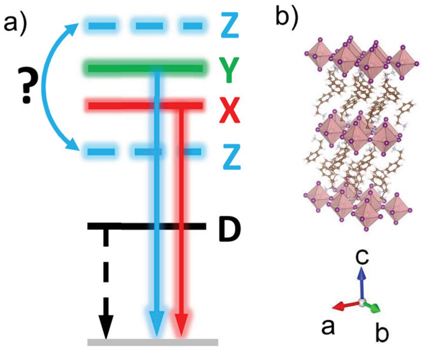

Figure 1.16: (a) Schematic of an exciton fine structure of 2D perovskites, showing possible positions of the Z state. (b) Schematic of a representative 2D perovskite $(PEA)_2PbI_4$ crystal structure, with crystal axes shown. Adapted from [Posmyk 2024a].

In recent years, the topic of the band edge exciton fine structure in perovskites, more specifically, the energy ordering of states within, has been revisited and studied using different theoretical approaches. However, there were discrepancies between the results obtained in these investigations. For example, in the works using models based on the multi-band effective mass theory [Tanaka 2005, Ema 2006, Fieramosca 2018, Steger 2022] the dark state is located as the lowest one energetically, followed by *out of plane* oriented bright Z state and remaining X and Y *in plane* states. However, recent *ab initio* works reversed the order of bright states, placing the Z state above X and Y as energetically highest [Quarti 2020, Quarti 2024]. There was also a report that included the Rashba effect in considering the exciton fine structure for perovskite nanocrystals [Sercel 2019], which reversed the order of states in a way that placed the dark state as the energetically highest.

In earlier experimental works, by the use of optical spectroscopy techniques combined with the magnetic field, the position of the dark D state was confirmed to be the energetically lowest [Tamarat 2019, Dyksik 2021a]. However, the position of the *out of plane* Z state with respect to the other states has not been confirmed at this point (Fig. 1.16), even though a trace of it has been observed in the optical spectra at extremely high magnetic fields [Dyksik 2021a]. In lead iodide nanocrystals, the exciton fine structure has also been observed to strongly depend on dimensionality [Fu 2017, Tamarat 2019, Liu 2021]. Without clear experimental evidence, the exciton fine structure in low-dimensional perovskite systems remains incomplete. In order to establish the said picture in 2D perovskites, this problem was experimentally approached [Posmyk 2022, Posmyk 2024a], and the results of these investigations will be described in detail in this work.

1.3.6 Excitons in the Magnetic Field

The magnetic field, in conjunction with optical spectroscopy techniques, has proven to be an effective tool for studying the optoelectronic properties of perovskites, such as exciton binding energy or carriers' effective mass [Yang 2017, Galkowski 2019, Baranowski 2019b, Dyksik 2020, Dyksik 2021b, Baranowski 2024]. The magnetic field introduces perturbation to the excitonic wave function, resulting in breaking of the system's symmetry - the excitonic states, as described by Eq. 1.19, are no longer the eigenstates of the Hamiltonian. However, the new eigenstates can be expressed as a linear combination of exciton states without magnetic field [Yu 2016]. In the case of a structure with low crystal symmetry, with anisotropy both *in plane* and *out of plane* of the crystal, they can be expressed as a linear combination of two pairs of zero-field states. The new Hamiltonian, describing the system under the influence of the external magnetic field, can be expressed as follows:

$$H_B = H_{\text{ex}} + H_Z, \tag{1.24}$$

where H_{ex} is the exchange Hamiltonian, defined in the Eq. 1.17, and H_Z is the Hamiltonian describing the Zeeman energy (Zeeman hamiltonian), defined as:

$$H_Z = \frac{1}{2}\mu_B \left(g_e(B_x\sigma_x^e + B_y\sigma_y^e + B_z\sigma_z^e) + g_h(B_x\sigma_x^h + B_y\sigma_y^h + B_z\sigma_z^h) \right). \tag{1.25}$$

where:

μ_B – Bohr magneton,
$g_{e/h}$ – g-factor of an electron and a hole, respectively.

The g-factor (also called the Landé g-factor) is a dimensionless parameter that describes how strongly the spin or orbital angular momentum of a particle couples to an external magnetic field [Landé 1921]. The g-factors are related, by their value and anisotropy, to the band parameters of the material [Ivchenko 2005, Yu 2016, Kirstein 2022a]. As the considered structure is anisotropic, their g-factors also are, thus in this case two characteristic components are considered – paralell $\mathrm{g}_{\|}$ and perpendicular $\mathrm{g}_{\perp}$ to the *c* axis of the crystal (as defined in Fig. 1.16). The specific cases will be discussed below, as different experimental configurations probe the system in different spatial directions.

The magnetic field vector and its components are written as:

$$\mathbf{B} = (B_x, B_y, B_z). \tag{1.26}$$

There are two typical experimental configurations of the orientation in which the magnetic field vector **B** is oriented with relation of the k vector of the light; usually k is paralell to the c-axis of the 2D crystal, as shown in the Fig. 1.17.

- *Faraday configuration*, where $\mathbf{B} = (0, 0, \mathrm{B})$, or $\mathbf{B} \parallel \mathbf{k} \parallel c$,
- *Voight configuration*, where $\mathbf{B} = (\mathrm{B}, 0, 0)$ or $\mathbf{B} \perp \mathbf{k} \parallel c$.

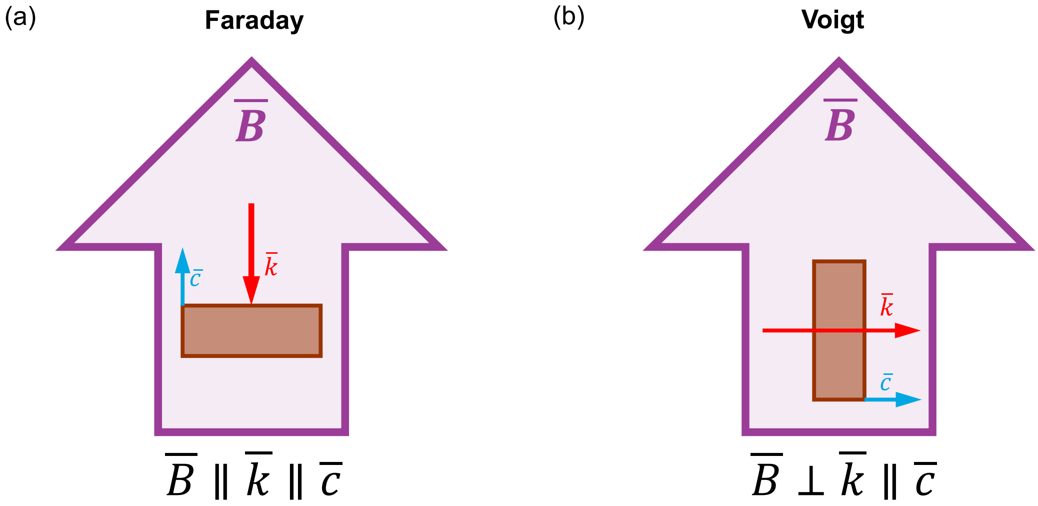

Figure 1.17: (a) Schematic of the geometric configurations of the experiments in the magnetic field: (a) Faraday configuration, where **B** (purple) ∥ **k** (red) ∥ c (blue); (b) Voigt configuration, when **B** (purple)⊥ **k** (red) ∥ c (blue).

Faraday configuration In this geometry, the magnetic field **B** is paralell to the light wavewector **k**, and in this particular case oriented along the c axis of the crystal (**B** = (0,0,B)), as shown in the Fig. 1.17(a). The Zeeman Hamiltonian in this case has the following form (after [Yu 2016]):

$$H_Z = \frac{1}{2}\mu_B B_z \left(g_{e\|}\sigma_z^e + g_{h\|}\sigma_z^h \right), \tag{1.27}$$

Let us define "dark" and "bright" g-factors paralell to the c-axis of the crystal (accessible in this experimental geometry), respectively:

$$\begin{aligned} g_D &= g_{e\|} - g_{h\|} \\ g_B &= g_{e\|} + g_{h\|} \end{aligned} \tag{1.28}$$

The calculations below are done in basis defined in the Eq. 1.19, $|\psi\rangle$ basis. In this framweork, both H_{ex} and H_Z have the terms in the same two diagonal blocks. They can be considered separately; for the first block, states $|\psi_1\rangle = |D\rangle$ and $|\psi_2\rangle = |Z\rangle$, there are off-diagonal terms in the full magnetic field Hamiltonian, indicating the "mixing" of these two states:

$$H_{B(1,2)} = \begin{pmatrix} -J_z - J_x - J_y & \frac{1}{2}\mu_B B_z g_D \\ \frac{1}{2}\mu_B B_z g_D & -J_z + J_x + J_y \end{pmatrix} \tag{1.29}$$

The eigenvalues of this part are given by:

$$E_{D,Z}(B) = -J_z \pm \sqrt{(J_x + J_y)^2 + \left(\frac{1}{2}\mu_B B_z g_D\right)^2} \tag{1.30}$$

The eigenvectors in the magnetic field can be expressed as a linear combination of the zero-field eigenvectors (as defined in Eq. 1.22):

$$\begin{aligned} |D_B\rangle &= c_2\,|\psi_1\rangle - c_1\,|\psi_2\rangle, \\ |Z_B\rangle &= c_1\,|\psi_1\rangle + c_2\,|\psi_2\rangle, \end{aligned} \tag{1.31}$$

It is important to note that $|\psi_1\rangle = |D\rangle$ and $|\psi_2\rangle = |Z\rangle$, as the exchange interaction does not introduce any mixing between the two states (only lifts their degeneracy). The coefficients c_1 and c_2 are defined as [Kataoka 1993]:

$$\begin{aligned} c_1 &= \sqrt{\frac{1}{2}\left(1 - \frac{J_x + J_y}{\sqrt{(J_x+J_y)^2 + \left(\frac{1}{2}\mu_B B_z\, g_D\right)^2}}\right)}, \\ c_2 &= \sqrt{\frac{1}{2}\left(1 + \frac{J_x + J_y}{\sqrt{(J_x+J_y)^2 + \left(\frac{1}{2}\mu_B B_z\, g_D\right)^2}}\right)}. \end{aligned} \tag{1.32}$$

These coefficients quantify how much of each zero-field basis state contributes to a given eigenstate in the magnetic field. They depend on the magnetic field and describe the field-dependent mixing of excitonic eigenstates owing to Zeeman or exchange interactions. In Fig. 1.18 (a) the square values of the coefficients c_1 and c_2 are shown. It can be seen there, as well as from the Equations 1.32 and 1.31, that in the absence of the external magnetic field, B=0, $|D_B\rangle = |D\rangle$ and $|Z_B\rangle = |Z\rangle$. With increasing magnetic field, in a high field limit, both c_1^2 and c_2^2 are approaching $\frac{1}{2}$, showing equal mixing of states.

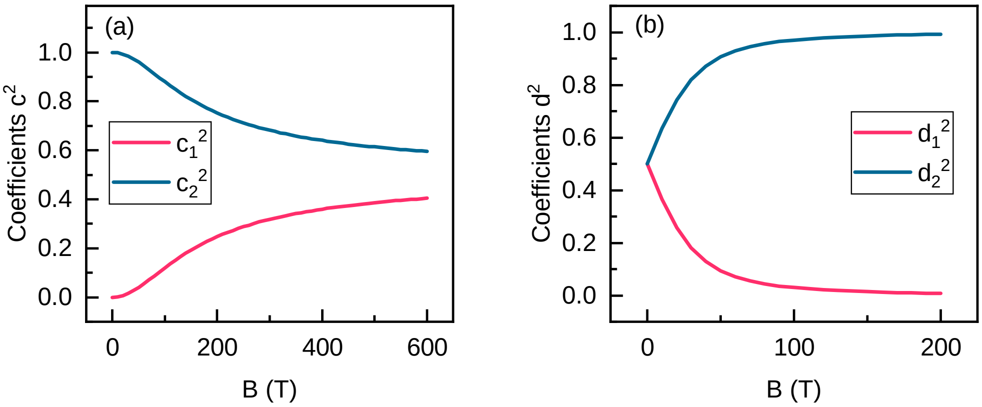

Figure 1.18: Square value of coefficients (a) c_1 (pink) and c_2 (blue) and (b) d_1 (pink) and d_2 (blue) as a function of the magnetic field, showing the gradual mixing of states of the exciton fine structure in the magnetic field, as shown by the Eq. 1.32 and 1.36. Values of $J_x = 5.2\,\text{meV}$, $J_y = 3.95\,\text{meV}$, $J_z = 2.6\,\text{meV}$ were calculated from the Eq. 1.22 using experimental energy values from [Posmyk 2024a].

By analogy, the second block of the full H_B Hamiltonian describes the mixing of states $|X\rangle$ and $|Y\rangle$:

$$H_{B(3,4)} = \begin{pmatrix} J_z - \frac{1}{2}\mu_B B_z\, g_B & J_x - J_y \\ J_x - J_y & J_z + \frac{1}{2}\mu_B B_z\, g_B \end{pmatrix} \tag{1.33}$$

with the eigenvalues:

$$E_{X,Y}(B) = J_z \mp \sqrt{(J_x - J_y)^2 + \left(\tfrac{1}{2}\mu_B B_z\, g_B\right)^2} \tag{1.34}$$

and eigenvectors:

$$\begin{aligned} |X_B\rangle &= d_2\, |\psi_3\rangle - d_1\, |\psi_4\rangle, \\ |Y_B\rangle &= d_1\, |\psi_3\rangle + d_2\, |\psi_4\rangle, \end{aligned} \tag{1.35}$$

The coefficients d_1 and d_2 are defined as:

$$\begin{aligned} d_1 &= \sqrt{\frac{1}{2}\left(1 - \frac{\frac{1}{2}\mu_B B_z\, g_B}{\sqrt{(J_x - J_y)^2 + \left(\frac{1}{2}\mu_B B_z\, g_B\right)^2}}\right)}, \\ d_2 &= \sqrt{\frac{1}{2}\left(1 + \frac{\frac{1}{2}\mu_B B_z\, g_B}{\sqrt{(J_x - J_y)^2 + \left(\frac{1}{2}\mu_B B_z\, g_B\right)^2}}\right)}. \end{aligned} \tag{1.36}$$

These coefficients are also field dependent (Fig. 1.18 (b)). Both coefficients d_1 and d_2 are equal to $\frac{1}{\sqrt{2}}$ when B=0, and with increasing magnetic field $d_1 \to 0$ and $d_2 \to 1$. Furthermore, it is important to note that in case of B=0, $|X_B\rangle = \frac{1}{\sqrt{2}}(|\psi_3\rangle - |\psi_4\rangle) = |X\rangle$ and $|Y_B\rangle = \frac{1}{\sqrt{2}}(|\psi_3\rangle + |\psi_4\rangle) = |Y\rangle$. It means that for the (zero-field) X/Y state pair, in the magnetic field, the oscillator strength of these states does not change; rather, their exchange interaction-induced coupling decreases, gradually suppressed by the Zeeman effect. Thus, they become more like the original basis states $|\psi_3\rangle$ and $|\psi_4\rangle$ and couple to the circularly polarised light.

The equations above: 1.30 and 1.34 can also be written in the simplified notation of the states used in this work (X, Y, Z, D) and using the zero-field energy eigenvalues as:

$$\tilde{E}_{Y(D)/X(Z)}(B) = \frac{1}{2}\left[(E_{Y(Z)} + E_{X(D)}) \pm \sqrt{(E_{Y(Z)} - E_{X(D)})^2 + g_{B(D)}^2 \mu_{\mathrm{B}}^2 B^2}\right] \tag{1.37}$$

The evolution of excitonic states in the magnetic field, as described by the above formula (Eq. 3.2), is shown in Fig. 1.19. Two pairs of states shift in energy in opposite directions, as influenced by the Zeeman effect. In Faraday configuration, relevant to this work, the pairs are XY (pink and green solid lines) and DZ (black and blue dotted lines), as described above.

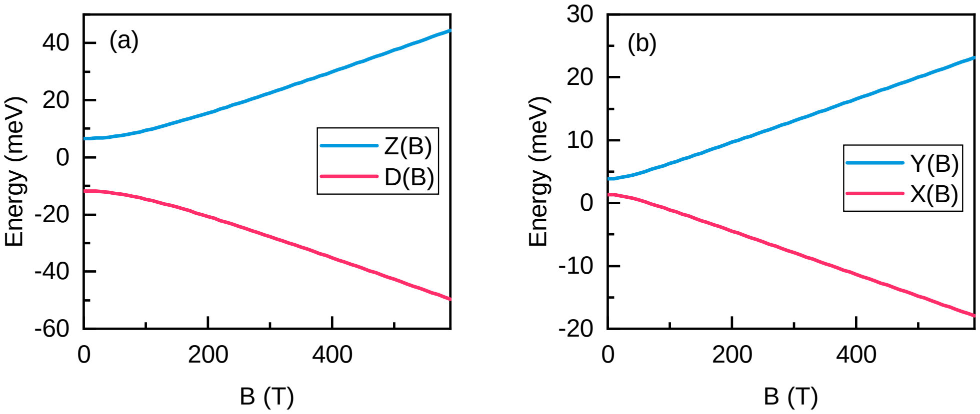

Figure 1.19: Schematic presentation of the evolution of the exciton fine structure in the magnetic field in Faraday configuration. Calculated from the Eq. 1.30 for (a) D and Z pair, and from Eq. 1.34 for (b) X and Y pair. In both cases, the values of $J_x = 5.2\,\text{meV}$, $J_y = 3.95\,\text{meV}$, $J_z = 2.6\,\text{meV}$ were used, calculated from the Eq. 1.22 using experimental energy values from [Posmyk 2024a].

In the case of the Faraday configuration, $g_{B(D)}$ is the bright (dark) exciton g-factor along the c axis of the crystal, being sum (difference) of electron and hole g-factors, also along the c axis of the crystal:

$$g_{B(D)} = g_{e\|} \pm g_{h\|} \tag{1.38}$$

In this configuration, the X and Y states can be detected with the light circularly polarised in the plane of the 2D crystal ($\mathbf{k} \parallel c$). As for the Z/D pair, the dipole forbidden dark state D under the magnetic field “mixes” with the remaining bright state Z, gaining the oscillator strength and thus the ability to interact with light. Z state, consequently, will lose the oscillator strength in these conditions. As the dipole moment of the Z state is oriented *out of plane* of the crystal, these states interact with the light polarised along the 2D crystal plane ($\mathbf{k} \perp c$).

The magnetic field modifies the orbital motion of electrons and holes, changing the spatial extent of the exciton’s wave function. The effective “squeezing” of the wavefunction leads to the increase of the exciton energy. When the exciton binding energy is much higher than the cyclotron energy of the charge carriers, the blueshift has a quadratic dependence on B. This effect is known as a **diamagnetic shift**, and has the form [Miura 2007]:

$$\Delta E_{dia} = c_0 B^2 \tag{1.39}$$

c_0 is a diamagnetic coefficient and is defined as:

$$c_0 = \frac{e^2}{8m_r^*}\langle r^2 \rangle, \tag{1.40}$$

where:

e – elementary charge,
m_r^* – exciton reduced effective mass,
$\langle r^2 \rangle$ – exciton mean squared radius (expected value of the carriers' separation, squared).

Thus, the formula describing the evolution of the excitonic states' energy, including both the Zeeman effect and a diamagnetic shift, has the following form:

$$E_{Y(D)/X(Z)} = \frac{1}{2}\Big[(E_{Y(Z)} + E_{X(D)}) \pm \sqrt{(E_{Y(Z)} - E_{X(D)})^2 + g^2_{B(D)}\mu^2_{\mathrm{B}}B^2}\Big] + c_0 B^2 \tag{1.41}$$

Intensity of the PL in the magnetic field As shown in Eq. 1.31, the magnetic field induces a mixing of the dark exciton state with the bright state [Yu 2016]. In the Faraday configuration, the field couples the dark state D with the *out of plane* bright state Z, which results in a transfer of oscillator strength from the bright state to the dark state. In the so-called weak-field limit, this effect can be approximated by

$$f_D(B) \approx \left(\frac{\mu_B g_D B}{\Delta}\right)^2 f_{\mathrm{BX}}\,, \tag{1.42}$$

where

μ_B – Bohr magneton,
g_D – effective g-factor of the dark exciton,
Δ – energy splitting between the bright Z and dark D exciton states,
f_{BX} – oscillator strength of the bright state at zero magnetic field.

In this framework, the photoluminescence intensity from the dark state grows proportionally to B^2 in the weak-field regime, where the Zeeman energy is much smaller than the bright–dark energy splitting, $|\mu_B g B| \ll \Delta$. This quadratic dependence is a direct consequence of the two-level mixing model, in which the dark exciton gains oscillator strength through magnetic-field-induced hybridisation with the bright state [Zhang 2009, Molas 2017]. The quadratic dependence presented here is a simplified picture, as in real perovskite systems the thermal distribution of carriers and the finite excitonic lifetimes must also be taken into account, both of which significantly influence the observed photoluminescence. However, this simplified description it remains an accurate approximation in the weak-field regime. In particular, at low temperatures where the dark state is preferentially occupied, the quadratic dependence of the PL intensity on the magnetic field is a good approximation.

Voigt configuration In Voigt configuration (shown in the Fig. 1.17 (b)), magnetic field will "mix" the dark state with *in plane* bright states. The first pair of states is characterised by a dipole moment oriented along the magnetic field vector **B** and is called longitudinal, while the second pair is labelled transverse and has its dipole moment perpendicular to **B**. The energies of these states can be expressed with the formula:

$$E_{Y(Z)/D(X)} = \frac{1}{2}\left[(E_{Y(Z)} + E_{D(X)}) \pm \sqrt{(E_{Y(Z)} - E_{D(X)})^2 + g^2_{L(T)}\mu^2_{\mathrm{B}}B^2}\right] + c_0B^2 \tag{1.43}$$

where $g_{L(T)}$ is the longitudinal (transverse) exciton g-factor perpendicular the c axis of the crystal being difference (sum) of electron and hole g-factors (perpendicular to the c axis of the crystal):

$$g_{L(T)} = g_{h\perp} \mp g_{e\perp} \tag{1.44}$$

Again, the external magnetic field induces the transfer of the oscillator strength from the bright states to the dark state, effectively brightening it and allowing its detection with the light polarised along the magnetic field ($\mathbf{E} \parallel \mathbf{B}$).

This experimental geometry was not used in this work; all of the measurements in the high magnetic fields shown were performed in the Faraday configuration.

As shown in the formulas above, in order to accurately determine the values of the excitonic g-factors in both configurations, it is crucial to have information on the zero-field energy of all states of the exciton fine structure, as well as their evolution under the influence of the magnetic field.

1.4 Research Objectives

The main objective of this study was to empirically determine the full exciton fine structure in a representative 2D metal-halide perovskite, that is, phenylethylammonium lead iodide $(PEA)_2PbI_4$. More specifically, the excitonic states' energies, order, and separation were confirmed by means of optical spectroscopy with and without the use of high external magnetic field conditions. The results obtained in this study provide a baseline for further theoretical investigations and resolve the controversy about the ordering of states present in the literature [Tanaka 2005, Sercel 2019, Quarti 2024]. Establishing the fine structure is also crucial from the point of view of potential applications, especially with regard to the interaction of the material with light. The energy spacing between the states, as well as the information about whether the lowest energetically (and thus preferently occupied) state is bright or dark, has a dramatic impact on the performance of a perovskite-based device [Tamarat 2019]. Dark states, which are not interacting with light, provide an effective channel for non-radiative recombination, which may hinder the operation of the light emitters. For optoelectronics, the key is the radiative recombination process, which is possible with bright excitonic states. Hence, knowing the spacing between the states and the position of the dark state with respect to the bright states is necessary when designing and optimising the performance of a potential device [Gan 2019, Folpini 2020].

Furthermore, the influence of the crystal structure on the excitonic properties was examined by investigation of *in plane* excitonic states. It was carried out in a series of 2D perovskite compounds with a varying number of octahedra layers n within a slab, *i.e.* the varying width of a quantum well. This study was performed on the series of phenylethylammonium lead iodide compounds with general chemical formula $(PEA)_2(MA)_{n-1}PbI_{3n+1}$, where PEA indicates phenylethylammonium, MA stands for methylammonium and n indicates the number of octahedra layers. The results obtained provide valuable information about the evolution of the optoelectronic properties of 2D perovskites with increasing thickness of the quantum well, showing a transition between the 2D and 3D limits.

Chapter 2

Experimental Techniques

2.1 Investigated Samples

2.1.1 Phenylethylammonium Lead Iodide – Gallium Arsenide of Two-Dimensional Perovskites

The material system chosen for the study of exciton physics in this work is a phenylethylammonium lead iodide (PEPI). It is one of the most researched and well-known representatives of the Ruddlesden–Popper 2D lead-halide perovskite family [Kataoka 1993, Ishihara 1994, Kikuchi 2004, Zhang 2009, Kitazawa 2012, Wei 2014, Even 2015, Quan 2016, Zhai 2017]. PEPI is described by the chemical formula:

$$(\mathrm{PEA})_2(\mathrm{MA})_{n-1}\mathrm{Pb}_n\mathrm{I}_{3n+1} \tag{2.1}$$

where:

PEA	–	phenylethylammonium cation $C_6H_5CH_2CH_2NH_3^+$,
MA	–	methylammonium cation $CH_3NH_3^+$,
Pb	–	lead cation,
I	–	iodide anion,
n	–	number of octahedra layers within a crystal slab.

It forms a characteristic, layered structure, typical for 2D perovskites, where the inorganic lead iodide octahedra layers are separated by organic phenylethylamine (PEA) cations (as shown in Fig. 2.1):

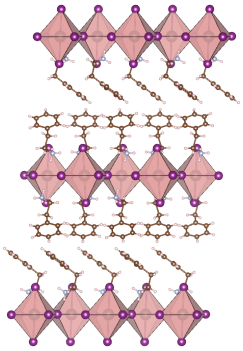

Figure 2.1: Model of a crystal structure of phenylethylammonium lead iodide n=1. Visualised using VESTA software [Momma 2011] using crystallographic data after [Du 2017].

PEPI crystallises in the triclinic crystallographic system and does not show any phase transitions between room temperature (RT) and liquid helium (LHe) temperature T=4.2 K [Du 2017]. The triclinic system is the one with the lowest symmetry, with all crystal axes being non-equivalent. This fact, together with the exchange interaction (and a possible crystal field), can result in the splitting of the exciton fine structure. At the same time, within this material system all excitonic effects are greatly enhanced due to the significant values of exciton binding energy, which reach hundreds of meV [Dyksik 2021b]. As such, PEPI is an excellent choice as a framework for the proposed investigation.

The study described in this work was carried out on high-quality single crystals of PEPI compounds, fabricated using *wet chemistry* methods. To reduce the possibility of material imperfections influencing the results of the described experimental investigations, two sets of samples were grown, using two different synthesis protocols. The first, called *cooling-induced crystallisation*, resulted in a series of PEPI compounds of n=1..4, with high phase purity and crystal quality. The protocol previously reported in the literature [Stoumpos 2016, Stoumpos 2017, Peng 2017] was modified by Paritmongkol et al. [Paritmongkol 2019], and the resulting samples were kindly shared for optical investigations by Prof. William A. Tisdale from the Massachusetts Institute of Technology. The second, *slow evaporation of a solvent*, produced high-quality crystals of the PEPI compound with n=1, and the crystals were kindly shared by Prof. Mirosaw Mączka from the Institute of Low Temperature and Structure Research, Polish Academy of Sciences.

2.1.2 Cooling-Induced Crystallisation Method

High-quality crystals can be fabricated by chemical synthesis. It is a relatively straight forward, step-by-step "benchtop" process (Fig. 2.2), which does not require an inert atmosphere. Thus, there is no need to use the Schlenk line, further simplifying the procedure. The main point of this method is to slow down the crystallisation process. In this way, the material grows with significantly fewer defects.

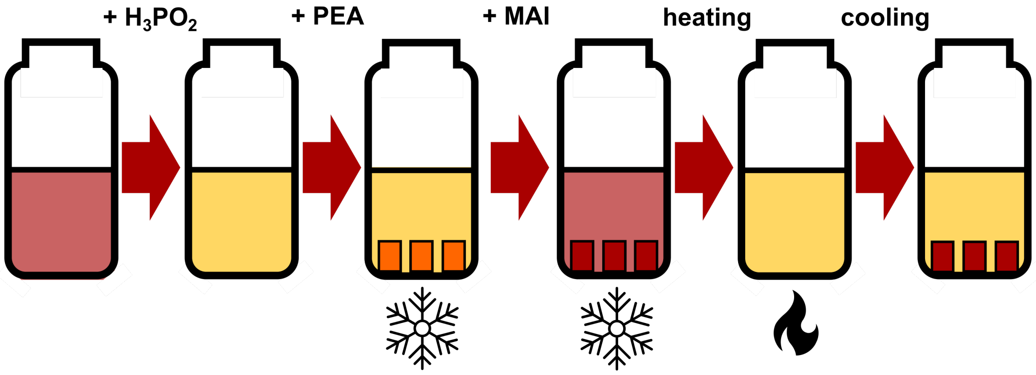

Figure 2.2: Diagram schematically depicting the process of synthesis of 2D perovskites. Adapted from [Paritmongkol 2019].

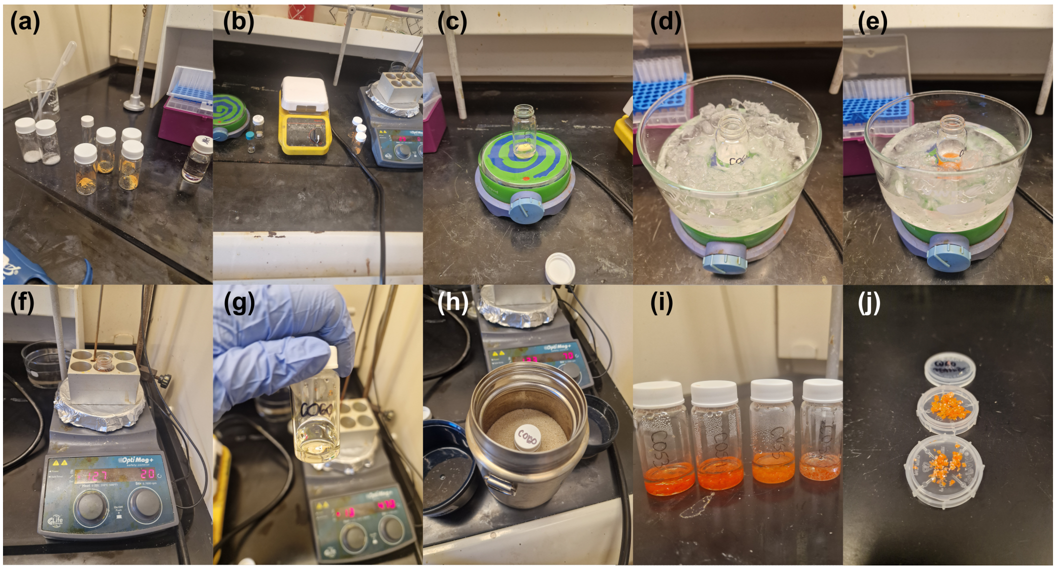

Figure 2.3: Photographs showing a synthesis procedure. Here shown for a 2D perovskite phenylethylammonium lead bromide $(PEA)_2(MA)_{n-1}Pb_nBr_{3n+1}$, however procedure is analogous for the iodide-containing compounds. (a) Precursors – lead oxide (II) and A-site cation salt weighted into glass vials, prepared for synthesis. (b) Magnetic stirrers and a hot plate used in the process. (c) Preparation of PbI_2 salt. (d) Vial placed into an ice bath, adding ligand – PEA cation. Immediate formation of crystals. (e) Adding the A-site cation salt, dissolved in a separate vial. Change of colour of the solution. (f) Heating up the solution to 130 °C until all crystals dissolve and solution becomes clear (g). (h) Vial placed in the sand bath for 24 hours, allowing slow cooling down of the solution and crystallisation of 2D perovskites. (i) Vials containing 2D perovskite crystals, retrieved after 24 h of cooling. (j) Dry crystals removed from the solution via filtration.

The synthesis protocol consists of the following steps (after [Paritmongkol 2019]):

1. Preparation of precursors (Fig. 2.3 (a), (b)); lead oxide (II) (PbO) and methylammonium iodide (MAI) are weighted out into the separate glass vials, phenylethylammine (PEA) ligand is also measured out into a vial; lead iodide (II) (PbI_2) is obtained by dissolving PbO in hydroiodic acid (HI) for 15 minutes while constantly stirring the solution (Fig. 2.3 (c)). Then, the hypophosphorus acid (H_3PO_2) is added (to ensure the reduction of any remaining iodine I_2 back to I^-). In a separate vial, MAI is dissolved in HI.

2. The vial containing PbI_2 solution, while constantly stirred, is placed into an ice bath (Fig. 2.3 (d)), to slow down the crystallisation process; at this point, phenethylamine is added into the vial and immediately the crystals of $(PEA)_2PbI_4$, *i.e.* the compound with n=1 are formed.

3. For $n \geq 2$, while in the ice bath, MAI solution is added, resulting in immediate change of colour of the mixture (Fig. 2.3 (e)); then, if needed, an additional amount of HI is added.

4. The mixture is then heated up to 130 °C while constantly stirring (Fig. 2.3 (f)), until the solution becomes clear and all crystals are dissolved (Fig. 2.3 (g)). The vial is then placed into the sand bath at 110 °C, and is allowed to slowly cool down undisturbed for 24 hours (Fig. 2.3 (h)).

5. After 24 hours, single crystals of 2D perovskites are formed (Fig. 2.3 (i)). They are removed from the solution via suction filtration and then dried under reduced pressure for at least 24 hours (Fig. 2.3 (j)).

In order to obtain high-quality, phase pure crystals of 2D perovskites, it is imperative to adjust the ratio of precursors used in the synthesis; the key parameter in this process is the precipitation rate of the crystals out of a solution.

By using the protocol described above, a series of PEPI compounds with n=1..4 were obtained. Crystals formed had flat, thin flake shape with lateral dimensions of a few millimetres (Fig. 2.4 (a)). As such, it was possible to pick them up and manipulate them using tweezers, without the need to use any elaborate transfer techniques. The crystals obtained via this method were indeed highly phase-pure, which was further confirmed via X-ray diffraction measurements (XRD, as shown in Fig. 2.4 (b)).

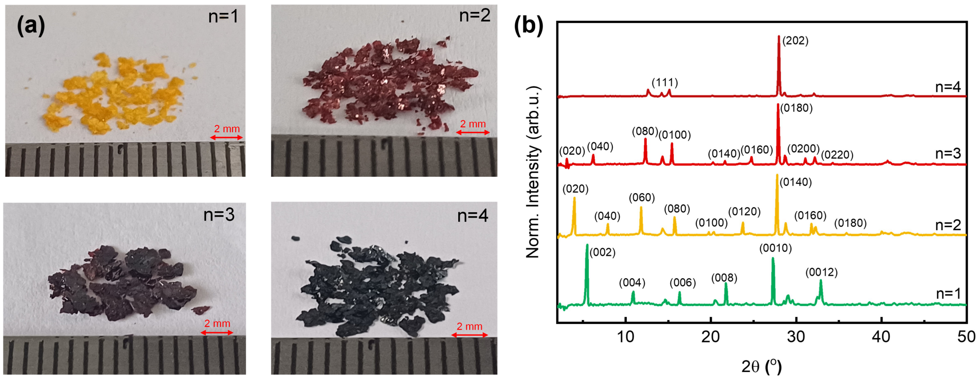

Figure 2.4: (a) Photographs showing crystals of a PEA compound series with varying n. (b) XRD showing phase purity of the synthesised materials. Adapted from [Posmyk 2024b], published under a Creative Commons Attribution (CC-BY 4.0) license.

All data presented in this work originate from optical studies on phenylethylammonium lead iodide perovskite compounds. The same synthesis procedure can be adapted to yield perovskites with varying chemical composition, depending on the precursors used. The procedure presented on photographs in Fig. 2.3 was done on the example of phenylethylammonium lead bromide, performed at Massachussetts Insitiute of Technology during the stay within 2024 Fulbright Junior Award programme. However, qualitatively, the synthesis protocol described above remains the same (sans the differences in the colours of the crystals and solutions and the amounts of the precursors).

2.1.3 Second synthesis method – slow evaporation of a solvent

In an alternative synthesis approach, reported in the work [Posmyk 2022], for obtaining PEA_2PbI_4 n=1 single crystals, PbI_2 was dissolved in hydroiodic acid along with aqueous H_3PO_2, while stirring and heating to 50 °C. Separately, phenethylamine was mixed with HI while stirring. Acetonitrile was then added until the precipitate dissolved completely. This phenethylamine solution was poured into the PbI_2 solution while stirring, after which the hot plate was turned off. As orange crystals began to form at room temperature, additional acetonitrile was added to dissolve any formed crystals. The vial was then sealed with parafilm with small holes and left undisturbed at room temperature. After one week, orange crystals up to 5 mm in size were collected from the bottom of the vial.

2.2 Optical Spectroscopy Techniques

Optical spectroscopy is a versatile and highly informative group of experimental techniques that is used to probe the optical and vibronic properties of solid-state materials. It involves a detailed analysis of the spectrum of light that has interacted with the material or been emitted by it.

Typically, the process begins with the illumination of the sample using an external light source. As the light interacts with the material, various physical processes – such as absorption, reflection, transmission, scattering, or emission – can occur, each revealing different aspects of the material's internal structure and dynamics. The resulting changes in the light's spectral composition carry valuable information about the electronic band structure, excitonic states, phonon modes, defect states, and other fundamental properties. By examining how the spectral features vary under different conditions – such as temperature, magnetic field, or polarisation – it is possible to gain a deeper insight into the material's behaviour. These interactions and their spectroscopic signatures are often described through well-established physical models [Fox 2010].

2.2.1 Photoluminescence

When a semiconductor is driven out of equilibrium, for instance, by incident electromagnetic radiation or by carrier injection, it naturally tends to return to equilibrium. This occurs through two primary mechanisms (Fig. 2.5):

- **Relaxation processes**: excited carriers lose energy and move toward the lowest available energy states within their respective bands.

- **Recombination processes**: electrons recombine with holes, returning to the valence band.

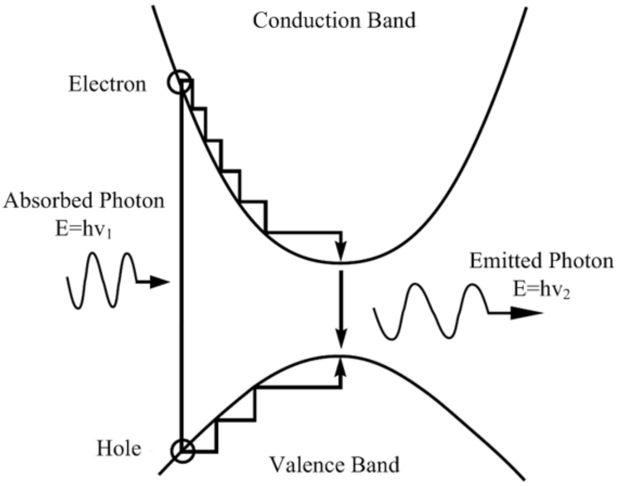

Figure 2.5: Schematic depiction of relaxation and recombination processes. Adapted from [Min 2018].

If recombination results in the emission of a photon, the process is called **radiative recombination**. When this photon emission follows excitation by external electromagnetic radiation, the process is known as **photoluminescence (PL)**.

Radiative recombination in semiconductors can occur through several distinct mechanisms [Yu 2010]:

1. **Band-to-Band Recombination**
   Electrons excited from the valence band to the conduction band can recombine with holes. Since photons carry negligible momentum, radiative recombination is allowed only between electron and hole states with the same wavevector **k** [Singh 2007], as mentioned above in the 1.3.2.

   Although, in principle, recombination can occur throughout the band structure, relaxation within a band is generally much faster than recombination. Consequently, radiative transitions predominantly occur at the band edges. Band-to-band recombination is a *bimolecular process* and becomes inefficient at low carrier densities. It tends to dominate only when *excitonic recombination* is suppressed – for example, when the thermal energy $k_B T$ exceeds the exciton binding energy, as is common in III–V semiconductors at room temperature [Adachi 1992].

2. **Excitonic Recombination**
   Excitonic recombination refers to the radiative decay of a bound electron-hole pair, known as an exciton. This is a *monomolecular process* and is typically more efficient due to the high density of excitonic states [Yu 2010].

The strength of the optical transition for excitons is inversely proportional to their spatial extent:

$$\text{Transition strength} \propto \begin{cases} 1/a_B^3 & \text{(3D systems)} \\ 1/a_B^2 & \text{(2D systems)} \end{cases}$$

where a_B denotes the Bohr radius of the exciton. In materials with strongly bound excitons – such as 2D perovskites – these effects dominate the optical response.

Only excitons with centre-of-mass momentum $\mathbf{K} = 0$ are optically active, which leads to discrete emission and absorption spectra, although excitonic states form a continuum [Singh 2007].

3. **Recombination via Impurities or Defects**
   Radiative recombination can also take place via localised states introduced by impurities or structural defects, including:

   - transitions between conduction or valence band states and donor or acceptor levels,
   - recombination between donor and acceptor states,
   - and recombination involving defect-bound excitons.

   These processes are most prominent at low temperatures and under weak excitation. At higher excitation powers, such localised states may become saturated, diminishing their contribution to the emission spectrum [Yu 2010].

PL is a widely used, non-invasive, and non-destructive technique for studying the optical properties of semiconductors. Its versatility makes it suitable for a broad range of materials and conditions. However, the PL spectrum can be influenced by several factors [Pelant 2012]:

- carrier relaxation dynamics,
- non-radiative recombination mechanisms,
- and the presence of defects or impurity states.

PL predominantly probes the lowest-energy transitions, often resulting in a **Stokes shift** – an energy difference between absorption and emission peaks. To interpret PL data reliably and identify relevant optical transitions, it is a good practice to compare PL results with absorption spectra.

2.2.2 Absorption

Unlike PL, which predominantly probes the lowest-energetically states of a system, **absorption measurements** provide information about electronic states with a high joint density of states. Therefore, it is a complementary measurement to photoluminescence measurements.

In general, the absorption coefficient $\alpha(E)$ is proportional to the joint density of states $D(E)$ and the square of the modulus of the optical transition matrix element [Yu 2010]:

$$\alpha(E) \propto D(E) \cdot |M_{cv}|^2 \tag{2.2}$$

Assuming that the matrix element M_{cv} remains approximately constant near the band edges, the behaviour of the absorption near the energy gap depends on the dimensionality of the system:

- **3D crystals** (with parabolic band dispersion):

  $$\alpha(E) \propto \sqrt{E - E_g}$$

- **2D crystals or quantum wells** (with parabolic bands):

  $$\alpha(E) \propto \Theta(E - E_g)$$

  where:

  Θ – the Heaviside step function,
  E_g – the energy band gap,

- **Excitonic transitions**: For bound exciton states, which are discrete in nature, the absorption spectrum exhibits peaks corresponding to a discrete density of states:

  $$\alpha(E) \propto \delta(E - E_X)$$

  In real materials, however, these peaks are broadened due to various interactions, causing the spectral lines to adopt Gaussian or Lorentzian profiles.

  Moreover, strong excitonic effects may modify the fundamental absorption edge, changing its typical square-root dependence to a more step-like form.

The **complex refractive index** describes both refraction and absorption of light in a medium, and is defined as [Fox 2010]:

$$\tilde{n} = n + i\kappa, \tag{2.3}$$

where:

n – refractive index,
κ – extinction coefficient.

The real part, $n = c/v$, describes the reduction of light velocity in the medium (compared to the speed of light in vacuum, c), while the imaginary part, the extinction coefficient κ, is directly related to the absorption coefficient:

$$\alpha = \frac{2\kappa\omega}{c} = \frac{4\pi\kappa}{\lambda}, \tag{2.4}$$

with λ the free-space wavelength.
The real part, the refractive index, is defined as $n = \frac{c}{v}$, describes the reduction of light velocity v in the medium (compared to the speed of light in vacuum, c). The imaginary part of $\tilde{n}$, the extinction coefficient κ is directly related to the absorption coefficient α of the medium, defined by the relation:

$$\alpha = \frac{2\kappa\omega}{c} = \frac{4\pi\kappa}{\lambda} \tag{2.5}$$

where:

λ – wavelength in free space.

When direct absorption measurements are not feasible, for example, if the sample is thick and strongly absorbs incident photons, valuable information about regions of high density of states in the band structure can be obtained from analysing the light reflected from the surface of the sample – **reflectance**. It can be defined as a ratio of the light reflected from the surface to the light incident to it. In other words, it is a coefficient of the reflection between the medium and air/vacuum at normal incidence, including both refraction and absorption of light in the medium:

$$R = \left|\frac{\tilde{n}-1}{\tilde{n}+1}\right|^2 = \frac{(n-1)^2+\kappa^2}{(n+1)^2+\kappa^2}. \tag{2.6}$$

Since the refractive index is related to the dielectric function by the relation:

$$\tilde{n}^2 = \tilde{\varepsilon}_r, \tag{2.7}$$

where the complex dielectric function is defined as:

$$\tilde{\varepsilon}_r = \varepsilon_1 + i\varepsilon_2, \tag{2.8}$$

the real and imaginary parts of the dielectric function are related to both refraction and absorption:

$$\varepsilon_1 = n^2 - \kappa^2, \tag{2.9}$$

$$\varepsilon_2 = 2n\kappa. \tag{2.10}$$

According to both quantum-mechanical band theory and classical models based on damped oscillators, the dielectric function near discrete electronic transitions adopts a resonant form:

$$\tilde{\varepsilon}(E) = 1 + \chi + \frac{f}{E_0^2 - E^2 - i\Gamma E} \tag{2.11}$$

where:

χ – background contribution from remote transitions,
f – oscillator strength of the electronic transition,
E_0 – energy of the optical transition,
Γ – linewidth (accounts for spectral broadening).

This resonant behaviour gives rise to characteristic features in both the real (ε_1) and imaginary (ε_2) parts of the dielectric function (Fig. 2.6, left), and consequently affects the refractive index $n(E)$ and the extincion coefficient $\kappa(E)$ (Fig. 2.6, right). In particular, materials exhibiting strong excitonic oscillator strengths display well-defined resonances in their reflectance spectra corresponding to excitonic transitions.

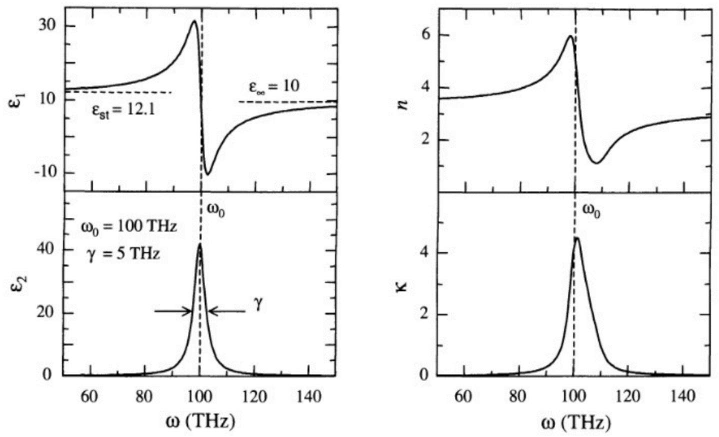

Figure 2.6: The real and imaginary parts of the complex dielectric function near the energy of the optical transition (left), as well as the refractive index n and extinction coefficient κ. Adapted from [Fox 2010].

Although the reflectance spectrum is not strictly described by the exact form of $\varepsilon_1(E)$, it often closely resembles it in practice. In this framework:

- The transition energy can be identified with the point of maximum slope on the resonance curve.
- Calculating the derivative of the reflectance spectrum, $\frac{\mathrm{d}R}{\mathrm{d}E}$, provides a practical method to determine transition energies, often with precision comparable to that of absorption measurements.

2.3 Experimental Setup

2.3.1 Micro Configuration

Photoluminescence and reflectance measurements are performed in a custom-built experimental setup, consisting of parts optimised for the visible range of the electromagnetic spectrum. It is schematically depicted in Fig. 2.7. Excitation is provided by two light sources:

- A Quixx **continuous-wave** (CW) **laser** with a wavelength of 405 nm,
- A Thorlabs tunsten-halogen **white light source**.

The laser beam or white light are directed onto the sample using silver mirrors (Thorlabs). The excitation power is then adjusted by using variable density filter (Thorlabs) and kept constant throughout the whole series. The excitation beam is then directed onto a 50:50 non-polarising beam splitter (BS, Thorlabs); half of the beam is reflected down towards the sample and focused on it using the 50x microscope objective (M Plan Apo, Mitutoyo) with numerical aperture NA=0.55. The other half of the beam is transmitted through the BS and directed to a power meter (Thorlabs).

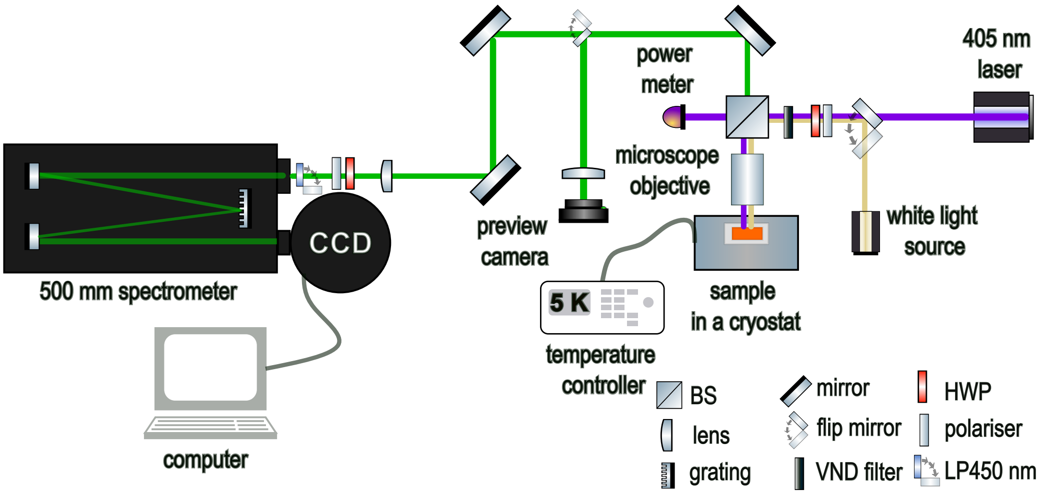

Figure 2.7: Schematic depiction of the experimental setup, allowing the measurements with micrometric resolution in the temperature range 4.2-300 K.

The samples were placed inside a flow-type cryostat cooled with liquid helium (Microstat HiRes cryostat, Oxford Instruments). Together with the temperature controller (Mercury iTC temperature controller, Oxford Instruments), this enables measurements in the 4–300 K temperature range. Thermal contact is ensured through the use of the silver paste to mount the samples onto the so-called “cold finger” of the cryostat. The cryostat was placed onto the XY translation stages (Standa), which allowed to adjust the position of the sample in the setup. The focus of the objective was adjusted using a separate Z stage.

This setup is configured in so-called “back-scattering geometry”, so the photoluminescence signal from the sample or the reflected white light is collected back by the same objective, then transmitted through the beam splitter, directed by the silver mirrors and focused on the slit of the monochromator using a lens (BK-7, Thorlabs). An appropriate long-pass filter (450 nm, Thorlabs) is placed right in front of the slit to remove the exciting laser and protect the detector in case of the PL measurement.

Main signal detection is carried out using a liquid nitrogen-cooled CCD camera, with a quantum efficiency of 98% (PyLon 400BR eXcelon, Princeton Instruments). The camera is mounted on the monochromator (HRS-500, Princeton Instruments), allowing for spectral separation of the detected signal. It is optimised for the visible spectrum, with a focal length of 50 cm and fitted with three diffraction gratings:

- 300 grooves/mm, blaze at 750 nm,
- 600 grooves/mm, blaze at 500 nm,
- 1200 grooves/mm, blaze at 500 nm.

These components facilitate high spectral resolution, which is essential for the resolution of the excitonic fine structure in photoluminescence and reflectance measurements. With the 1200 grooves/mm grating at 500 nm, the achievable spectral resolution is 0.05 nm, corresponding to an energy resolution of $\Delta E = 248\,\mu$eV.

All measurement series in this work were performed in "micro mode" – that is, a microscope objective was used to focus the laser beam (or white light) on the sample and to collect the signal from the sample. This allows for obtaining an optical response from the area of the sample in the size of single micrometers (for the objective used in this study, the diameter of the focused laser spot is about 0.9 μm for an excitation wavelength of 405 nm).

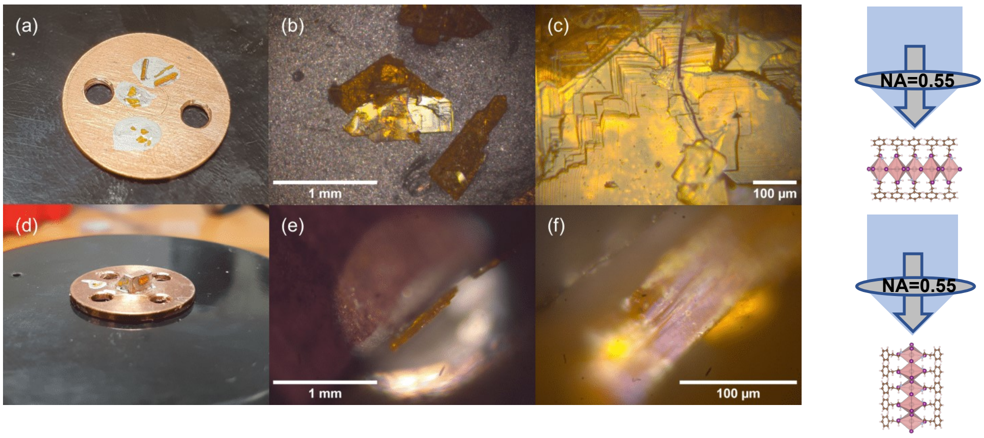

Figure 2.8: Optical images of investigated $(PEA)_2PbI_4$ crystal. Top part: crystals mounted in a "planar" configuration, with signal collected from the surface of the sample. Bottom part: Crystals mounted parallel to the incident beam, signal collected from the edge of the sample – this is an "edge" configuration. Adapted from [Posmyk 2024a].

As described in the section 1.4, the main objective of this work was to examine the exciton fine structure of 2D lead-halide perovskite. As the specific excitonic states couple to linearly polarised light oriented in three different dimensions, different geometries of the experiment are required to access all of them. By using custom mounting copper plates and owing to the relatively large sizes (milimeters) of investigated crystals, it was possible to collect the optical response not only from the surface of the crystal flakes (Fig. 2.8, top – "planar" configuration), but also from the edge of the crystal (Fig. 2.8, bottom – “edge” coonfiguration). As the laser spot is the size of single micrometers (less than 1 μm for 405 nm laser, few μm for white light beam in this specific setup), it was possible to accurately focus the incident beam on the flat part of the crystal in both experimental configurations. This allowed for investigation of all excitonic states in three dimensions, and access the previously not observed bright state $|Z\rangle$ state, with dipole moment oriented *out of plane* of the crystal.

2.3.2 Polarisation-Resolved Measurements

As described in the subsection 1.3.5,in the context of exciton fine structure, in systems with sufficiently low symmetry, the energy degeneracy of excitonic states can be entirely lifted. In such cases, excitons emit or absorb light with a well-defined linear polarisation. As a result, polarisation-resolved measurements are crucial for investigating the fine structure of excitonic states. In this study, polarisation-resolved photoluminescence and reflectance measurements were performed using a combination of a linear polariser (Thorlabs) and a half-wave plate (HWP, B.Halle).

The half-wave plate rotates the linear polarisation of the incident light by an angle of 2θ, where θ is the angle between the wave plate’s fast axis and the incoming polarisation, as shown in Fig. 2.9 [Optics , Thorlabs]. The beam then passes through a polariser which is oriented to transmit the polarisation that yields maximum signal on the spectrometer.

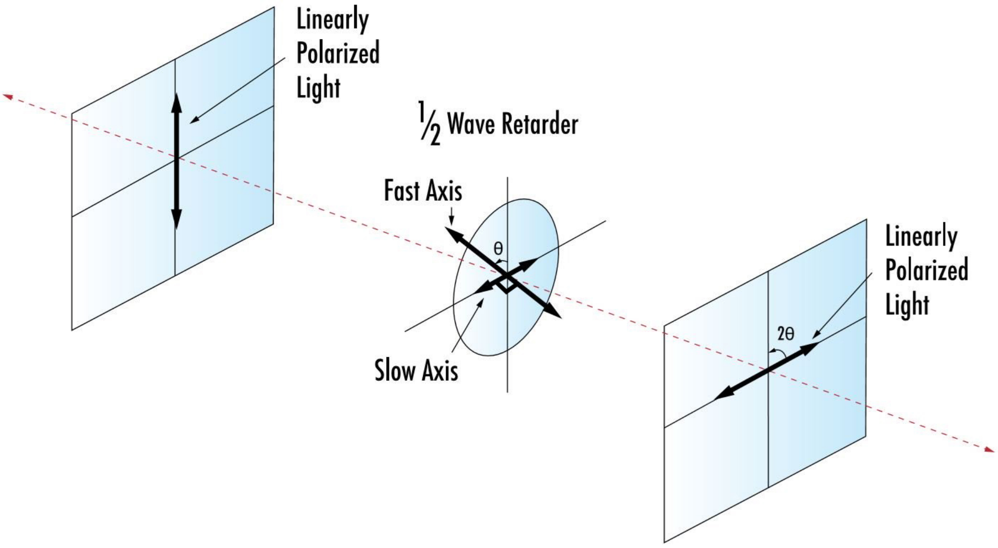

Figure 2.9: Principle of rotating the linearly polarised light using the combination of half wave plate (HWP) and linear polariser. Adapted from [Optics].

By rotating the half-wave plate, the polarisation of the emitted light is varied relative to the polariser axis. This alters the transmission through the polariser, thereby modulating the detected intensity. For certain orientations of the wave plate, the signal for a particular emission line is maximised; for others, it may be minimised or fully suppressed. This approach enables the determination of the relative polarisation orientations of individual spectral features. In systems where a fine structure of bright excitonic states is present, these states are typically expected to be orthogonally polarised. It was schematically depicted in Fig. 2.9.

However, if the goal of the measurement was to observe the signal from the sample excited with the light linearly polarised in various directions, then the polariser is placed right in front of the excitation source and oriented to maximise the transmitted power. HWP is placed afterwards and rotated to change the orientation of the polarisation.

Both placements of the polarisation optics were depicted in Fig. 2.7.

Converting Between Linear and Circular Polarisation

As described in subsection 1.3.6, the excitonic states with dipole moments oriented *in plane* of the crystal, non-degenerate in energy and linearly polarised, change their properties when the external magnetic field is applied [Kataoka 1993, Yu 2016]. The exchange interaction warranted mixing between the $|\psi_3\rangle$ and $|\psi_4\rangle$ states is suppressed, and the states gain back the circular polarisation. Thus, while performing magneto-optical spectroscopy measurements, instead of linear, circular polarisation of the signal was investigated.

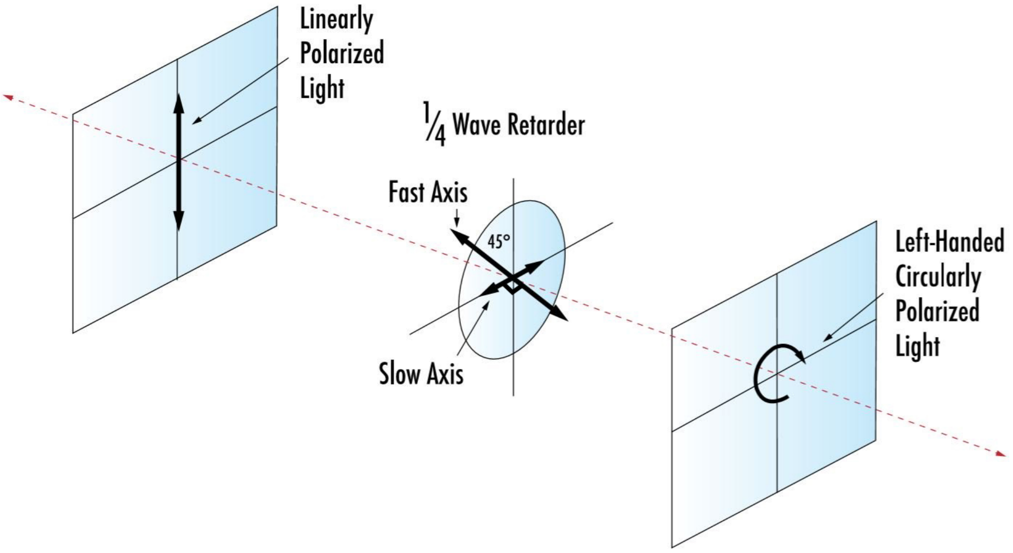

Figure 2.10: Principle of obtaining the circularly polarised light using the quarter wave plate (QWP). Adapted from [Optics].

A quarter-wave plate ($\lambda/4$, QWP) can convert linearly polarised light into circularly polarised light, and vice versa, depending on its orientation. When linearly polarised light enters a $\lambda/4$ wave plate at an angle of 45° to its fast axis, the emerging light becomes circularly polarised. Conversely, circularly polarised light passing through a $\lambda/4$ wave plate is transformed into linearly polarised light, oriented at 45° to the wave plate's axis.

If the incident polarisation is at an angle other than 45°, the resulting light becomes elliptically polarised. Thus, the final polarisation state – whether circular, linear, or elliptical – is determined by the orientation of the incoming polarisation relative to the wave plate's axes. Schematic of the process was shown in Fig. 2.10.

2.3.3 Magnetic Field Measurements

Magnetophotoluminescence (magneto-PL) and magnetoreflectance (magneto-R) were performed in collaboration with the group of prof. Adam Babiński with prof. Maciej Molas from the Faculty of Physics at University of Warsaw, within the ISABEL project of European Magnetic Field Laboratory.

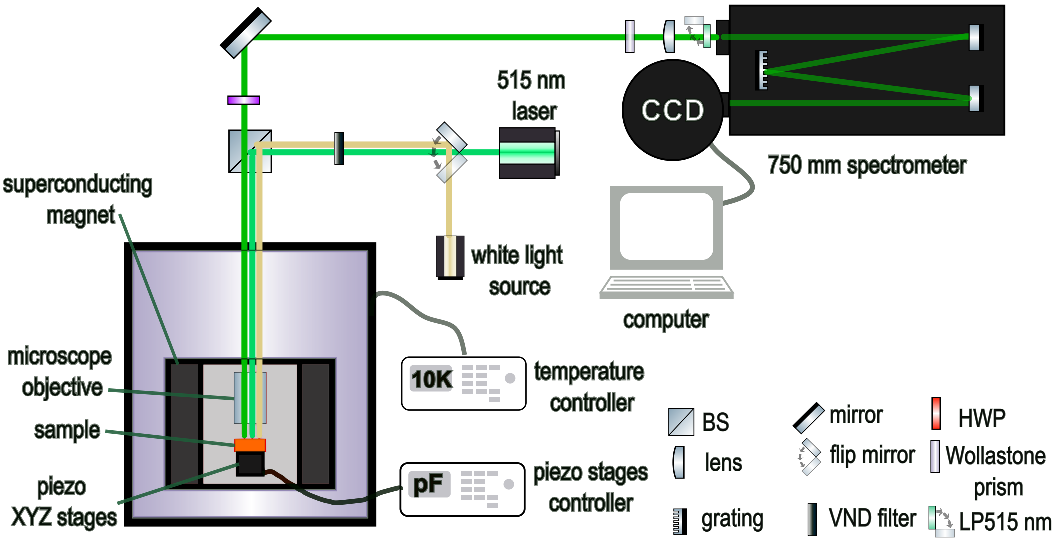

Figure 2.11: Schematic depiction of the experimental setup with superconducting magnet, allowing the measurements with micrometric resolution in the static magnetic field up to 12 T. Measurements in this work were performed at T=10 K.

The measurements were performed in the Faraday configuration at a temperature of 10 K, using a superconducting magnet capable of generating static magnetic fields up to 16 T (Oxford Instruments). The coil of the magnet is cooled by the liquid helium and kept at superconducting state throughout the field sweep. The experimental setup is depicted in Fig. 2.11. The sample was mounted on a custom-made probe, along with all necessary instruments and optical elements, and inserted into the cryostat placed within the coil of the magnet. The material is excited using a CW 515 nm laser, which was directed onto a 30:70 beam splitter (Thorlabs). The beam was reflected down into the cryostat and focused on the surface of the sample with a microscope objective of numerical aperture NA=0.82 (Attocube). The position of the sample was controlled by using the XYZ translation piezo stages (Attocube). The emitted light was collected by the objective, passed through the quarter wave plate (QWP), then directed by silver mirrors towards the spectrometer. The signal was passed through a Wollaston prism (Thorlabs) in order to spatially separate the two circular polarisations, and two resulting polarisation-resolved beams were focused on the slit of the monochromator (HRS-750, Princeton Instruments) by a lens (BK-7, Thorlabs). An appropriate long-pass filter was mounted in front of the slit to protect the detector. The signal was spectrally separated by using 1800 gr./mm diffraction grating, and directed onto a liquid nitrogen-cooled CCD camera. Two polarisation-resolved signal beams were detected simultanously from two separate regions of interest (ROI) on the CCD chip.

Chapter 3

Exciton Fine Structure

The topic of the exciton fine structure in 2D perovskites is very relevant from the point of view of potential practical applications of 2DP, such as light emitters. As previously described in subsection 1.3.5, it has been debated in the literature, however the reports were at times conflicting, the discrepancies especially in the specific excitonic states' energetic order. This work attempts to resolve the issue, by experimental determination of the energy and order of the fine structure states.

In this chapter, the results of optical spectroscopy investigations, obtained specifically for PEPI compound with n=1, are shown. This compound is the "thinnest" of the n series, and closest to the 2D limit. Single crystals of $(\mathrm{PEA})_2\mathrm{PbI}_4$, in a form of thin milimeter-sized flakes, obtained by two different synthesis methods, were examined to exclude the influence of any material defects on the experimental results. The results of the two experimental series carried out on two batches of high-quality single crystals, grown by two diefferent synthesis protocols, are consistent with each other, which confirms their validity. Throughout this chapter, most of the results shown were obtained from crystals grown via cooling-induced crystallisation. The results of the alternative batch of samples, grown by slow evaporation of a solvent, are shown in the last section 3.5.

Different variations of the photoluminescence and reflectance measurements were performed under varying conditions to characterise the optical response of the material. Then, detailed polarisation-resolved measurements were carried out to address the bright states of the exciton fine structure. Finally, a magneto-optical study was carried out in order to obtain information about the remaining dark state of the exciton and determine how the excitonic properties evolve in the magnetic field.

3.1 Optical Response from $(\mathrm{PEA})_2\mathrm{PbI}_4$

The optical response of PEPI compounds was studied by measuring photoluminescence and reflectance from the surface of the sample crystal kept at T=4.2 K. The obtained spectra are shown in Fig. 3.1 (a). At low, cryogenic temperature, photoluminescence is bright even under relatively low excitation power (around 1 μW). The PL emission is centred around 2.351 eV (527 nm) and quite complex, consists of multiple peaks with spectral width of singular meV. The intensity of the PL scales linearly with the excitation power for all lines visible in the spectrum, as shown in Fig. 3.1 (b). This suggests the monomolecular – excitonic – origin of the emission. At the same time, linear power dependence of all lines present in the spectrum, as well as lack of any energy shift in the emission (Fig. 3.1 (c)), points against other origins, such as recombination of trions, biexcitons or defects. Possible explanations include emission from different states of the exciton fine structure or from the states formed as the charge carriers interact with soft, ionic crystal lattice – formation of polarons. Closer investigation of the photoluminescence spectra is one of the topics addressed by this work.

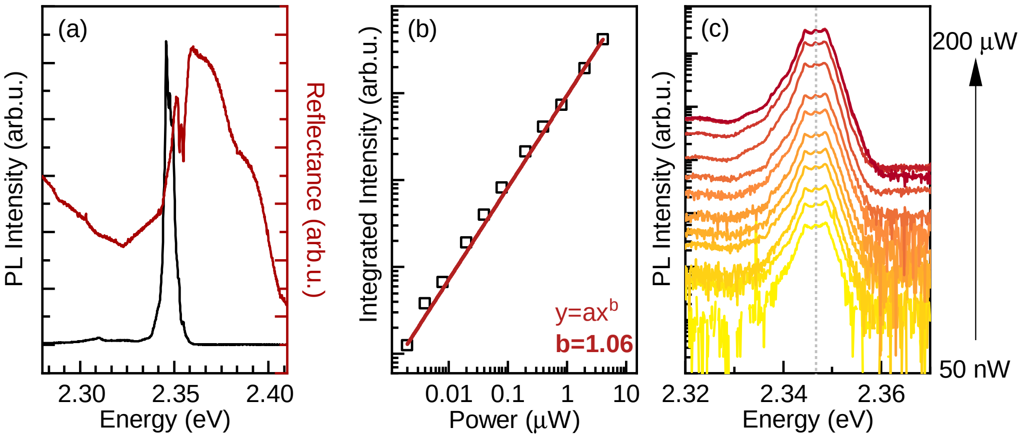

Figure 3.1: Basic optical characterisation of investigated single crystals of PEPI n=1 compound, grown by cooling-induced crystallisation method. (a) PL and Reflectance spectra obtained at T=4.2 K. (b) Integrated PL intensity as a function of the excitation power, showing linear dependence. Red line is an allometric fit to the data points, power exponent b value close to unity shows linear dependence. (c) PL spectra as a function of the excitation power. Intensity displayed in logarythmic scale. Gray dotted line is a guide to the eye, showing no energy shift of the PL emission.

Looking at the temperature dependence of the emission from PEPI (Fig. 3.2) in the range 4.2-300 K, there is quite an interesting behaviour, deviating from what is typically observed for the III-V semiconductors, but typical for LHP. In case of the "classical" semiconductors, such as sillicon or gallium arsenide, the energy band gap is reduced as the temperature increases. It is caused by two effects:

- band-gap renormalisation depending on the phonon occupation (thermal vibrations); it is described by Bose-Einstein oscillator model, and this approach was succesfully fitted to the experimental data [O'donnell 1991];
- effect related to the thermal expansion: when the crystal heats up, its lattice constant a increases. This reduces the overlap between orbitals forming valence and conduction bands, consequently reducing the interaction between the bonded atoms in the crystal and leads to decreased band splitting and further band gap reduction [Singh 2007, Yu 2010].

However, the 2DP does not follow this strictly-redshift-behaviour. There are two antagonistic effects in place: in the temperature range of 4.2-150 K, instead of the “typical” redshift, the emission is blueshifting. It is an effect directly related to the band structure of MHP, which was described in the section 1.2. As the conduction band edge is the spin-orbit split-off band, with increasing temperature, the effect of spin-orbit splitting is reduced, effectively bringing the band edge higher in energy, opening the band gap. However, it is an effect dominating only until a certain temperature threshold (approx. 150 K), above which the the energy of the emission is decreasing and the effects related to electron-phonon coupling and lattice expansion are dominating and dictating the behaviour.

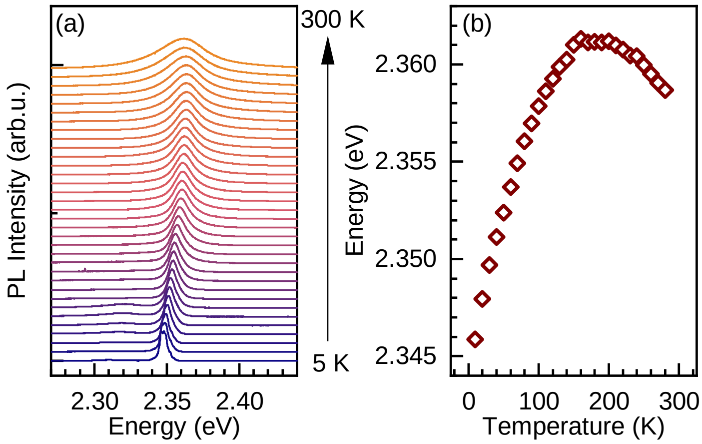

Figure 3.2: (a) Temperature dependence of the PL. (b) The energy of the emission vs the temperature. Both are showing behaviour typical for perovskites – initial blueshift of the emission’s energy, followed by the redshift related to the thermal expansion of a crystal lattice above 150 K.

The effects related to the temperature are not the main focus of this thesis. However, it is worth showing this dependence, as it brings two valuable pieces of information, namely:

- the peculiar temperature dependence of the emission displayed by the PEPI compound is the same as in previously studied LHP materials [Even 2013];
- within the studied temperature range, PEPI n=1 compound does not undergo any phase transitions. It is relevant in the context of previously described complex PL spectrum – the multiple lines present in spectra are not likely to originate from different crystal phases.

The reflectance spectra measured at T=4.2 K are not as complex as PL, however they bring a key information about the energy of free excitons in this 2DP compound. As shown in Fig. 3.3 (a), above the energy of the intense green emission, there are two clear resonance-like features, separated roughly by 2 meV. There is a clear Stokes shift between main PL emission peak and the features in the reflectance.

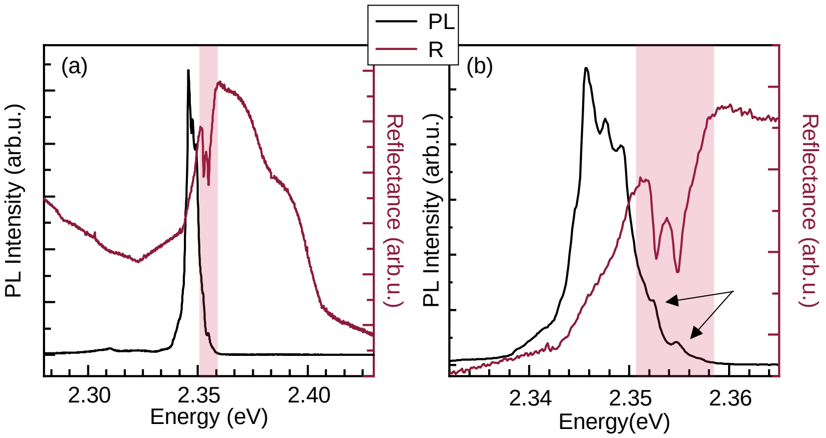

Figure 3.3: Comparison of photoluminescence and reflectance (R) spectra measured from PEPI n=1 compound at T=4.2 K shown in (a) broader energy range, and (b) in more narrow energy range, focused on the main observed optical transition. Arrows point to the two emission peaks on the high energy side, corresponding to the two features observed in reflectance spectrum. Shaded areas indicate the region of interest, around the free excitonic transition FX.

However, if the crystalline quality of the investigated sample is sufficiently high, on the high energy side of the PL spectrum there are two well resolved peaks visible (Fig. 3.3 (b), indicated by arrows). Although of lower intensity than the main emission, these two peaks are of the same energy as the features in the reflectance, with the same energy separation between them. The energy matching and exact same value of the splitting suggest that these well-resolved features originate from the free excitons (more specific, from two separate states of the exciton fine structure). This claim is further confirmed by the linear polarisation-resolved study in the following section. Here, in Fig. 3.3, spectra were collected from the surface of the sample, without polarisation optics. Thus, in this experimental configuration (“planar”, as shown in Fig. 2.8), light couples to the *in plane*-oriented states, and both these transitions appear simultaneously.

3.2 Polarisation-Resolved Measurements

In order to address specifically the bright states of the exciton fine structure, which couple to the light polarised linearly in three orthogonal dimesions (as described in subection 1.3.5), both photoluminescence and reflectance measurements were performed with the use of linear Glan polariser and a superachromatic half-wave plate (HWP), as described in the subsection 2.3.2. The polarisation optics was placed in the detection part of the setup (Fig. 2.7). Furthermore, the measurements were made with a microscope objective with relatively low numerical aperture (NA = 0.55), which mainly detects the *in plane* oriented states.

All of the results presented below, for both PL and reflectance measurements, were obtained at the low temperature of T=4.2 K and at low excitation power of P=1 μW, to exclude any influence of the possible local heating of the sample surface and avoid the degradation of the material. All measurements were performed repeatedly (at least three times from different spots on the crystals; from each of three spots, both PL and reflectance were measured as a function of the polarisation angle), to ensure that the results obtained are reproducible.

3.2.1 Reflectance

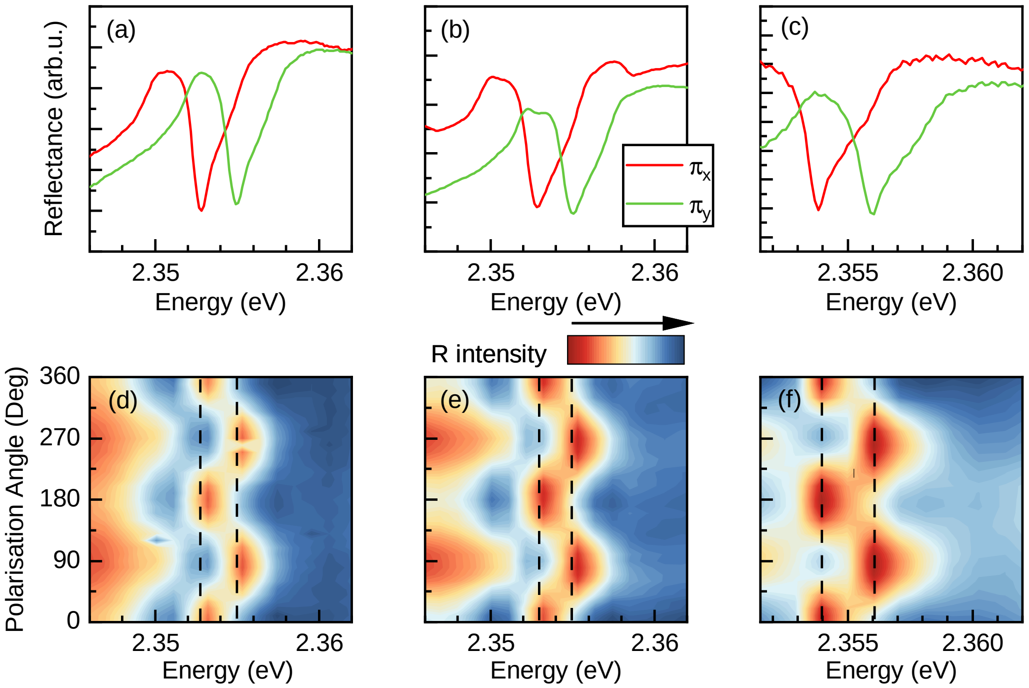

Figure 3.4: Signature of the two bright *in plane* states of the exciton fine structure. (a-c) Comparison of the reflectance spectra obtained for two orthogonal linear polarisation of light, showing that the two resonant-like features in the R spectrum are polarised differently and orthogonal to each other. Each panel show the results obtained from different spots on a sample. (d-f) Full linear polarisation dependence of the reflectance spectrum on the polarisation angle. Black dashed lines indicate the energies of two excitonic transitions.

The polarisation-resolved reflectance spectra are shown in Fig. 3.4 (a-c). These panels show results obtained from three different spots on a sample. All of them clearly demonstrate the fine-structure splitting (FSS) of bright *in plane* excitonic states. By the appropriate choice of the two spectra recorded under two orthogonal polarisations – π_x (red line) and π_y (green line) – the two free excitonic (FX) resonances can be easily distinguished, and fully separated into one or the other spectrum. Their behaviour follows theoretical predictions for two linearly polarised transitions. As the degeneracy of the excitonic states is fully lifted, they are expected to selectively couple to the linearly polarised light aligned with the dipole moment of each state. This is according to the description of the exciton fine structure shown in this work, as well as in the literature [Tanaka 2005, Sercel 2025].

The splitting between the bright exciton states FX_X and FX_Y can be well resolved and is about 2.1 ± 0.1 meV, much larger than what is typically seen in 3D perovskites. There, it is order of magnitude less, which was reported to be 200 μeV by [Baranowski 2019a]. This larger value for 2DP is expected, because excitons have higher binding energy and stronger overlap of electron and hole wave functions, which increases exchange interaction between them [Tanaka 2005, Srimath Kandada 2020, Hansen 2023]. To confirm that indeed the two orthogonal transitions are present, the reflectance as a function of the the detection polarisation angle was measured (as shown in Fig. 3.4 (d-f)). The spectrum's intensity and shape change in an oscillating way for each recorded dataset, alternating between the two energy values. It is the signature of two split, linearly polarised exciton states contributing differently depending on the orientation of the HWP. Data shown in Fig. 3.4 (a) and (d) are measured from the Spot 1, (b) and (e) from Spot 2, and (c) and (f) from Spot 3 on the sample.

3.2.2 Photoluminescence

Polarisation-resolved PL measurements were also performed to obtain more information about the origin of multiple lines present in the low temperature spectrum. In Fig. 3.5 (a-c) there are PL spectra measured under two orthogonal linear polarisations. It is clear that the peaks on the high energy side of the emission are linearly polarised – depending on the orientation of the polarisation, one of these transitions (indicated in Fig. 3.5 (a-c) as FX) is strongly supressed. Moreover, these FX peaks correspond to the features in the reflectance both in energy and the orientation of the polarisation axis. The lower-energy transition, FX_X visible in π_x polarisation (red line), is more intense than energetically higher FX_Y (green line), which reflects the thermal population of excitons between the two in-plane states X and Y.

The spectral lines originating from excitonic recombination exhibit a Lorentzian line shape at low temperature, as the broadening of the line is mostly homogenous, caused by a finite lifetime of the emission. Here, the experimental data can be well fitted with a Lorentz function, since at low temperature and in high-quality crystals, the disorder contribution is weak, so the intrinsic lifetime-limited Lorentzian dominates [Meltzer 2005]. As both of the FX features are located on the high-energy slope of the most intense emission peak in the spectrum, it was treated as a background and subtracted from the data to eliminate its influence on the intensity. The examples of the fitting are shown in Fig. 3.5 (d-f). These are shown for the dataset from Spot 1, shown here on panel (a); all of the measured datasets were analysed the same way. The intensity obtained from this analysis reveal a characteristic, double-lobe pattern for each state in the polar plot, as shown in Fig. 3.5 (g-i)). It can be fitted with a $\cos^2(\phi + \delta)$ function, where ϕ is the angle of the analyser (more specifically, double the angle between fast axes of the HWP and polariser, as described in subsection 2.3.2). δ is a phase shift factor, introduced to account for a certain orientation of the crystal in the experimental setup, and the orientation of the crystal axes with regards to the linear polarisation axis. This confirms the linear polarisation of the observed states, and the 90° phase difference between the two peaks proves their orthogonality.

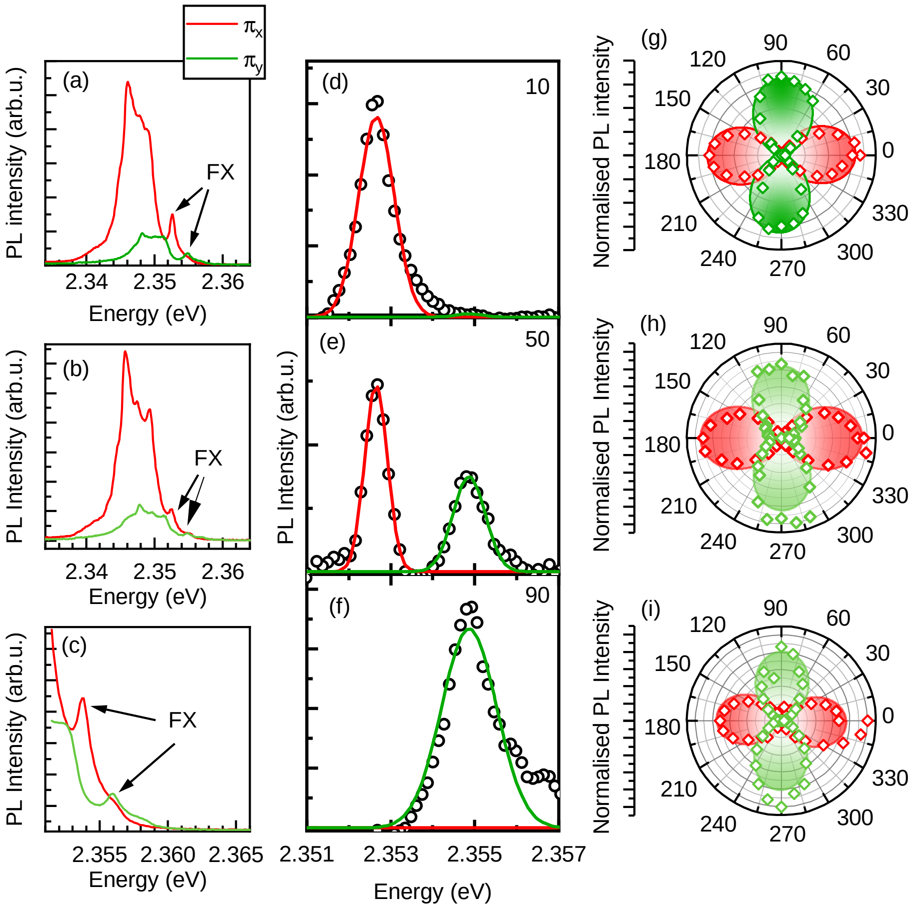

Figure 3.5: Polarisation-resolved photoluminescence measurements. (a-c) PL spectra obtained for two orthogonal polarisations. (d-f) Examples of a fitting FX_X and FX_Y PL peaks with Lorenz function at different detection polarisation angles, shown for the dataset from Spot 1. (g-i) PL intensity of the two FX transitions as a function of the polarisation detection angle.

Data shown in Fig. 3.5 (a), (b) and (g) are from the Spot 1, (b) and (h) from Spot 2, and (c) and (i) from Spot 3 on the sample. Dataset from Spot 3 was measured with centre of the spectral window shifted to the higher energy, in order to push the intense emission peak out of it and focus solely on the emission from the FX.

The dominant PL emission in the spectra, redshifted with regards to the FX transition, also exhibits the linear polarisation dependence. It behaves the same way as the emission from FX, clearly blueshifting and decreasing in intensity when the detection polarisation is changed from π_x to π_y. The redshifted PL band still preserve the selection rules and fine structure of the "bare", in-plane oriented free excitons. In fact, it evolves in intensity and energy in the same way as the FX states. Under π_y polarisation, all PL features are blueshifted by 2.1 meV relative to π_x polarisation and are weaker in intensity, yet the overall spectral shape remains the same for both polarizations. This is illustrated in Fig. 3.6, where the π_y spectrum (normalized to equalize the FX intensities) is shifted by 2.1 meV to align with the π_x spectrum. The near-identical structure and broadening of the two spectra confirm that the dominant PL originates from free in-plane excitonic transitions. This is a reproducible result, observed in the spectra obtained from both experimental Spot 1 (Fig. 3.6 (a)) and Spot 2 (Fig. 3.6 (b)). However, because the emission bands partially overlap, a precise analysis of intensity versus polarisation angle is not possible.

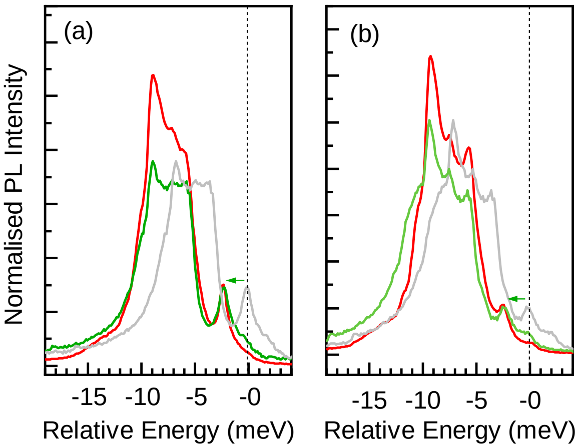

Figure 3.6: PL spectra obtained for two orthogonal polarisations and plotted relative to the energy of the FX_Y transition (dashed line). Grey line is a PL spectrum measured in the π_y polarisation, normalised to the intensity of the FX_X transition. Blue line is the same normalised PL spectrum shifted to the lower energy by the value of the energy splitting between FX_X and FX_Y, $\Delta E = 2.1\,\text{meV}$. Panel (a) shows the data obtained from the Spot 1, panel (b) shows the data from the Spot 2. Lower energy, intense PL band was not measured in the series from Spot 3.

Notably, no transitions corresponding to the main, intense PL emission, appear in the reflectance spectrum (Fig. 3.3). No additional features are observed at the same energy as the emission. Higher-energy features at the free-exciton transition plus the phonon energy are also not observed, although such phonon replicas have previously been reported in 2D perovskites [Urban 2020]. This strongly suggests that the dominant PL emission originates neither from a separate, additional species, nor from the localised trap states, as no blueshift of the emission is observed with increasing excitation power (Fig. 3.1 (C)). Rather it may stem from a reorganisation of the soft, ionic perovskite lattice. Such lattice deformation, called a phonon cloud, effectively “dresses” the free excitons, giving rise to exciton-polaron states that reflect specific lattice configurations.

Recent time-resolved photoluminescence studies of 2DP have shown that their low energy emission originates from the formation of large exciton polarons, rather than from static disorder or trap states [Hurtado Parra 2022]. Immediately after excitation, free excitons are created at the band edge. Within a few picoseconds, a substantial fraction of these excitons are strongly coupled to phonons, resulting in lattice dressing and the formation of exciton–polaron states. This process is manifested as a picosecond-scale redshift of the emission spectrum.

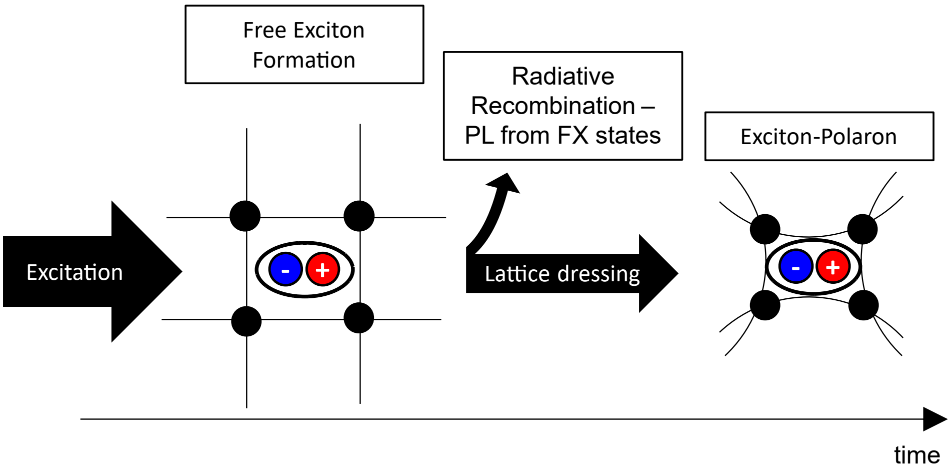

Figure 3.7: Schematic depiction of the processes occurring in the material after photoexcitation. Charge carriers form excitons, which then can either recombine in a radiative process and emit a photon of the energy of the FX transition, or remain bound as excitons and interact with the soft, ionic crystal lattice, leading to the formation of exciton-polarons.

Crucially, despite this redshift, the emission preserves the optical signatures of an excitonic transition: the photoluminescence intensity scales linearly with excitation power, the polarisation remains consistent with that of the free exciton observed in reflectance and on the high energy slope of the main emission, as shown in this work. Therefore, the experimental results support a scenario in which two radiative channels coexist (Fig. 3.7):

1. fast radiative recombination of free excitons occurring before lattice dressing;

2. delayed emission from exciton–polaron states, which dominate the steady-state spectrum.

This picture provides an explanation to the observed behaviour of the PL emission from the 2DP - redshifted, but preserving the excitonic nature and the polarisation of the either one of the FX *in plane* states of the exciton fine structure - FX_X or FX_Y.

Importantly, this interpretation rules out the need to introduce extra excitonic states to account for the PL spectrum and is consistent with exciton models based on symmetry considerations [Quarti 2024]. In light of these findings, the common attribution of the PL maximum to a free exciton transition should be reconsidered. Instead, the dominant PL emission at low temperature arises from excitons coupled to phonons – *i.e.*, exciton–polaron states – in addition to the free exciton transitions. The high crystalline quality of the studied samples, which minimises the spectral broadening, enables to separate these two contributions. Accurately identifying the true free exciton energy is essential for correctly extracting the fine structure splitting (FSS) values from PL spectra.

3.3 *Out of Plane*-Oriented Excitonic State

As previously described in subsection 1.3.5, the energy position of the remaining bright state – *out of plane*-oriented Z state – remained elusive thus far, with conflicting literature reports. Within this work, the topic was addressed experimentally, to prove the exact energy of the Z state and determine the bright excitonic triplet.

By choosing the appropriate sample orientation and performing polarisation-resolved measurements, it is possible to directly study each bright exciton state. To do this, the polarisation-resolved microreflectance experiments at $T = 4.2\,\mathrm{K}$ were carried out. The samples were mounted on custom-made copper plates in two ways. In the "plane" configuration, light was reflected from the crystal surface parallel to the inorganic layers (light oriented along the c axis of the crystal), giving selective access to the X and Y transitions. In the "edge" configuration, light was reflected from the edge of the crystal, allowing to probe the Z excitonic state, whose dipole moment is oriented perpendicular to the in-plane states. As shown in Fig. 2.4, the crystals were large and thick enough to have flat surfaces on both the planar part and its edge, much bigger than the 2-4 μm white-light spot. The polarisation optic elements were mounted in the excitation part of the experimental setup.

The results of these measurements are shown in Fig. 3.8. In Fig. 3.8, the black line show the reflectance spectra of unpolarised white light reflected from the crystal surface. Two sharp peaks at $\approx 2.353\,\mathrm{eV}$ and $\approx 2.355\,\mathrm{eV}$ correspond to the X and Y *in plane* exciton states, properties of which were described in detail in the previous section. However, to access the Z state, which has an *out of plane* oriented dipole moment, polarisation-resolved reflectance measurements were done in the "edge" configuration. When the white light is polarised along the c-axis of the crystal, the resulting spectrum (blue line) shows one strong resonance, attributed to the Z excitonic state.

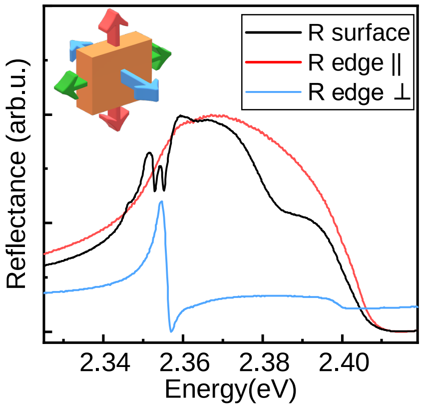

Figure 3.8: Reflectance spectra measured under two orthogonal polarisations in the "edge" configuration (red and blue lines) compared to the reflectance spectrum measured in the "plane" configuration (black line). The inset schematically depicts the orientation of the dipole moments of the bright excitonic states of the exciton fine structure with regards to the crystal.

Interestingly, the broad high-energy sidebands disappear when the light is polarised perpendicular to the crystal plane. This suggests strong optical anisotropy in 2D perovskites, since their *in plane* and *out of plane* properties are vastly different. A detailed analysis of the high energy sidebands is beyond the scope of this work, but this suggests that related to the *in plane* oriented excitons. When probing *in plane* states from the edge, the sidebands reappear, though the individual X and Y states cannot be resolved (red line). It is most likely because the crystal edge is of lower quality than the surface.

To confirm the *out of plane* character of the identified Z state, the reflectance as a function of the polarisation angle with respect to the *c*-axis was measured. Similarly to the studies of the *in plane* states, three series of reflectance measurements were carried out from three different spots on the edge of the crystal, to ensure the reproducibility of the findings.

The transition energy and oscillator strength are easier to see in the negative derivative of reflectance, -dR/dE (Fig. 3.9 (a-c)). This produces peaks at the transition energies, and the peak area is proportional to the oscillator strength of the transition (exemplary spectrum is shown in Fig. 3.9 (d)). The -dR/dE signal is the strongest when the polarisation is along the *c*-axis, and the Z-state signal disappears when polarised along the edge of the crystal. The same conclusion comes from the polarisation dependence of the transition intensity, shown in the polar plot in Fig. 3.9 (e). The double-lobe shape, aligned with the c-axis, confirms that the Z exciton is linearly polarised.

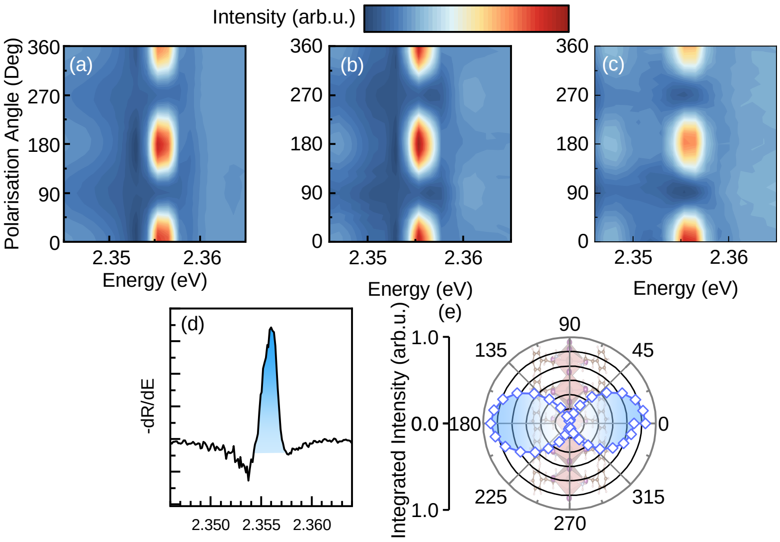

Figure 3.9: (a-c) Dependence of the negative derivative of the reflectance spectrum in the "edge" configuration versus polarisation angle, measured for three different spots at the edge of the sample. (d) Example of a negative derivative of the reflectance spectrum, measured for the "edge" configuration with polarization oriented perpendicular to the sample plane ("edge ⊥"). Shaded area under the plot is the integrated intensity of the transition. (e) Polar plot of the intensity of the Z state extracted from the negative derivative of the reflectance spectrum. $(PEA)_2PbI_4$ crystal structure is shown to provide a reference for the dipole moment orientation. This dataset is extracted from the measurement series displayed in panel (a).

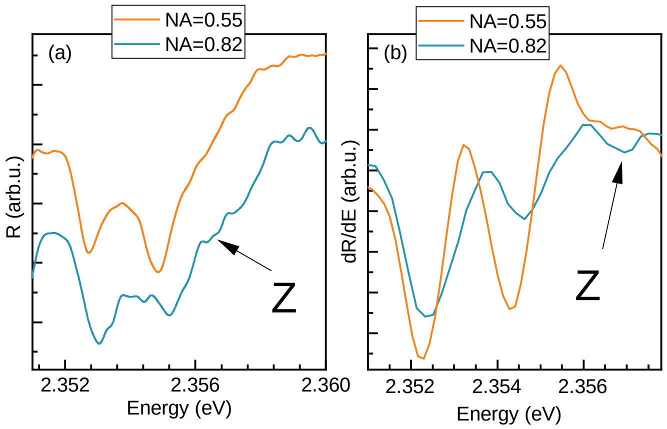

Figure 3.10: (a) Reflectance and (b) reflectance derivative spectrum measured in the "plane" configuration with the use of low (NA=0.55) and high (NA=0.82) numerical aperture objectives. The feature attributed to the Z exciton state transition visible with the use of high numerical aperture objective is indicated by the arrows.

To rule out any influence of crystal edge on the exciton transition energy, the reflectance spectrum from the crystal surface was also measured using a high numerical aperture objective (NA = 0.82). This setup gave access to the optical transitions with *out of plane* orientation, without the need to use any specific mounting plates. As shown in Fig. 3.10, an additional feature was observed, located 1.3-1.5 meV above the highest *in plane* state, which supports the conclusions obtained from the measurements in the "edge" configuration.

3.4 Evolution in the Magnetic Field

In previous sections, the energy of the three bright excitonic states was determined experimentally by optical spectroscopy measurements. However, the fourth, remaining state does not couple to the light because of the mismatch between its total angular momentum $J = 0$, and the total angular momentum of photons $J = \pm 1$, thus such a transition is momentum-forbidden and usually not accessible in optical measurements. In order to probe the dark excitonic state D and determine its energy, magneto-optical spectroscopy measurements were performed in the Faraday configuration (B ∥ k ∥ c, see Fig, 1.17 (a)). The details of the experimental setup for this part were described in subsection 2.3.3. The measurements were performed at the Faculty of Physics University of Warsaw, in the group of Prof. Adam Babiski and Prof. Maciej Molas.

In the Faraday geometry, the magnetic field "mixes" the dark exciton ψ_1 (D) with the *out of plane* ψ_2 (Z) state. The mixed states, including the "brightened" dark exciton, can be written as a linear combination of the zero-field states:

$$|\tilde{D}_B\rangle = c_2|D\rangle - c_1|Z\rangle, \qquad |\tilde{Z}_B\rangle = c_1|D\rangle + c_2|Z\rangle, \tag{3.1}$$

where the coefficients c_1 and c_2 depend on the magnetic field strength and the energy separation between the D and Z states (Eg. 1.32). Oscillator strength is transferred from the Z state to the dark state. Thanks to this mixing, the use of a high-NA objective (NA = 0.82), and the preferential population of the dark state at low temperatures, it was possible to observe the PL signature of the dark state D.

Fig. 3.11 (a) shows PL spectra at different magnetic fields. With increasing field, a sharp new feature appears on the low-energy side of the main PL band. It is assigned to the dark exciton, brightened by the magnetic field induced transfer of the oscillator strength. Its intensity grows quadratically with the field (Fig. 3.11 (b)), which is typical for a dark state becoming optically active through mixing with a bright state in the weak-field limit [Molas 2017, Zhang 2017]. The dark exciton lies about 15.5 ± 1.0 meV below the average energy of the *in plane* bright excitons, a value in a reasonable agreement with previous results on thin films in the Voigt configuration (21.6 ± 3.3 meV) [Dyksik 2020].

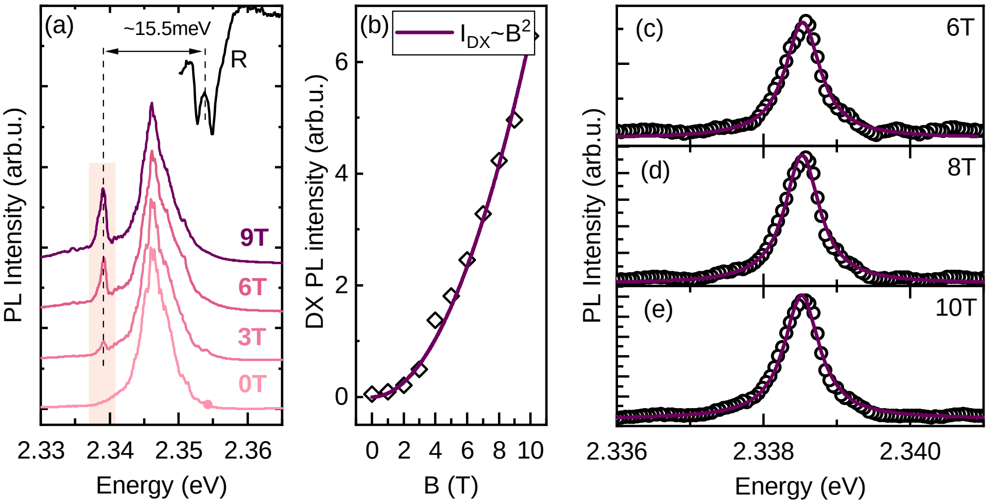

Figure 3.11: (a) PL spectra measured under the magnetic field. The light orange shading indicates the position of the brightened dark state. The arrow indicates the splitting between the *in plane* bright states and the dark state. (b) PL intensity of the dark exciton transition versus magnetic field. It shows quadratic dependence, as predicted for the weak field limit [Yu 2016, Zhang 2017]. (c-e) Examples of the fitting the dark exction PL peak with Lorentz function, shown for different values of the magnetic field. Because the dark state appears on the low energy side of the dominating PL peak, it was treated as a background and the straight line was subtracted from the spectra before the fitting to exclude its impact.

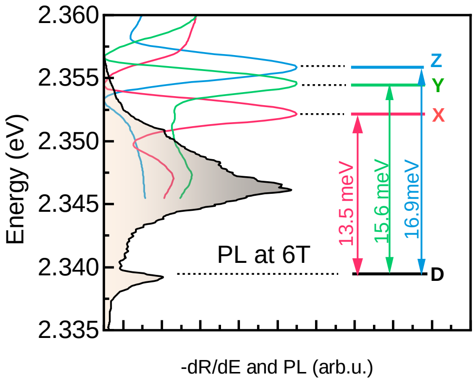

Figure 3.12: The photoluminescence spectrum measured in the magnetic field of 6 T (gray spectrum). The small peak visible below 2.34 eV is a signature of the dark exciton state. The coloured lines are the negative derivatives of the reflectance spectra (without the magnetic field) showing the energy positions of all of the bright exciton states.

Having previously identified all three bright exciton transitions, as well as the energy position of the dark state, it is possible to determine their order in $(\mathrm{PEA})_2\mathrm{PbI}_4$. Fig. 3.12 shows the negative derivative of the reflectance spectra (-dR/dE), measured with linearly polarised light aligned with each transition dipole. The X and Y states were measured in the “plane” configuration, while the Z state was measured in the “edge” configuration, as described in previous section of this chapter. The data show that the Z state lies above the two *in plane* states, about 3.4 meV above X and 1.3 meV above Y. All three bright states are located roughly 15 meV above the dark state, revealed in magneto-PL studies. These results confirm the bright state ordering predicted by recent first-principle calculations and some effective mass models for lead-iodide 2D perovskites and nanocrystals [Ben Aich 2020, Biffi 2023, Quarti 2024].

External magnetic field not only enables direct observation of the dark excitonic state in the optical experiment, but also provides insight on more fundamental properties of excitons. This information can be obtained by analysis of the evolution of excitonic states as a function of the magnetic field. As previously described in the subsection 1.3.6, in the Faraday geometry, the magnetic field-induced shifts of the two coupled pairs of states X-Y and D-Z, is given by (Eq. 1.41):

$$\tilde{E}_{Y(D)/X(Z)}(B) = \frac{1}{2}\left[(E_{Y(Z)} + E_{X(D)}) \pm \sqrt{(E_{Y(Z)} - E_{X(D)})^2 + g^2_{B(D)}\mu^2_{\mathrm{B}}B^2}\right] + c_0 B^2 \tag{3.2}$$

where:

$E_{Y(D)/X(Z)}$ – energy Eigenvalues of the zero field states,
B – magnetic field,
μ_B – Bohr magneton,
$g_{B(D)}$ – g-factor of bright (dark) exciton, respectively,
c_0 – diamagnetic coefficient.

The energy shifts of the two *in plane* bright states were extracted from magneto-reflectance spectra (Fig. 3.13 (a)). As described in subsection 1.3.6, these two excitonic states, non-degenerate in energy and linearly polarised, change their properties when the external magnetic field is applied [Kataoka 1993, Yu 2016]. The exchange interaction warranted mixing between the $|\psi_3\rangle$ and $|\psi_4\rangle$ basis states is suppressed, and the states gain back the circular polarisation, which can be seen in Fig. 3.13 (b). The excitonic features, when measured in the circular polarisation basis, are visible simultaneously at zero field. However, when the magnetic field is applied, they not only shift in field according to the dependence of Eq. 3.2, but also become visible only one each in a specific circular polarisation, confirming the suppression of the exchange-interaction warranted basis state mixing when the external magnetic field is applied.

Analysing the spectra in a broader energy range reveals two additional features in the reflectance spectra, located approximately 14 meV above the free excitonic transition (as indicated in Fig. 3.13. They are also separated by 2 meV and display the exact same behaviour in the magnetic field – *i.e.*, with increasing magnetic field, only one of two features can be seen in each polarisation, whereas at zero field both were visible. They also display Zeeman energy shift, in the exact same way as the FX. All of this is suggesting that these additional features in fact originate from the excitonic transitions, and the same energy evolution in the magnetic field as the FX leads to the conclusion that they are phonon replicas [Urban 2020].

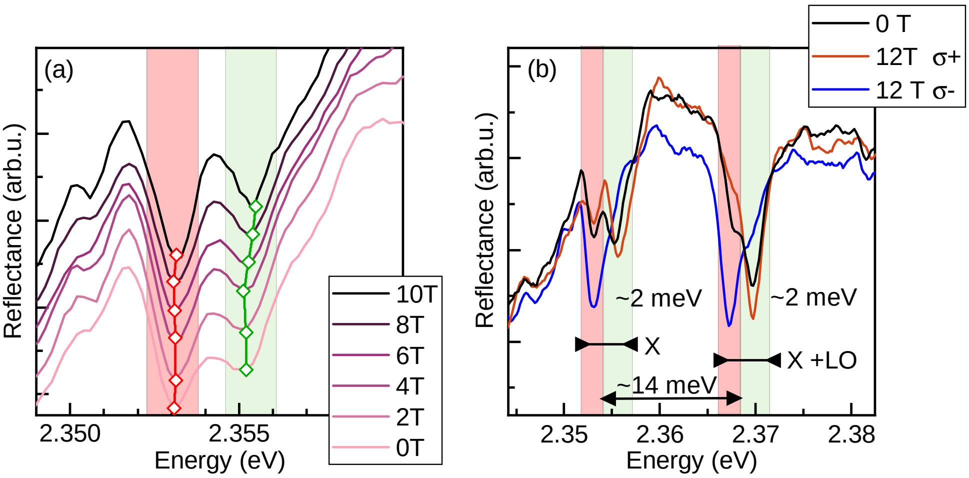

Figure 3.13: Reflectance spectra in the magnetic field. Light red and green shaded areas indicate X and Y states. (a) Reflectance spectra for different magnetic fields together with indicated shifts of two excitonic transitions. (b) Reflectance spectra obtained for zero-field (black) and magnetic field (orange and blue) measurements performed for two orthogonal circular polarisations. A phonon replica at approx. 2.37 eV is also indicated.

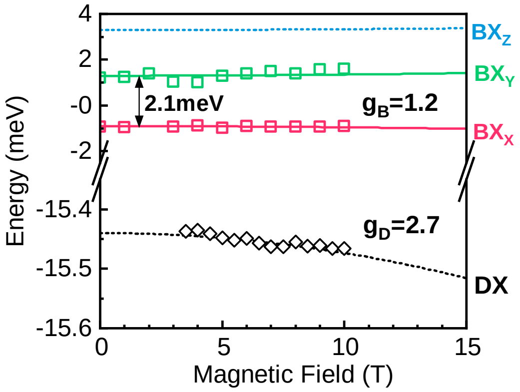

Figure 3.14: Dependence of the energy of the excitonic state versus the magnetic field applied in the Faraday configuration. Lines are calculated according to the Eq. 3.2.

The energy shifts in magnetic field of two bright in-plane states and the dark state are summarised in Fig. 3.14. Energies of the the bright X and Y states are taken from the reflectance measurements, and for the dark excitonic states they are obtained from the fitting of the PL spectra with the Lorentz function, (Fitting examples are shown in Fig. 3.11 (c)). The observed shifts of the in-plane bright states are well described using an X-Y splitting of 2.1 meV and bright exciton g-factor value $\mathrm{g}_B = 1.2 \pm 0.1$, in agreement with earlier high-field studies [Dyksik 2020, Dyksik 2021a]. The dark state peak shows a slight red-shift with magnetic field, as expected for the lowest dark exciton[Kataoka 1993], confirming the states' assignment. Taking the D-Z splitting of 16.9 meV, the obtained value of dark exciton g-factor $\mathrm{g}_D = 2.7 \pm 0.2$.

Determination of the exact energies of all exciton fine structure states, thus the energy differences between them, allowed the determination of the independent electron and hole g-factors paralell to the *c*-axis of the crystal. As in the case of the Faraday configuration, $g_{B(D)}$ is the bright (dark) exciton *g*-factor along the c axis of the crystal, being sum (difference) of electron and hole g-factors, also along the c axis of the crystal:

$$g_{B(D)} = g_{e\|} \pm g_{h\|} \tag{3.3}$$

Based on $\mathrm{g}_D = 2.7$ and $\mathrm{g}_B = 1.2$, the values of independent electron and hole g-factor parallel to c-axis are estimated to be to be $\mathrm{g}_{e\|} = 1.95 \pm 0.3$ and $\mathrm{g}_{h\|} =$ -0.75 ± 0.3. The determined electron $\mathrm{g}_e \| = 1.95$ is in very good agreement with that obtained from recent Kerr rotation measurements ($\mathrm{g}_{e\|} = 2.05 \pm 0.05$, after [Kirstein 2022b]).

In conclusion, a complete description of the bright exciton fine structure was presented for 2D perovskite representative $(\mathrm{PEA})_2\mathrm{PbI}_4$. Using polarisation-resolved reflectance from the edge of the 2D crystals, the Z state, whose dipole moment is oriented out of the 2D crystal plane, became accessible. It is confirmed to be of highest energy among all bright states of exciton fine structure. These results disagree with general effective mass theory predictions [Tanaka 2005, Ema 2006] but agree with recent ab-initio calculations [Ben Aich 2020, Quarti 2024]. By identifying the Z-state position, it was also possible, for the first time, to report g-factors for the Z and dark excitons (along the *c*-axis of the crystal). This result allowed determination of the separate electron and hole g-factors, providing a reliable benchmark for band structure models. The values of parameters obtained in this chapter are summarised in Table 3.1.

Parameter	**Value**	**Parameter**	**Value**	**Parameter**	**Value**
E_D	2.339 eV	ΔE	2.1 ± 0.1 meV	g_B	1.2
E_X	2.353 eV	J_x	5.2 meV	g_D	2.7
E_Y	2.355 eV	J_y	3.95 meV	$\mathrm{g}_{e\|}$	1.95 ± 0.3
E_Z	2.357 eV	J_z	2.6 meV	$\mathrm{g}_{h\|}$	-0.75 ± 0.3

Table 3.1: Summary of the parameter values obtained in this chapter.

3.5 Results Obtained for the Alternative Batch of Samples

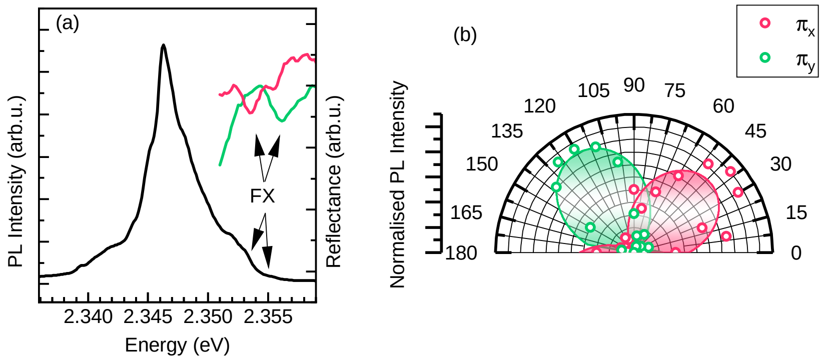

Figure 3.15: Optical spectra measured from $(PEA)_2PbI_4$ single crystal grown by a slow evaporation of a solvent method. (a) PL spectra measured without polarisation optics (black line) and reflectance spectra (pink and green lines) measured for two orthogonal linear polarisations. (b) PL intensity of FX_X and FX_Y transitions as a function of polarisation detection angle.

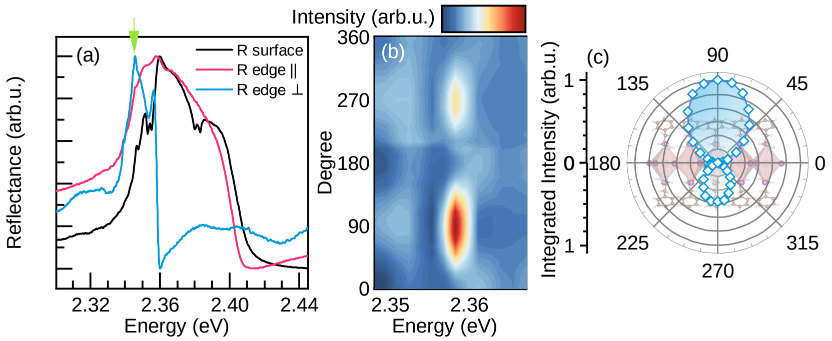

Figure 3.16: (a) Reflectance spectra measured under two orthogonal polarisations in the "edge" configuration (red and blue lines) compared to the reflectance spectrum measured in the "plane" configuration (black line). Green arrow indicates the feature attributed to the photoluminescence visible in the reflectance spectra, however it is clearly separated from the features of interest and does not obscure the results. (b) Dependence of the negative derivative of the reflectance spectrum as a function of the polarisation angle. (c) Integrated intensity of the negative deriviative of the Z state feature in the reflectance spectrum showing linear polarisation. Schematic of the (PEA)2PbI4 crystal structure shown for the reference of the dipole moment orientation. This crystal was installed in the setup perpendicular to the crystal grown via other method, hence the difference in the angular orientation.

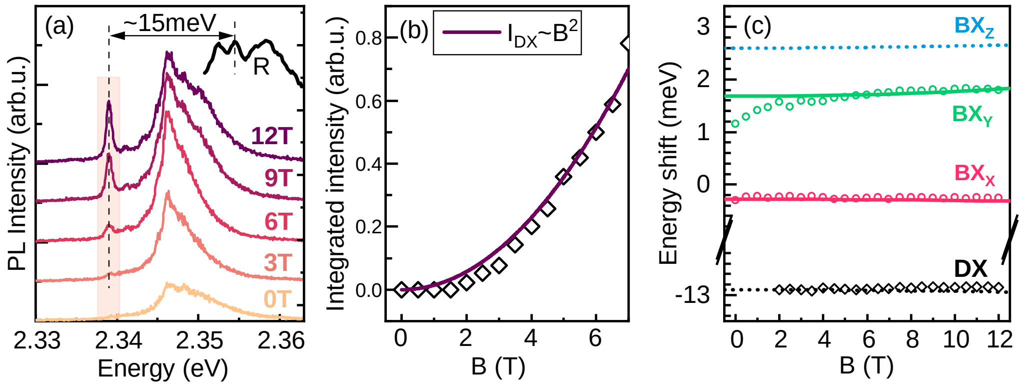

Figure 3.17: PL spectra from PEPI n=1 single crystal grown by slow evaporation of a solvent, measured under the external magnetic field. (a) PL spectra measured under the magnetic field. The light orange shading indicate the position of the dark state brightened by the magnetic field. Arrow indicate the distance between in-plane bright states and dark exciton states. (b) Dark exciton transition PL intensity as a function of the magnetic field showing quadratic dependence. (c) Dependence of the energy of the excitonic states versus the magnetic field. Lines are calculated according to the Eq. 3.2, for g_B=1.2 and g_D=2.7, the same values as in Fig. 3.14.

In order to exclude any influence of the possible material defects on the obtained results, in this study two sets of samples were investigated, grown by two different synthesis methods. This section shows the results obtained from the samples grown by the slow evaporation of a solvent. Samples for the experiments were kindly shared by Prof. Mirosław Mączka from Polish Academy of Sciences.

As shown in Figures 3.15, 3.16 and 3.17, the results of optical and magneto-optical investigations are the same, regardless of the synthesis method used to produce 2D perovskite crystals. This fact further confirms the reproducibility of obtained results and the validity of the analysis described in this chapter.

CHAPTER 4

Evolution of Properties from Two-Dimensional to Bulk Limit

Despite the relatively easy tunability of the excitonic properties of 2D perovskites by adjusting the number of layers within a crystal structure, the effect of quantum confinement on the exciton fine structure has not yet been studied in detail. This is important to understand why these materials show such high emission efficiency [Tamarat 2019, Dyksik 2021a]. Fine structure splitting has been reported for bulk, 3D perovskites [Baranowski 2019a], as well as the 2D limit, in case of a 2DP compound with n=1 [Do 2020, Posmyk 2024a]. The aim of this chapter is to show how the excitonic properties evolve between the 2D ($n = 1$) and 3D ($n \rightarrow \infty$) limits. This evolution is not straightforward, since increasing the number of inorganic layers n affects not only confinement, but also dielectric screening and carrier masses [Blancon 2018, Dyksik 2020]. Thus, solid experimental data are needed to build accurate theoretical models across the 2D-3D transition, filling the gap between these two limits.

In this chapter, the main focus is placed on the bright *in plane* exciton fine structure in the series of representative 2D perovskite compounds $(PEA)_2(MA)_{n-1}Pb_nI_{3n+1}$ (PEPI). Using polarisation-resolved and magneto-optical spectroscopy techniques, the evolution of splitting of in-plane bright excitons is studied for the series of PEPI compounds with varying number of the inorganic octahedra layers ($n = 1..4$). The splitting between the states decreases with an increasing n and reaches bulk-like values already for $n = 4$. The bright exciton g-factors increase, approaching the bulk values as n increases. These results provide important benchmarks for exciton theory, as these properties reflect the anisotropy and dispersion of the electronic bands.

4.1 Optical Response from Series of PEPI Compounds

The high-quality $(PEA)_2(MA)_{n-1}Pb_nI_{3n+1}$ ($n = 1..4$) single phase-pure crystals used in this study were grown by a cooling-induced crystallization method and were kindly shared by Prof. William Tisdale from Massachusetts Institute of Technology. Their average size was a few millimeters (as shown in Fig. 2.4 (a)).

Optical measurements, including micro-photoluminescence and micro-reflectance, were carried out in backscattering geometry at T = 4.2 K, as shown in Fig. 2.7. As in the study for the PEPI compound with n=1, described in chapter 3, an objective with numerical aperture (NA) of 0.55 was used to selectively access the *in plane* states. The polarisation optics was placed in the detection part of the experimental setup.

Typical PL and reflectance spectra for $n = 1..4$ are shown in Fig. 4.1. With increasing n, both the PL spectra and the exciton resonances (highlighted by shaded areas in the reflectance spectra) shift to lower energies. This shift reflects the weakening of quantum and dielectric confinement as the quantum well becomes thicker [Blancon 2018, Dyksik 2021b].

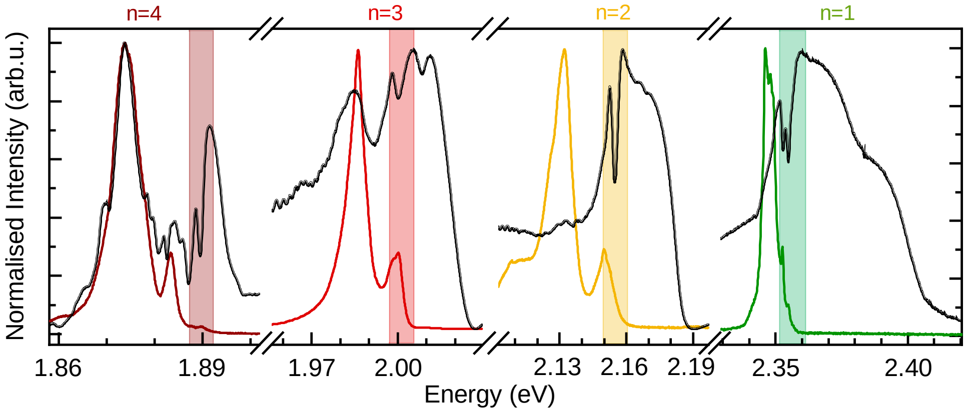

Figure 4.1: Photoluminescence (PL) (coloured lines) and reflectance (black double lines) spectra for samples with varying numbers of inorganic octahedra layers n. Shaded areas indicate the excitonic transitions. Colours denote the respective PL emissions in the visible range. The multiple resonance structures visible in the reflectance spectra for $n = 3$ and $n = 4$ are attributed to the phonon replicas of the main excitonic transition. Adapted from [Posmyk 2024b].

For all investigated samples, the PL spectra have a complex shape with two main features. The more intense PL peak is redshifted compared to the excitonic resonances in reflectance, while the weaker PL peak overlaps with them (Fig. 4.1). By comparing the high-energy PL peaks with the excitonic transitions in reflectance, the are assigned to free exciton recombination, as it was shown in the previous chapter for the PEPI compound with n=1, where the effect was the most prominent. The stronger, redshifted PL peak likely comes from local potential variations, such as polaronic effects [Tao 2021, Kahmann 2021], shallow traps [Jin 2020] or local band gap fluctuations [Zuri 2023, Dar 2016]. Because relaxation processes are faster than free exciton radiative recombination, the PL of each sample is dominated by this low-energy component.

The exact origin of the complex PL spectrum is beyond the scope of this work. The assignment of PL peaks to free exciton transitions is therefore based mainly on their energy, which matches the excitonic transitions observed in reflectance spectra. PL can be viewed as a convolution of the density of states with the thermal distribution of carriers. This is why PL spectra are more complex and often dominated by trapping-related signals rather than free exciton recombination.

In the remaining part of this chapter, all of the discussion revolves around and the conclusions are drawn from the results of the reflectance measurements, which directly reveal the energies of free exciton transitions.

4.2 Polarisation-Resolved Measurements

Fig. 4.2 (a) shows two reflectance spectra of the n = 2 sample, measured with orthogonal linear polarizations π_x and π_y. The energy difference between the π_x and π_y spectra (red and green curves) is the signature of the bright exciton fine structure splitting (FSS), which cannot be seen in unpolarised spectra due to the transition broadening. Panels (b) and (c) show the corresponding reflectance spectra measured in analogous way on samples with n=3 and n=4, respectively. There is a clear trend visible – the reduction of the energy splitting as the number of octahedra layers increases.

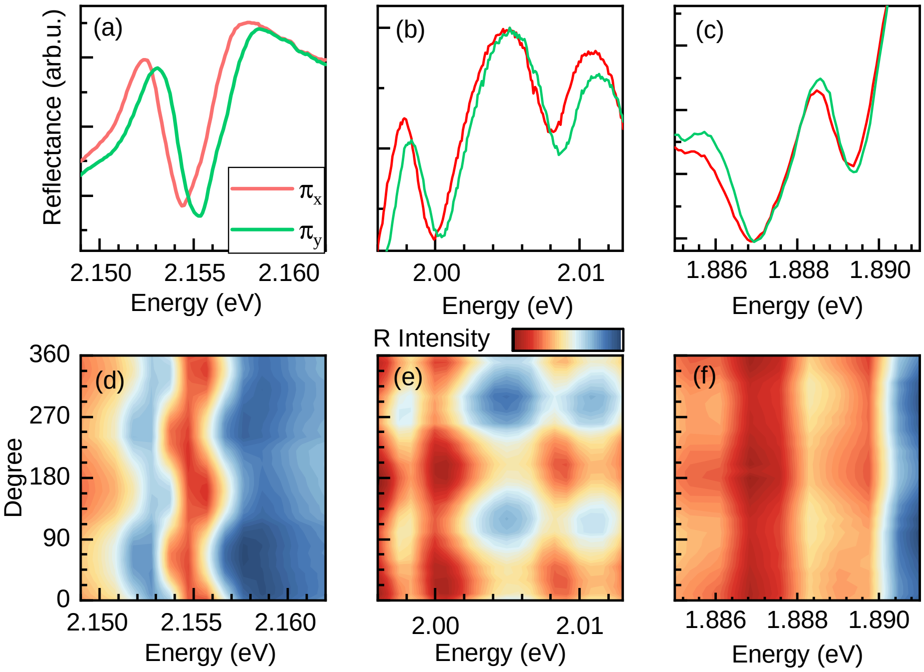

Figure 4.2: Reflectance spectrum measured in two orthogonal linear polarisations from the sample with (a) n = 2, (b) n=3 and (c) n=4, showing the energy splitting between two bright states of the exciton fine structure. As the n increases, the value of the spliting becomes more and more reduced. (d-f) Dependence of the reflectance spectrum for PEPI (d) n = 2, (e) n=3 and (f) n=4 versus polarisation angle. The clear oscillating pattern is visible for the PEPI compound with n=2, however the value of the energy splitting becomes too small to easily detect the difference for thicker PEPI compounds.

To study this in more detail, the reflectance was measured as a function of polarisation angle (Fig. 4.2 (d-f)). The spectra show a clear oscillating pattern with a 180° period, caused by the changing contribution of the two orthogonally polarised exciton states with slightly different energies. To determine the exact value of the FSS, the shift of the resonance energy with the analyser angle was studied.

To detect this small shift (single meV or less), an analysis was performed using a method described in detail in the literature [Baranowski 2019a, Baranowski 2019b]. It is based on the fact that the reflectance line shape remains nearly unchanged for different polarisation analyser orientations, as shown in Fig. 4.2 (a) for PEPI n=2, (b) for n=3 and (c) for n=4. In panels (a-c) of the Fig. 4.3, the "ratio spectra" (open symbols) are shown, obtained by dividing reflectance spectra measured at different analyser orientations by a reference spectrum taken at a specific orientation. It is chosen to fully maximise one of the *in plane* states, and reveal the maximum value of the energy splitting between the two states. Because the exciton resonance shifts slightly in energy with analyser angle, these ratio spectra show sharp features whose amplitude, width, and position depend strongly on the energy shift relative to the reference spectrum.

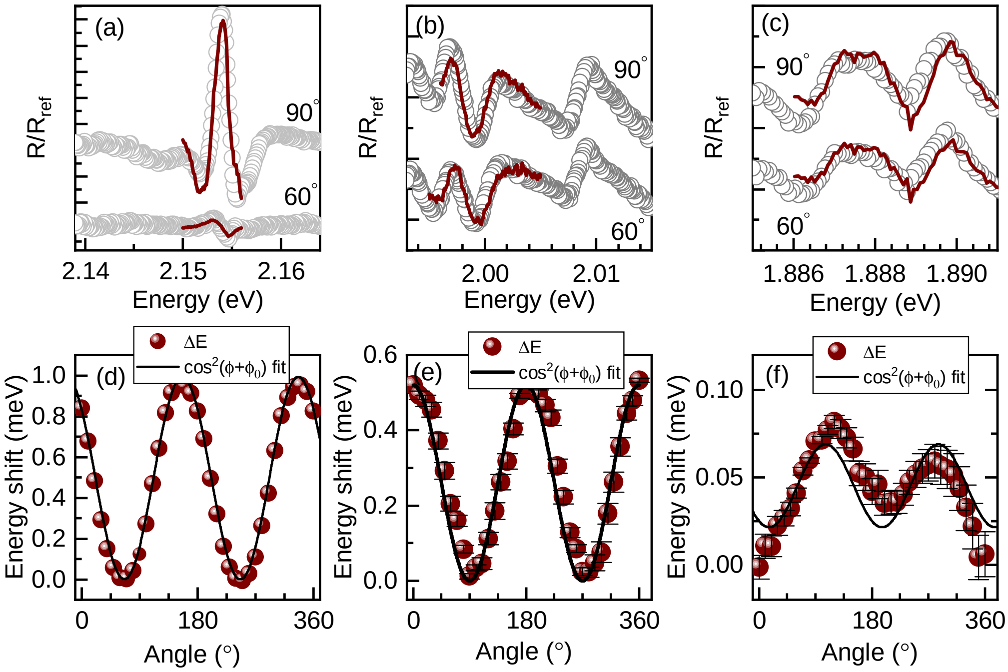

Figure 4.3: Fitting examples of the ratio spectra for PEPI samples (a) n=2, (b) n=3 and (c) n=4. (d-e) Extracted energy difference between two features in reflectance for the compounds with n=2, n=3 and n=4, respectively. The black line is a $\cos^2(\phi + \phi_0)$ fit to the data points.

The ratio spectra are fitted with a formula [Baranowski 2019a]:

$$\frac{R_\alpha(E)}{R_0(E)} = \frac{AR_0(E+\Delta E)+B}{R_0(E)}, \tag{4.1}$$

where:

$R_0(E)$ – reference spectrum,
$R_\alpha(E)$ – spectrum at an analyser angle α,
A – constant accounting for possible changes in the amplitude,
B – constant accounting for possible changes in the background,
ΔE – resonance shift at angle α.

The fits were performed using the least squares method and show good agreement with the experimental data.

This approach allows to precisely extract the small energy shifts of the exciton transition. The extracted shifts as a function of polarisation angle are shown in Fig. 4.3 (d-f). In all cases, the data follow a dependence:

$$\Delta E(\alpha) = \delta \cos^2(\alpha+\phi), \tag{4.2}$$

which directly provides the splitting δ between the two *in plane* bright exciton states.

The values of the bright exciton fine structure splitting (FSS) δ as a function of quantum well thickness are shown in Fig. 4.4. The splitting between the *in plane* exciton states decreases systematically from about 2 meV to about 0.2–0.1 meV as n increases.

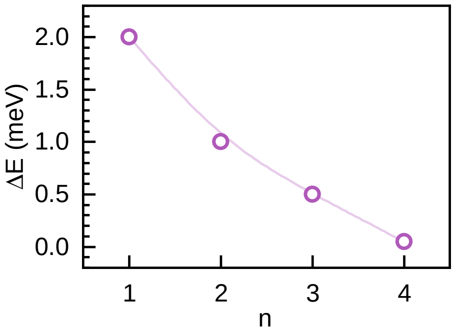

Figure 4.4: Energy splitting as a function of the number of inorganic octahedron layers n, extracted from polarization-resolved measurements.

This trend can be explained qualitatively: in wider quantum wells (higher n) the exciton binding energy decreases, and the exciton wave function becomes more extended [Dyksik 2021b]. As the distance between electron and hole increases, the exchange interaction becomes weaker, leading to smaller FSS [Fu 1999, Ramade 2018, Nestoklon 2018, Guilloux 2023]. Quantitatively, these values provide useful benchmarks for exciton models in metal-halide perovskites. For example, for n = 4 obtained value of the energy splitting of approx. 0.1 meV is close to the expected bulk value (100–200 μeV [Yin 2017, Nestoklon 2018, Baranowski 2019a]).

4.3 *In plane*-Oriented Excitonic States in the Magnetic Field

To better understand the properties and evolution of the excitonic states, the magneto-reflectance measurements in the Faraday configuration (B ∥ k ∥ c) were performed, using static magnetic fields up to 12 T at T=10 K. As shown in Fig. 4.5 (a), the magnetic field increases the splitting between the *in plane* exciton states. Tracking how the transition energies change with field allows to extract not only the value of the energy splittion δ but also the exciton g-factor and the diamagnetic shift.

In this configuration, the two *in plane* bright exciton states mix with each other; at zero field they are linearly polarised, while at high fields they become circularly polarised. This behaviour is clearly seen in Fig. 4.5 (a) for PEPI n=2, where the spectra are shown in the circular polarisation basis. At zero field both states appear in the spectrum, but as the field increases, each state gains circular polarization and becomes stronger in one chosen circular polarisation, as shown in Fig. 4.5 (b) and (c) for n=3 and (d) and (e) for n=4.

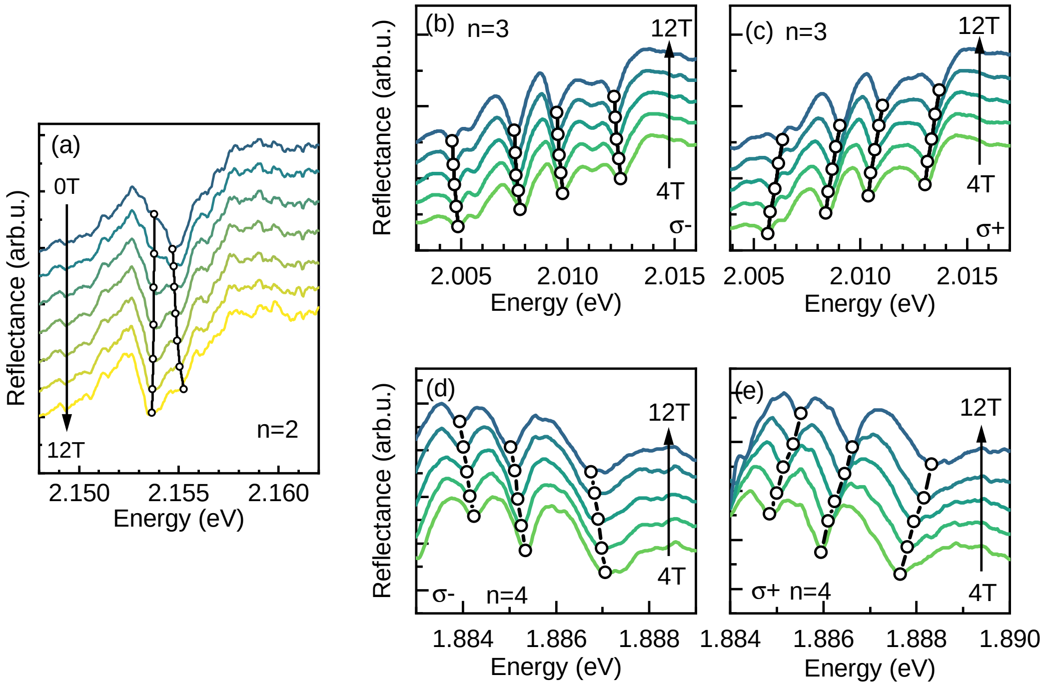

Figure 4.5: Reflectance spectra for the (a) n=2, (b-c) n=3 and (d-e) n=4 samples at different magnetic fields. Panels (b) and (d) show one circular polarisation σ^-, and panels (c) and (e) show the other one σ^+. Black lines track the shift of the excitonic transition as a function of the magnetic field. There are multiple transitions present in the spectra, likely related to the presence of phonon replicas, as they shift the same way in the magnetic field.

It is worth to note that the reflectance spectra are more complex for samples with n = 3 and n = 4. Multiple resonance-like features are present in the spectra, with the energy separation too large to consider them as originating from multiple fine structure states. However, all features shift in the same way under a magnetic field, as shown in Fig 4.5 (b-e). This strongly suggests that these features are phonon replicas of the same excitonic transition (the zero-phonon line, denoted in Fig.4.5 as stars) [Urban 2020]. Importantly, for the analysis performed here, the exact origin of these features is not critical, as long as they all shift identically with magnetic field or with polarisation angle – which they do. Had they originated from different excitonic species, their shifts would differ, but this is not observed.

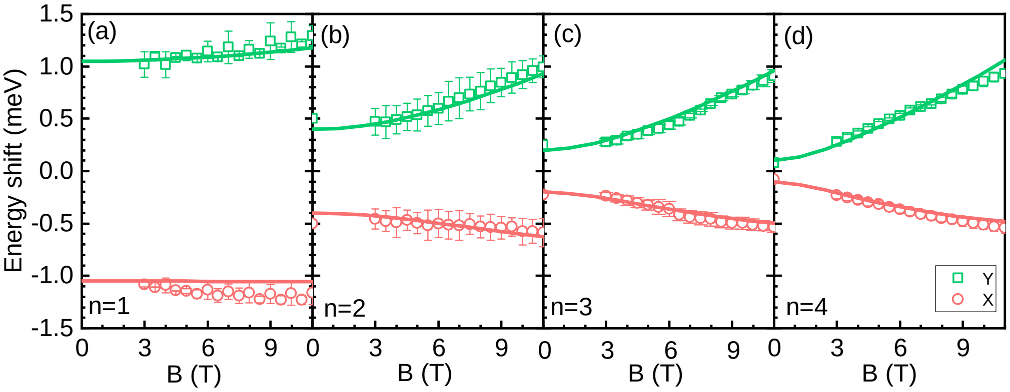

Figure 4.6: Energy of the bright excitonic in-plane states with respect to the magnetic field for (a) n=1, (b) n = 2, (c) n = 3, and (d) n = 4 PEPI compounds. Data extracted from the magneto-reflectance measurements.

The evolution of exciton energy shifts in magnetic field for samples with n = 1..4 is shown in Fig. 4.6. In the analysis, spectra below 3 T were excluded because the exciton states for n = 3 and 4 are not spectrally resolved well enough at low fields. The transition energy shift relative to the average energy of in-plane excitonic transition ($\frac{1}{2}(E_Y + E_X)$) at zero field is described by the formula:

$$\Delta E_{Y/X}(B) = \pm\frac{1}{2}\sqrt{\delta^2 + g_B^2\mu_{\mathrm{B}}^2 B^2} + c_0 B^2, \tag{4.3}$$

where:

δ – energy splitting between the two *in plane* exciton states,
g_B – bright exciton g-factor,
μ_{B} – Bohr magneton,
c_0 – diamagnetic coefficient.

By fitting the data with the equation 4.3, the values of δ, c_0 and g_B as functions of n can be obtained. The dependence of the energy splitting between the *in plane* excitonic states on n from this method is presented in Fig. 4.7, compared to the value of the splitting obtained from the linear polarisation-resolved measurements at zero field. Importantly, the values obtained from magnetic-field dependence agree very well with those extracted from measurements at zero field, which confirms the reliability of the performed analysis.

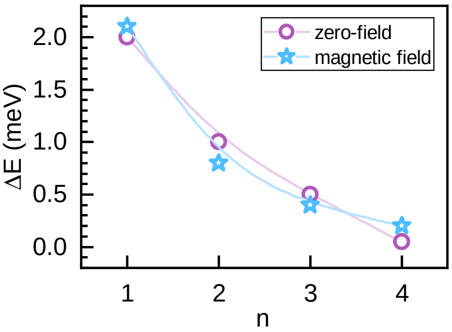

Figure 4.7: Energy splitting as a function of the number of inorganic octahedron layers n, extracted from polarization-resolved measurements without the magnetic field (circles) and from magneto-optical measurements (stars).

Diamagnetic shift The diamagnetic shift increases the energy of the excitonic transition, as it is a manifestation of "squeezing" the excitonic wavefunction by the magnetic field, increasing the interaction between charge carierrs. Its effect is clearly visible in the data. The upper transition shows a blue shift, while the lower one exhibits a red shift. These shifts are not symmetric, which originates from the quadratic term in the Eq. 4.3. The extracted diamagnetic coefficients c_0 increase with n, as the exciton wave function becomes more extended *in plane* in thicker quantum wells (as shown in Fig. 4.8 (a)) [Dyksik 2021b]. Since $c_0 = \frac{e^2}{8m_r^*}\langle r^2 \rangle$, where $\langle r^2 \rangle$ is the mean-square exciton radius [Miura 2007], this trend is expected. The values of c_0 are shown in Fig. 4.8 (b) together with previously reported values, which are in a good agreement [Dyksik 2021b, Urban 2020].

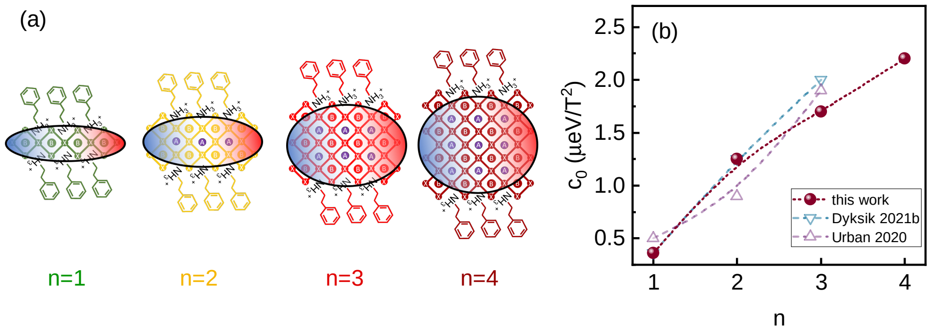

Figure 4.8: (a) Schematic depiction of the excitonic wavefunction spanning over 2DP crystal. (b) Diamagnetic coefficient as a function of the number of inorganic octahedron layers n. Values obtained in references [Dyksik 2021b] and [Urban 2020] are displayed for comparison.

4.3.1 g-factors

The analysis performed on the evolution of the excitonic states' energy also provide the dependence of the bright exciton g-factor on n. As the data were obtained from experiments in the Faraday geometry, the g-factors accessed here are in the direction parallel to the crystal *c*-axis. As previously defined in Eq. 1.28, the "bright" exciton g-factor refers to the sum of the g-factors of the electrons and holes in the relevant direction:

$$g_B = g_{e\|} + g_{h\|} \tag{4.4}$$

The results of the fitting the excitonic states' energy shift with the Eq. 4.3 are shown in Fig. 4.9 (a) as a function of the number of octahedra layers n. The value increases, however it reaches a kind of a plateau for higher values of n. To put these values into a context, it is better to display them not as a function of n, but rather as a function of the energy band gap of a material, as shown in Fig. 4.9 (b) (pink circles). Additionally the values reported for 3D perovskites (black squares) and 2D perovskites (n = 1, purple circles) [Kirstein 2022a, Dyksik 2021a] are shown, together with the curves showing the theoretical prediction of the g-factor dependence on the band gap energy for MHP [Kirstein 2022a].

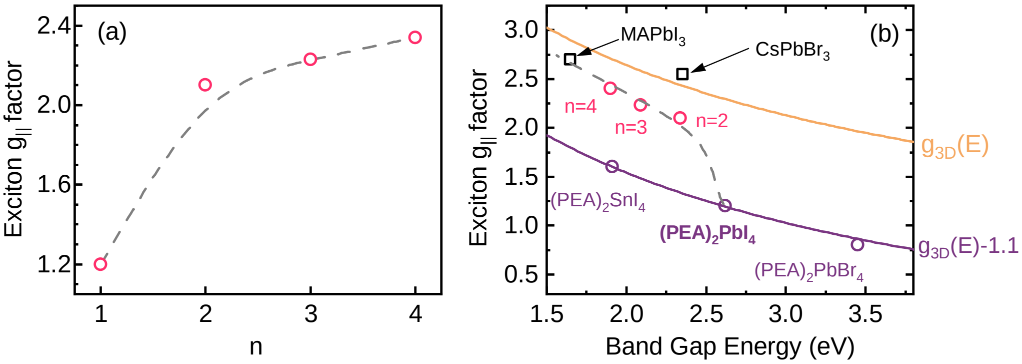

Figure 4.9: Exciton g-factor in the direction parallel to the c axis of the crystal as a function of (a) the number of octahedra layers n, and (b) the band gap energy. Values of the bulk perovskite g_{3D}(E) are taken after reference [Kirstein 2022a]) and values of g-factors for 2D perovskites are taken after reference [Dyksik 2021a] The gray dashed line is a guide to the eye showing the evolution of g-factors from the 2D limit to the 3D limit. Adapted from [Posmyk 2024b].

The work of Kirstein *et al.* invoked the k·p model to predict the dependence of the g-factors of the electrons end holes in MHP on the band gap energy of a material. This dependence is defined as:

$$\begin{aligned} g_e &= -\frac{2}{3} + \frac{4}{3}\frac{p^2}{m_0 E_g} + \Delta g_e \\ g_h &= 2 - \frac{4}{3}\frac{p^2}{m_0}\left(\frac{1}{E_g} - \frac{1}{E_g + \Delta}\right) \end{aligned} \tag{4.5}$$

The experimental data provides the values of the excitonic g-factor, being the sum of g-factors for electrons and holes. Then, the dependence takes the following form:

$$g_{3D}(E) = g_e + g_h = \frac{4}{3} + \Delta g_e + \frac{4}{3}\frac{p^2}{m_0(E_g + \Delta)}, \tag{4.6}$$

where:

g_e – electron g-factor,
g_h – hole g-factor,
p – interband momentum matrix element,
m_0 – free electron mass,
E_g – fundamental band gap,
Δ – spin–orbit splitting energy of the valence band,
Δg_e – correction to the electron g-factor due to remote bands.

It is shown in Fig. 4.9 (b) as an orange curve, in reasonable agreement with the experimental data obtained for 3D MHP (black squares, after [Kirstein 2022a]). The g-factor decreases when the band gap increases. The observed trend agrees with general predictions of the k·p model for MHP [Kirstein 2022a, Nestoklon 2023].

Furthermore, the same curve shifted downward by a value of 1.1 (purple line), matches very well the experimentally obtained g-factors of PEA-based 2D perovskites (purple circles, after [Dyksik 2021b]) This suggests that in case of 2DP, the model can be applied with mostly the same parameters as in 3D case, but with adjusted correction Δ. For n = 2, 3, and 4, the g-factor values lie between the pure 2D and 3D limits and gradually approach the 3D value ($MAPbI_3$). It already approaches the bulk values for 2DP with n=4. This shows that confinement plays a key role in determining the g-factor, and show the gradual evolution of the excitonic properties between the 2D and 3D limit.

The bright in-plane exciton fine structure splitting (FSS) and its g-factors were studied in $PEA_2(MA)_{n-1}Pb_nI_{3n+1}$ crystals with n ranging from 1 to 4. It was shown that, similar to the pure 2D and 3D limits, the in-plane exciton states exhibit splitting and orthogonally oriented dipoles under the intermediate confinement regime. For the first time, the evolution of the exciton g-factors as a function of n was described for $PEA_2(MA)_{n-1}Pb_nI_{3n+1}$ compound series. The observed FSS, together with the exciton g-factors, was found to approach the values characteristic of bulk metal-halide perovskites as n increased. This evolution can be explained by the gradual reduction of quantum confinement. The parameters provided here form a reliable basis for further studies of the band structure and excitons in lead-halide perovskites, particularly the role of quantum and dielectric confinement.

Chapter 5

Conclusions

In this thesis, the optoelectronic properties of two-dimensional metal-halide perovskites were studied experimentally, using optical spectroscopy methods. This material system is an object of extensive investigations due to their application potential, but it is also a convenient framework for fundamental research – such as exciton physics. The main goal of this work was to determine the exciton fine structure. Detailed experimental studies were performed on a series of compounds of a representative 2D perovskite – phenylethylammonium lead iodide, $(\mathrm{PEA})_2(\mathrm{MA})_{n-1}\mathrm{Pb}_n\mathrm{I}_{3n+1}$ – with varying number of octahedra layers n. Obtaining precise values of the excitonic states' energy was possible due to the excellent crystalline quality of the investigated single crystals of 2D perovskites.

In Chapter 3, the fine structure was revealed in its entirety for the 2DP compound with utmost 2D-like character – $(\mathrm{PEA})_2\mathrm{PbI}_4$ $n = 1$, with a single layer of octahedra units within the crystal structure. The ordering, energy separation, and nature of the excitonic states were established using polarisation-resolved optical spectroscopy with and without the use of external magnetic fields, resolving long-standing ambiguities reported in the literature. Importantly, the Z state, with its dipole moment oriented perpendicular to the crystal plane, was confirmed to be the highest in energy among the bright states. This finding contradicts some reports based on the effective mass theory, but agrees well with recent ab-initio predictions. The energy position of the dark state was confirmed to be energetically lowest, in agreement with previous literature reports. For the first time, the g-factors of the Z and dark excitons were determined, allowing the extraction of separate electron and hole g-factors (in the direction parallel to the crystal c axis), providing a robust benchmark for band structure models.

In Chapter 4, the series of 2DP compounds with varying number of octahedra layers n were studied using the optical spectroscopy methods. Polarisation-resolved measurements with and without the use of the magnetic field were performed on $(\mathrm{PEA})_2(\mathrm{MA})_{n-1}\mathrm{Pb}_n\mathrm{I}_{3n+1}$ compounds for $n = 2, 3, 4$ in the same manner as described in previous chapter for the $n = 1$. It allowed obtaining consistent information about the optical properties of the whole series of 2DP compounds with varying values of n. This investigation revealed how exciton fine structure splitting (FSS) and excitonic g-factors evolve with varying quantum well thickness. Both quantities gradually approach bulk values with increasing n, consistent with reduced quantum confinement. These results show the evolution between the 2D and 3D regimes and emphasise the role of quantum and dielectric confinement in shaping excitonic properties.

Overall, the results presented in this thesis provide a reliable reference for theoretical modelling of phenomena occurring in 2D perovskites. The determination of the exciton fine structure, together with the confirmed energy spacing between states and their coupling to specific light polarisations, provides essential guidance for the design and optimisation of lead-halide perovskite optoelectronic devices.

Appendix A

Publications and Conferences

Publications based on the results presented in this thesis:

1. **K. Posmyk**, N. Zawadzka, Ł. Kipczak, M. Ł. Dyksik, A. Surrente, D. K. Maude, T. Kazimierczuk, A. Babiński, M. R. Molas, W. Bumrungsan, C. Chooseng, W. Paritmongkol, W. A. Tisdale, M. Baranowski, P. Płochocka
"Bright excitonic fine structure in metal-halide perovskites: from two-dimensional to bulk"
Journal of the American Chemical Society, vol. 146, nr 7, s. 4687-4694 (2024)

2. **K. Posmyk**, M. Ł. Dyksik, A. Surrente, D. K. Maude, N. Zawadzka, A. Babiński, M. R. Molas, W. Paritmongkol, M. Mączka, W. A. Tisdale, P. Płochocka, M. Baranowski
"Exciton fine structure in 2D perovskites: the out-of-plane excitonic state"
Advanced Optical Materials, vol. 12, nr 8, art. 2300877 (2024)

3. **K. Posmyk**, N. Zawadzka, M. Ł. Dyksik, A. Surrente, D. K. Maude, T. Kazimierczuk, A. Babiński, M. R. Molas, W. Paritmongkol, M. Mączka, W. A. Tisdale, P. Płochocka, M. Baranowski
"Quantification of exciton fine structure splitting in a two-dimensional perovskite compound"
Journal of Physical Chemistry Letters, vol. 13, nr 20, s. 4463-4469 (2022)

Other publications:

1. J. J. P. Thompson, M. Ł. Dyksik, P. Peksa, **K. Posmyk**, A. Joki, R. Perea-Causin, P. Erhart, M. Baranowski, M. A. Loi, P. Płochocka, E. Malic
"Phonon-bottleneck enhanced exciton emission in 2D perovskites"
Advanced Energy Materials, vol. 14, nr 20, art. 2304343 (2024)

2. M. Ł. Dyksik, D. Beret, M. Baranowski, H. Duim, S. Moyano, **K. Posmyk**, A. Mlayah, S. Adjokatse, D. K. Maude, M. A. Loi, P. Puech, P. Płochocka
"Polaron vibronic progression shapes the optical response of 2D perovskites"
Advanced Science, vol. 11, nr 7, art. 2305182 (2024)

3. N. Sokołowski, S. K. Palai, M. Ł. Dyksik, **K. Posmyk**, M. Baranowski, A. Surrente, D. K. Maude, F. Carrascoso, O. Cakiroglu, E. Sanchez, A. Schubert, C. Munuera, T. Taniguchi, K. Watanabe, J. Hagel, S. Brem, A. Castellanos-Gomez, E. Malic, P. Płochocka

"Twist-angle dependent dehybridization of momentum-indirect excitons in MoSe2/MoS2 heterostructures"
2D Materials, vol. 10, nr 3, art. 034003 (2023)

4. **K. Posmyk**, M. Ł. Dyksik, A. Surrente, K. Zalewska, M. Śmiertka, E. Cybula, W. Paritmongkol, W. A. Tisdale, P. Płochocka, M. Baranowski
   "Fine structure splitting of phonon-assisted excitonic transition in (PEA)2PbI4 two-dimensional perovskites"
   Nanomaterials, vol. 13, nr 6, art. 1119 (2023)

5. T. Smołka, **K. Posmyk**, M. Wasiluk, P. D. Wyborski, M. Gawełczyk, P. Mrowiński, M. Mikulicz, A. D. Zielińska, J. P. Reithmaier, A. J. Musiał, M. Benyoucef
   "Optical quality of InAs/InP quantum dots on distributed Bragg reflector emitting at 3rd telecom window grown by molecular beam epitaxy"
   Materials, vol. 14, nr 21, art. 6270 (2021)

Scientific conferences:

1. **Flatlands Beyond Graphene 2024**
   9-13 September 2024, Wrocław, Poland
   Poster presentation: *"Unravelling the excitonic landscape in hybrid organic-inorganic two-dimensional silver chalcogenolates"*
   K. Posmyk, P. Peksa, M. Ł. Dyksik, A. Surrente, W. S. Lee, W. A. Tisdale, P. Płochocka, M. Baranowski

2. **HMF25: 25th International Conference on High Magnetic Fields in Semiconductor Physics**
   16-20 September 2024, Warsaw, Poland
   Oral presentation: *"Unravelling the exciton fine structure in two-dimensional lead-halide perovskites"*
   K. Posmyk, N. Zawadzka, Ł. Kipczak, M. Ł. Dyksik, A. Surrente, D. K. Maude, T. Kazimierczuk, A. Babiński, M. R. Molas, W. Paritmongkol, M. Mączka, W. A. Tisdale, P. Płochocka, M. Baranowski

3. **ICANS30: 30th International Conference on Amorphous and Nanocrystalline Semiconductors**
   5-8 August 2024, Manchester, UK
   Invited oral presentation: *"Excitons in two-dimensional metal-halide perovskites"*
   K. Posmyk, N. Zawadzka, Ł. Kipczak, M. Ł. Dyksik, A. Surrente, D. K. Maude, T. Kazimierczuk, A. Babiński, M. R. Molas, W. Bumrungsan, C. Chooseng, W. Paritmongkol, M. Mączka, W. A. Tisdale, P. Płochocka, M. Baranowski

4. **2024 MRS Spring Meeting and Exhibit**
   April 22-26, 2024, Seattle, Washington
   Oral presentation: *"Magneto-optical studies of exciton fine structure in two-dimensional perovskites"*
   K. Posmyk, N. Zawadzka, Ł. Kipczak, M. Ł. Dyksik, A. Surrente, D. K. Maude, T. Kazimierczuk, A. Babiński, M. R. Molas, W. Paritmongkol, W. A. Tisdale, P. Płochocka, M. Baranowski

5. **52nd International School & Conference on the Physics of Semiconductors "Jaszowiec"**
   15-21 June 2024, Szczyrk, Poland
   Oral presentation: *"Revealing the excitonic landscape in mithrene – hybrid organic-inorganic two-dimensional semiconductor"*
   K. Posmyk, P. Peksa, M. Ł. Dyksik, A. Surrente, W. S. Lee, W. A. Tisdale, P. Płochocka, M. Baranowski

6. **International Workshop on 2D Materials**
   15-17 November 2023, Grenoble, France
   Invited oral presentation: *"Probing the exciton fine structure of 2D perovskites using magneto-optical spectroscopy"*
   K. Posmyk, N. Zawadzka, M. Ł. Dyksik, A. Surrente, D. K. Maude, T. Kazimierczuk, A. Babiński, M. R. Molas, M. Mączka, W. Paritmongkol, W. A. Tisdale, P. Płochocka, M. Baranowski

7. **22nd International Winterschool on New Developments in Solid State Physics**
   12-17 February 2023, Mauterndorf, Austria
   Poster presentation: *"Exciton fine structure in two-dimensional perovskites"*
   K. Posmyk, N. Zawadzka, M. Ł. Dyksik, A. Surrente, D. K. Maude, T. Kazimierczuk, A. Babiński, M. R. Molas, M. Mączka, W. Paritmongkol, W. A. Tisdale, P. Płochocka, M. Baranowski

8. **50th International School & Conference on the Physics of Semiconductors "Jaszowiec"**
   4-10 June 2022, Szczyrk, Poland
   Poster presentation: *"Revealing the full exciton fine structure in two-dimensional perovskites"*
   K. Posmyk, N. Zawadzka, M. Ł. Dyksik, A. Surrente, D. K. Maude, T. Kazimierczuk, A. Babiński, M. R. Molas, M. Mączka, W. Paritmongkol, W. A. Tisdale, P. Płochocka, M. Baranowski

William A. Tisdale
Professor & MacVicar Faculty Fellow

Massachusetts Institute of Technology
77 Massachusetts Avenue, Building 66–458
Cambridge, Massachusetts 02139–4307

Department of Chemical Engineering
School of Engineering

Office 617–253–4975
Fax 617–258–5766
Email tisdale@mit.edu
http://web.mit.edu/tisdalelab

February 20th, 2025

Permission to use

I hereby grant permission to use the pictures taken in the Tisdale Laboratory at MIT Department of Chemical Engineering, documenting the process of chemical synthesis of two-dimensional perovskites, in the doctoral dissertation of Ms. Katarzyna Posmyk.

William Tisdale

Bibliography

[Adachi 1992] Sadao Adachi. Physical properties of III-V semiconductor compounds. John Wiley & Sons, 1992. (Cited on page 40.)

[Ahn 2017] Jihoon Ahn, Eunsong Lee, Jeiwan Tan, Wooseok Yang, Bokyung Kim and Jooho Moon. *A new class of chiral semiconductors: chiral-organic-molecule-incorporating organic–inorganic hybrid perovskites.* Materials Horizons, vol. 4, no. 5, pages 851–856, 2017. (Cited on page 12.)

[Akkerman 2016] Quinten A Akkerman, Silvia Genaro Motti, Ajay Ram Srimath Kandada, Edoardo Mosconi, Valerio D'Innocenzo, Giovanni Bertoni, Sergio Marras, Brett A Kamino, Laura Miranda, Filippo De Angelis*et al. Solution synthesis approach to colloidal cesium lead halide perovskite nanoplatelets with monolayer-level thickness control.* Journal of the American Chemical Society, vol. 138, no. 3, pages 1010–1016, 2016. (Cited on page 10.)

[Akkerman 2018] Quinten A Akkerman, Gabriele Rainò, Maksym V Kovalenko and Liberato Manna. *Genesis, challenges and opportunities for colloidal lead halide perovskite nanocrystals.* Nature Materials, vol. 17, no. 5, pages 394–405, 2018. (Cited on page 10.)

[Akkerman 2022] Quinten A Akkerman, Tan PT Nguyen, Simon C Boehme, Federico Montanarella, Dmitry N Dirin, Philipp Wechsler, Finn Beiglböck, Gabriele Rainò, Rolf Erni, Claudine Katan*et al. Controlling the nucleation and growth kinetics of lead halide perovskite quantum dots.* Science, vol. 377, no. 6613, pages 1406–1412, 2022. (Cited on page 10.)

[Baikie 2013] Tom Baikie, Yanan Fang, Jeannette M Kadro, Martin Schreyer, Fengxia Wei, Subodh G Mhaisalkar, Michael Graetzel and Tim J White. *Synthesis and crystal chemistry of the hybrid perovskite* $(CH_3NH_3)PbI_3$ *for solid-state sensitised solar cell applications.* Journal of Materials Chemistry A, vol. 1, no. 18, pages 5628–5641, 2013. (Cited on page 9.)

[Bajaj 1974] KK Bajaj. *Effect of electron-phonon interaction on the binding energy of a Wannier exciton in a polarizable medium.* Solid State Communications, vol. 15, no. 7, pages 1221–1224, 1974. (Cited on page 22.)

[Ball 2016] James M Ball and Annamaria Petrozza. *Defects in perovskite-halides and their effects in solar cells.* Nature Energy, vol. 1, no. 11, pages 1–13, 2016. (Cited on page 3.)

[Baranowski 2019a] Michał Baranowski, Krzysztof Galkowski, Alessandro Surrente, Joanna Urban, Łukasz Kłopotowski, Sebastian Maćkowski, Duncan Kennedy

Maude, Rim Ben Aich, Kais Boujdaria, Maria Chamarro*et al.* *Giant fine structure splitting of the bright exciton in a bulk $MAPbBr_3$ single crystal.* Nano Letters, vol. 19, no. 10, pages 7054–7061, 2019. (Cited on pages 56, 71, 74 and 75.)

[Baranowski 2019b] Michal Baranowski, Szymon J Zelewski, Mikael Kepenekian, Boubacar Traoré, Joanna M Urban, Alessandro Surrente, Krzysztof Galkowski, Duncan K Maude, Agnieszka Kuc, Edward P Booker*et al.* *Phase-transition-induced carrier mass enhancement in 2D Ruddlesden–Popper perovskites.* ACS Energy Letters, vol. 4, no. 10, pages 2386–2392, 2019. (Cited on pages 27 and 74.)

[Baranowski 2020] Michal Baranowski and Paulina Plochocka. *Excitons in metal-halide perovskites.* Advanced Energy Materials, vol. 10, no. 26, page 1903659, 2020. (Cited on pages 20 and 22.)

[Baranowski 2024] Michal Baranowski, Andrzej Nowok, Krzysztof Galkowski, Mateusz Dyksik, Alessandro Surrente, Duncan Maude, Marios Zacharias, George Volonakis, Samuel D Stranks, Jacky Even*et al.* *Polaronic Mass Enhancement and Polaronic Excitons in Metal Halide Perovskites.* ACS Energy Letters, vol. 9, pages 2696–2702, 2024. (Cited on pages 22 and 27.)

[Bayer 2002] M Bayer, G Ortner, O Stern, A Kuther, AA Gorbunov, A Forchel, Pawel Hawrylak, S Fafard, K Hinzer, TL Reinecke*et al.* *Fine structure of neutral and charged excitons in self-assembled In (Ga) As/(Al) GaAs quantum dots.* Physical Review B, vol. 65, no. 19, page 195315, 2002. (Cited on pages 22 and 25.)

[Ben Aich 2020] R Ben Aich, S Ben Radhia, K Boujdaria, M Chamarro and C Testelin. *Multiband $k{\cdot}p$ model for tetragonal crystals: application to hybrid halide perovskite nanocrystals.* The Journal of Physical Chemistry Letters, vol. 11, no. 3, pages 808–817, 2020. (Cited on pages 65 and 67.)

[Bett 1999] Andreas W Bett, Frank Dimroth, G Stollwerck and OV Sulima. *III-V compounds for solar cell applications.* Applied Physics A, vol. 69, pages 119–129, 1999. (Cited on page 2.)

[Biffi 2023] Giulia Biffi, Yeongsu Cho, Roman Krahne and Timothy C Berkelbach. *Excitons and their fine structure in lead halide perovskite nanocrystals from atomistic GW/BSE calculations.* The Journal of Physical Chemistry C, vol. 127, no. 4, pages 1891–1898, 2023. (Cited on page 65.)

[Billing 2007] David G Billing and Andreas Lemmerer. *Synthesis, characterization and phase transitions in the inorganic–organic layered perovskite-type hybrids $[(C_nH_{2n+1}NH_3)_2PbI_4]$, n= 4, 5 and 6.* Acta Crystallographica Section B: Structural Science, vol. 63, no. 5, pages 735–747, 2007. (Cited on page 12.)

[Billing 2008] David G Billing and Andreas Lemmerer. *Synthesis, characterization and phase transitions of the inorganic–organic layered perovskite-type hybrids* $[(C_nH_{2n+1}NH_3)_2PbI_4]$*(n= 12, 14, 16 and 18)*. New Journal of Chemistry, vol. 32, no. 10, pages 1736–1746, 2008. (Cited on page 12.)

[Bir 1974] Gennadiĭ Levikovich Bir and Grigoriĭ Ezekielevich Pikus. *Symmetry and strain-induced effects in semiconductors*. New York, 1974. (Cited on page 22.)

[Blancon 2018] J-C Blancon, Andreas V Stier, Hsinhan Tsai, Wanyi Nie, Costas C Stoumpos, Boubacar Traore, L Pedesseau, Mikael Kepenekian, Fumiya Katsutani, GT Noe*et al.* *Scaling law for excitons in 2D perovskite quantum wells*. Nature Communications, vol. 9, no. 1, page 2254, 2018. (Cited on pages 11, 19, 22, 71 and 72.)

[Brandt 2015] Riley E Brandt, Vladan Stevanović, David S Ginley and Tonio Buonassisi. *Identifying defect-tolerant semiconductors with high minority-carrier lifetimes: beyond hybrid lead halide perovskites*. Mrs Communications, vol. 5, no. 2, pages 265–275, 2015. (Cited on page 3.)

[Brandt 2017] Riley E Brandt, Jeremy R Poindexter, Prashun Gorai, Rachel C Kurchin, Robert LZ Hoye, Lea Nienhaus, Mark WB Wilson, J Alexander Polizzotti, Raimundas Sereika, Raimundas Zaltauskas*et al.* *Searching for "defect-tolerant" photovoltaic materials: combined theoretical and experimental screening*. Chemistry of Materials, vol. 29, no. 11, pages 4667–4674, 2017. (Cited on page 3.)

[Buizza 2021] Leonardo RV Buizza and Laura M Herz. *Polarons and charge localization in metal-halide semiconductors for photovoltaic and light-emitting devices*. Advanced Materials, vol. 33, no. 24, page 2007057, 2021. (Cited on page 3.)

[Cao 2023] Yang Bryan Cao, Daquan Zhang, Qianpeng Zhang, Xiao Qiu, Yu Zhou, Swapnadeep Poddar, Yu Fu, Yudong Zhu, Jin-Feng Liao, Lei Shu*et al.* *High-efficiency, flexible and large-area red/green/blue all-inorganic metal halide perovskite quantum wires-based light-emitting diodes*. Nature Communications, vol. 14, no. 1, page 4611, 2023. (Cited on page 1.)

[Chen 2018a] Cheng Chen, Xiangmin Hu, Wengao Lu, Shuai Chang, Lijie Shi, Liang Li, Haizheng Zhong and Jun-Bo Han. *Elucidating the phase transitions and temperature-dependent photoluminescence of* $MAPbBr_3$ *single crystal*. Journal of Physics D: Applied Physics, vol. 51, no. 4, page 045105, 2018. (Cited on page 9.)

[Chen 2018b] Yani Chen, Yong Sun, Jiajun Peng, Junhui Tang, Kaibo Zheng and Ziqi Liang. *2D Ruddlesden–Popper perovskites for optoelectronics*. Advanced Materials, vol. 30, no. 2, page 1703487, 2018. (Cited on pages 1 and 7.)

[Chen 2019] Chao Chen, Liang Gao, Wanru Gao, Cong Ge, Xinyuan Du, Zha Li, Ying Yang, Guangda Niu and Jiang Tang. *Circularly polarized light detection using chiral hybrid perovskite*. Nature Communications, vol. 10, no. 1, page 1927, 2019. (Cited on page 12.)

[Chernikov 2014] Alexey Chernikov, Timothy C Berkelbach, Heather M Hill, Albert Rigosi, Yilei Li, Burak Aslan, David R Reichman, Mark S Hybertsen and Tony F Heinz. *Exciton binding energy and nonhydrogenic Rydberg series in monolayer* WS_2. Physical Review Letters, vol. 113, no. 7, page 076802, 2014. (Cited on pages 18 and 19.)

[Dang 2015] Yangyang Dang, Yang Liu, Youxuan Sun, Dongsheng Yuan, Xiaolong Liu, Weiqun Lu, Guangfeng Liu, Haibing Xia and Xutang Tao. *Bulk crystal growth of hybrid perovskite material* $CH_3NH_3PbI_3$. CrystEngComm, vol. 17, no. 3, pages 665–670, 2015. (Cited on page 4.)

[Dar 2016] M Ibrahim Dar, Gwénolé Jacopin, Simone Meloni, Alessandro Mattoni, Neha Arora, Ariadni Boziki, Shaik Mohammed Zakeeruddin, Ursula Rothlisberger and Michael Grätzel. *Origin of unusual bandgap shift and dual emission in organic-inorganic lead halide perovskites*. Science Advances, vol. 2, no. 10, page e1601156, 2016. (Cited on page 72.)

[Devreese 1996] Jozef T Devreese. *Polarons*. In Encyclopedia of applied physics: vol. 14, page 383. Wiley-VCH Publishers, Inc., 1996. (Cited on page 21.)

[Dion 1981] Michel Dion, Marcel Ganne and Michel Tournoux. *Nouvelles familles de phases* $M^I M_2^{II} Nb_3 O_{10}$ *a feuillets "perovskites"*. Materials Research Bulletin, vol. 16, no. 11, pages 1429–1435, 1981. (Cited on page 7.)

[Do 2020] T Thu Ha Do, Andres Granados del Aguila, Dong Zhang, Jun Xing, Sheng Liu, MA Prosnikov, Weibo Gao, Kai Chang, Peter CM Christianen and Qihua Xiong. *Bright exciton fine-structure in two-dimensional lead halide perovskites*. Nano Letters, vol. 20, no. 7, pages 5141–5148, 2020. (Cited on page 71.)

[Du 2017] Ke-zhao Du, Qing Tu, Xu Zhang, Qiwei Han, Jie Liu, Stefan Zauscher and David B Mitzi. *Two-dimensional lead (II) halide-based hybrid perovskites templated by acene alkylamines: crystal structures, optical properties, and piezoelectricity*. Inorganic Chemistry, vol. 56, no. 15, pages 9291–9302, 2017. (Cited on pages 7, 35 and 36.)

[Dyksik 2020] Mateusz Dyksik, Herman Duim, Xiangzhou Zhu, Zhuo Yang, Masaki Gen, Yoshimitsu Kohama, Sampson Adjokatse, Duncan K Maude, Maria Antonietta Loi, David A Egger*et al.* *Broad tunability of carrier effective masses in two-dimensional halide perovskites*. ACS Energy Letters, vol. 5, no. 11, pages 3609–3616, 2020. (Cited on pages 12, 27, 63, 67 and 71.)

[Dyksik 2021a] Mateusz Dyksik, Herman Duim, Duncan K Maude, Michal Baranowski, Maria Antonietta Loi and Paulina Plochocka. *Brightening of dark excitons in 2D perovskites.* Science advances, vol. 7, no. 46, page eabk0904, 2021. (Cited on pages 26, 67, 71 and 79.)

[Dyksik 2021b] Mateusz Dyksik, Shuli Wang, Watcharaphol Paritmongkol, Duncan K Maude, William A Tisdale, Michal Baranowski and Paulina Plochocka. *Tuning the excitonic properties of the 2D* $(PEA)_2(MA)_{n-1}Pb_nI_{3n+1}$ *perovskite family via quantum confinement.* The Journal of Physical Chemistry Letters, vol. 12, no. 6, pages 1638–1643, 2021. (Cited on pages 27, 36, 72, 75, 78 and 80.)

[Ema 2006] K Ema, K Umeda, M Toda, C Yajima, Y Arai, H Kunugita, D Wolverson and JJ Davies. *Huge exchange energy and fine structure of excitons in an organic-inorganic quantum well material.* Physical Review B—Condensed Matter and Materials Physics, vol. 73, no. 24, page 241310, 2006. (Cited on pages 26 and 67.)

[Even 2013] Jacky Even, Laurent Pedesseau, Jean-Marc Jancu and Claudine Katan. *Importance of spin–orbit coupling in hybrid organic/inorganic perovskites for photovoltaic applications.* The Journal of Physical Chemistry Letters, vol. 4, no. 17, pages 2999–3005, 2013. (Cited on pages 12, 13 and 53.)

[Even 2015] Jacky Even, Laurent Pedesseau, Claudine Katan, Mikaël Kepenekian, Jean-Sébastien Lauret, Daniel Sapori and Emmanuelle Deleporte. *Solid-state physics perspective on hybrid perovskite semiconductors.* The Journal of Physical Chemistry C, vol. 119, no. 19, pages 10161–10177, 2015. (Cited on page 35.)

[Fakharuddin 2022] Azhar Fakharuddin, Mahesh K Gangishetty, Mojtaba Abdi-Jalebi, Sang-Hyun Chin, Abd Rashid bin Mohd Yusoff, Daniel N Congreve, Wolfgang Tress, Felix Deschler, Maria Vasilopoulou and Henk J Bolink. *Perovskite light-emitting diodes.* Nature Electronics, vol. 5, no. 4, pages 203–216, 2022. (Cited on pages 1 and 2.)

[Fan 1967] H Fan and L Genzel. *Light and Matter Ia/Licht und Materie Ia*, 1967. (Cited on page 21.)

[Feldstein 2020] David Feldstein, Raul Perea-Causin, Shuli Wang, Mateusz Dyksik, Kenji Watanabe, Takashi Taniguchi, Paulina Plochocka and Ermin Malic. *Microscopic picture of electron–phonon interaction in two-dimensional halide perovskites.* The Journal of Physical Chemistry Letters, vol. 11, no. 23, pages 9975–9982, 2020. (Cited on page 19.)

[Feynman 1955] Richard Phillips Feynman. *Slow electrons in a polar crystal.* Physical Review, vol. 97, no. 3, page 660, 1955. (Cited on page 21.)

[Fieramosca 2018] Antonio Fieramosca, Luisa De Marco, Marco Passoni, Laura Polimeno, Aurora Rizzo, Barbara LT Rosa, Giuseppe Cruciani, Lorenzo Dominici, Milena De Giorgi, Giuseppe Gigli*et al.* *Tunable out-of-plane excitons in 2D single-crystal perovskites*. ACS Photonics, vol. 5, no. 10, pages 4179–4185, 2018. (Cited on page 26.)

[Filip 2022] Marina R Filip, Diana Y Qiu, Mauro Del Ben and Jeffrey B Neaton. *Screening of excitons by organic cations in quasi-two-dimensional organic–inorganic lead-halide perovskites*. Nano Letters, vol. 22, no. 12, pages 4870–4878, 2022. (Cited on page 23.)

[Folpini 2020] Giulia Folpini, Daniele Cortecchia, Annamaria Petrozza and Ajay Ram Srimath Kandada. *The role of a dark exciton reservoir in the luminescence efficiency of two-dimensional tin iodide perovskites*. Journal of Materials Chemistry C, vol. 8, no. 31, pages 10889–10896, 2020. (Cited on page 34.)

[Fox 2010] Mark Fox. Optical properties of solids, volume 3. Oxford university press, 2010. (Cited on pages 20, 39, 42 and 44.)

[Frenkel 1931] Jacov Frenkel. *On the transformation of light into heat in solids. II*. Physical Review, vol. 37, no. 10, page 1276, 1931. (Cited on page 14.)

[Frost 2017] Jarvist Moore Frost. *Calculating polaron mobility in halide perovskites*. Physical Review B, vol. 96, no. 19, page 195202, 2017. (Cited on page 21.)

[Fu 1999] Huaxiang Fu, Lin-Wang Wang and Alex Zunger. *Excitonic exchange splitting in bulk semiconductors*. Physical Review B, vol. 59, no. 8, page 5568, 1999. (Cited on page 75.)

[Fu 2017] Ming Fu, Philippe Tamarat, He Huang, Jacky Even, Andrey L Rogach and Brahim Lounis. *Neutral and charged exciton fine structure in single lead halide perovskite nanocrystals revealed by magneto-optical spectroscopy*. Nano Letters, vol. 17, no. 5, pages 2895–2901, 2017. (Cited on page 26.)

[Fu 2023] Dongying Fu, Wenjuan Jia, Shichao Wu, Junli Chang, Zhuo Chen and Junhua Luo. *Bilayered Dion–Jacobson hybrid perovskite bulk single crystals constructed with aromatic diammonium for ultraviolet–visible–near-infrared photodetection*. Chemistry of Materials, vol. 35, no. 6, pages 2541–2548, 2023. (Cited on page 7.)

[Galkowski 2017] Krzysztof Galkowski, AA Mitioglu, Alessandro Surrente, Zhuo Yang, Duncan Kennedy Maude, Piotr Kossacki, Giles E Eperon, JT-W Wang, Henry James Snaith, Paulina Plochocka and Robin J Nicholas. *Spatially resolved studies of the phases and morphology of methylammonium and formamidinium lead tri-halide perovskites*. Nanoscale, vol. 9, no. 9, pages 3222–3230, 2017. (Cited on page 9.)

[Galkowski 2019] Krzysztof Galkowski, Alessandro Surrente, Michal Baranowski, Baodan Zhao, Zhuo Yang, Aditya Sadhanala, Sebastian Mackowski, Samuel D Stranks and Paulina Plochocka. *Excitonic properties of low-band-gap lead–tin halide perovskites.* ACS Energy Letters, vol. 4, no. 3, pages 615–621, 2019. (Cited on page 27.)

[Gan 2019] Zhixing Gan, Xiaoming Wen, Chunhua Zhou, Weijian Chen, Fei Zheng, Shuang Yang, Jeffrey A Davis, Patrick C Tapping, Tak W Kee, Hua Zhang*et al.* *Transient energy reservoir in 2D perovskites.* Advanced Optical Materials, vol. 7, no. 22, page 1900971, 2019. (Cited on page 34.)

[Gao 2014] Peng Gao, Michael Grätzel and Mohammad K Nazeeruddin. *Organohalide lead perovskites for photovoltaic applications.* Energy & Environmental Science, vol. 7, no. 8, pages 2448–2463, 2014. (Cited on page 8.)

[Gao 2022] Yuanji Gao, Keqing Huang, Caoyu Long, Yang Ding, Jianhui Chang, Dou Zhang, Lioz Etgar, Mingzhen Liu, Jian Zhang and Junliang Yang. *Flexible perovskite solar cells: From materials and device architectures to applications.* ACS Energy Letters, vol. 7, no. 4, pages 1412–1445, 2022. (Cited on page 2.)

[Giorgi 2018] Giacomo Giorgi, Koichi Yamashita and Maurizia Palummo. *Nature of the electronic and optical excitations of ruddlesden–popper hybrid organic–inorganic perovskites: the role of the many-body interactions.* The Journal of Physical Chemistry Letters, vol. 9, no. 19, pages 5891–5896, 2018. (Cited on page 23.)

[Goldschmidt 1927] VM Goldschmidt. *Crystal structure and chemical composition.* Reports of the German Chemical Society (A and B Series), vol. 60, no. 5, pages 1263–1296, 1927. (Cited on page 5.)

[Green 2014] Martin A Green, Anita Ho-Baillie and Henry J Snaith. *The emergence of perovskite solar cells.* Nature Photonics, vol. 8, no. 7, pages 506–514, 2014. (Cited on page 1.)

[Green 2024] Martin A Green, Ewan D Dunlop, Masahiro Yoshita, Nikos Kopidakis, Karsten Bothe, Gerald Siefer, David Hinken, Michael Rauer, Jochen Hohl-Ebinger and Xiaojing Hao. *Solar cell efficiency tables (Version 64).* Progress in Photovoltaics: Research and Applications, vol. 32, no. 7, pages 425–441, 2024. (Cited on page 1.)

[Guilloux 2023] Victor Guilloux, Amal Ghribi, Silbé Majrab, Florent Margaillan, Mathieu Bernard, Frédérick Bernardot, Laurent Legrand, Emmanuel Lhuillier, Kaïs Boujdaria, Maria Chamarro*et al.* *Exciton Fine Structure of* $CsPbCl_3$ *Nanocrystals: An Interplay of Electron–Hole Exchange Interaction, Crystal Structure, Shape Anisotropy, and Dielectric Mismatch.* ACS Nano, vol. 17, no. 13, pages 12266–12277, 2023. (Cited on page 75.)

[Haken 1958] Hermann Haken. *Die theorie des exzitons im festen Körper.* Fortschritte der Physik, vol. 6, no. 6, pages 271–334, 1958. (Cited on page 22.)

[Hansen 2023] Kameron R Hansen, Cindy Y Wong, C Emma McClure, Blake Romrell, Laura Flannery, Daniel Powell, Kelsey Garden, Alex Berzansky, Michele Eggleston, Daniel J King*et al. Mechanistic origins of excitonic properties in 2D perovskites: Implications for exciton engineering.* Matter, vol. 6, no. 10, pages 3463–3482, 2023. (Cited on page 56.)

[Herz 2018] Laura M Herz. *How lattice dynamics moderate the electronic properties of metal-halide perovskites.* The Journal of Physical Chemistry Letters, vol. 9, no. 23, pages 6853–6863, 2018. (Cited on pages 20, 21 and 22.)

[Hoke 2015] Eric T Hoke, Daniel J Slotcavage, Emma R Dohner, Andrea R Bowring, Hemamala I Karunadasa and Michael D McGehee. *Reversible photo-induced trap formation in mixed-halide hybrid perovskites for photovoltaics.* Chemical Science, vol. 6, no. 1, pages 613–617, 2015. (Cited on pages 2 and 9.)

[Hong 1992] X Hong, T Ishihara and AV Nurmikko. *Dielectric confinement effect on excitons in* PbI_4*-based layered semiconductors.* Physical Review B, vol. 45, no. 12, page 6961, 1992. (Cited on pages 11 and 12.)

[Hopcroft 2010] Matthew A Hopcroft, William D Nix and Thomas W Kenny. *What is the Young's Modulus of Silicon?* Journal of Microelectromechanical Systems, vol. 19, no. 2, pages 229–238, 2010. (Cited on page 3.)

[Huber 2018] Daniel Huber, Marcus Reindl, Johannes Aberl, Armando Rastelli and Rinaldo Trotta. *Semiconductor quantum dots as an ideal source of polarization-entangled photon pairs on-demand: a review.* Journal of Optics, vol. 20, no. 7, page 073002, 2018. (Cited on page 25.)

[Hurtado Parra 2022] Sebastian Hurtado Parra, Daniel B Straus, Bryan T Fichera, Natasha Iotov, Cherie R Kagan and James M Kikkawa. *Large exciton polaron formation in 2D hybrid perovskites via time-resolved photoluminescence.* ACS Nano, vol. 16, no. 12, pages 21259–21265, 2022. (Cited on page 59.)

[Ishihara 1994] Teruya Ishihara. *Optical properties of PbI-based perovskite structures.* Journal of Luminescence, vol. 60, pages 269–274, 1994. (Cited on page 35.)

[Ivchenko 2005] Eougenious L Ivchenko. Optical spectroscopy of semiconductor nanostructures. Alpha Science Int'l Ltd., 2005. (Cited on page 27.)

[Jacobson 1985] AJ Jacobson, Jack W Johnson and JT Lewandowski. *Interlayer chemistry between thick transition-metal oxide layers: synthesis and intercalation reactions of K* $[Ca_2Na_{n-3}Nb_nO_{3n+1}]$*(3. ltoreq. n. ltoreq. 7)*. Inorganic Chemistry, vol. 24, no. 23, pages 3727–3729, 1985. (Cited on page 7.)

[Jana 2020] Manoj K Jana, Ruyi Song, Haoliang Liu, Dipak Raj Khanal, Svenja M Janke, Rundong Zhao, Chi Liu, Z Valy Vardeny, Volker Blum and David B Mitzi. *Organic-to-inorganic structural chirality transfer in a 2D hybrid perovskite and impact on Rashba-Dresselhaus spin-orbit coupling.* Nature communications, vol. 11, no. 1, page 4699, 2020. (Cited on page 12.)

[Jin 2020] Handong Jin, Elke Debroye, Masoumeh Keshavarz, Ivan G Scheblykin, Maarten BJ Roeffaers, Johan Hofkens and Julian A Steele. *It's a trap! On the nature of localised states and charge trapping in lead halide perovskites.* Materials Horizons, vol. 7, no. 2, pages 397–410, 2020. (Cited on page 72.)

[Jung 2015] Hyun Suk Jung and Nam-Gyu Park. *Perovskite solar cells: from materials to devices.* Small, vol. 11, no. 1, pages 10–25, 2015. (Cited on page 1.)

[Kagan 1999] Cherie R Kagan, David B Mitzi and Christos D Dimitrakopoulos. *Organic-inorganic hybrid materials as semiconducting channels in thin-film field-effect transistors.* Science, vol. 286, no. 5441, pages 945–947, 1999. (Cited on page 3.)

[Kahmann 2021] Simon Kahmann, Herman Duim, Hong-Hua Fang, Mateusz Dyksik, Sampson Adjokatse, Martha Rivera Medina, Matteo Pitaro, Paulina Plochocka and Maria A Loi. *Photophysics of two-dimensional perovskites—learning from metal halide substitution.* Advanced Functional Materials, vol. 31, no. 46, page 2103778, 2021. (Cited on page 72.)

[Kamminga 2016] Machteld E Kamminga, Hong-Hua Fang, Marina R Filip, Feliciano Giustino, Jacob Baas, Graeme R Blake, Maria Antonietta Loi and Thomas TM Palstra. *Confinement effects in low-dimensional lead iodide perovskite hybrids.* Chemistry of Materials, vol. 28, no. 13, pages 4554–4562, 2016. (Cited on page 3.)

[Karpińska 2022] M Karpińska, J Jasiński, R Kempt, JD Ziegler, H Sansom, T Taniguchi, K Watanabe, HJ Snaith, A Surrente, M Dyksik*et al. Interlayer excitons in* $MoSe_2$*/2D perovskite hybrid heterostructures–the interplay between charge and energy transfer.* Nanoscale, vol. 14, no. 22, pages 8085–8095, 2022. (Cited on page 8.)

[Kataoka 1993] Takeshi Kataoka, Takashi Kondo, Ryoichi Ito, Satoshi Sasaki, Kazuhito Uchida and Noboru Miura. *Magneto-optical study on excitonic spectra in* $(C_6H_{13}NH_3)_2PbI_4$. Physical Review B, vol. 47, no. 4, page 2010, 1993. (Cited on pages 29, 35, 48, 65 and 67.)

[Keldysh 1979] LV Keldysh. *Coulomb interaction in thin semiconductor and semimetal films.* Soviet Journal of Experimental and Theoretical Physics Letters, vol. 29, page 658, 1979. (Cited on page 19.)

[Kéna-Cohen 2010] Stéphane Kéna-Cohen. Strong exciton-photon coupling in organic semiconductor microcavities. Princeton University, 2010. (Cited on page 14.)

[Kikuchi 2004] K Kikuchi, Y Takeoka, M Rikukawa and K Sanui. *Structure and optical properties of lead iodide based two-dimensional perovskite compounds containing fluorophenethylamines.* Current Applied Physics, vol. 4, no. 6, pages 599–602, 2004. (Cited on page 35.)

[Kim 2020] Guan-Woo Kim and Annamaria Petrozza. *Defect tolerance and intolerance in metal-halide perovskites.* Advanced Energy Materials, vol. 10, no. 37, page 2001959, 2020. (Cited on page 3.)

[Kirstein 2022a] Erik Kirstein, Dmitri R Yakovlev, Mikhail M Glazov, Evgeny A Zhukov, Dennis Kudlacik, Ina V Kalitukha, Victor F Sapega, Grigorii S Dimitriev, Marina A Semina, Mikhail O Nestoklon*et al. The Landé factors of electrons and holes in lead halide perovskites: universal dependence on the band gap.* Nature communications, vol. 13, no. 1, page 3062, 2022. (Cited on pages 13, 27, 79 and 80.)

[Kirstein 2022b] Erik Kirstein, Evgeny A Zhukov, Dmitri R Yakovlev, Nataliia E Kopteva, Carolin Harkort, Dennis Kudlacik, Oleh Hordiichuk, Maksym V Kovalenko and Manfred Bayer. *Coherent spin dynamics of electrons in two-dimensional* $(PEA)_2PbI_4$ *perovskites.* Nano Letters, vol. 23, no. 1, pages 205–212, 2022. (Cited on page 67.)

[Kitazawa 2012] Nobuaki Kitazawa, Masami Aono and Yoshihisa Watanabe. *Temperature-dependent time-resolved photoluminescence of* $(C_6H_5C_2H_4NH_3)_2PbX_4$ *(X= Br and I).* Materials Chemistry and Physics, vol. 134, no. 2-3, pages 875–880, 2012. (Cited on page 35.)

[Knutson 2005] Jeremy L Knutson, James D Martin and David B Mitzi. *Tuning the band gap in hybrid tin iodide perovskite semiconductors using structural templating.* Inorganic Chemistry, vol. 44, no. 13, pages 4699–4705, 2005. (Cited on page 11.)

[Kojima 2009] Akihiro Kojima, Kenjiro Teshima, Yasuo Shirai and Tsutomu Miyasaka. *Organometal halide perovskites as visible-light sensitizers for photovoltaic cells.* Journal of the American Chemical Society, vol. 131, no. 17, pages 6050–6051, 2009. (Cited on page 1.)

[Kopidakis 2024] Nikos Kopidakis. *NREL Best Research-Cell Efficiency Chart*, 2024. (Cited on pages 1 and 2.)

[Landé 1921] Alfred Landé. *Über den anomalen zeemaneffekt (teil i).* Zeitschrift für Physik, vol. 5, no. 4, pages 231–241, 1921. (Cited on page 27.)

[Lanzetta 2021] Luis Lanzetta, Thomas Webb, Nourdine Zibouche, Xinxing Liang, Dong Ding, Ganghong Min, Robert JE Westbrook, Benedetta Gaggio, Thomas J Macdonald, M Saiful Islam*et al. Degradation mechanism of hybrid tin-based perovskite solar cells and the critical role of tin (IV) iodide.* Nature Communications, vol. 12, no. 1, page 2853, 2021. (Cited on page 5.)

[Lee 2012] Michael M Lee, Joël Teuscher, Tsutomu Miyasaka, Takurou N Murakami and Henry J Snaith. *Efficient hybrid solar cells based on meso-superstructured organometal halide perovskites.* Science, vol. 338, no. 6107, pages 643–647, 2012. (Cited on page 1.)

[Leguy 2016] Aurélien MA Leguy, Alejandro R Goñi, Jarvist M Frost, Jonathan Skelton, Federico Brivio, Xabier Rodríguez-Martínez, Oliver J Weber, Anuradha Pallipurath, M Isabel Alonso, Mariano Campoy-Quiles*et al. Dynamic disorder, phonon lifetimes, and the assignment of modes to the vibrational spectra of methylammonium lead halide perovskites.* Physical Chemistry Chemical Physics, vol. 18, no. 39, pages 27051–27066, 2016. (Cited on page 21.)

[Leijtens 2017] Tomas Leijtens, Rohit Prasanna, Aryeh Gold-Parker, Michael F Toney and Michael D McGehee. *Mechanism of tin oxidation and stabilization by lead substitution in tin halide perovskites.* ACS Energy Letters, vol. 2, no. 9, pages 2159–2165, 2017. (Cited on page 5.)

[Lemmerer 2012] Andreas Lemmerer and David G Billing. *Synthesis, characterization and phase transitions of the inorganic–organic layered perovskite-type hybrids* $[(C_nH_{2n+1}NH_3)_2\ PbI_4]$*, n= 7, 8, 9 and 10.* Dalton Transactions, vol. 41, no. 4, pages 1146–1157, 2012. (Cited on page 12.)

[Létoublon 2016] Antoine Létoublon, Serge Paofai, Benoit Ruffle, Philippe Bourges, Bernard Hehlen, Thierry Michel, Claude Ecolivet, Olivier Durand, Stéphane Cordier, Claudine Katan*et al. Elastic constants, optical phonons, and molecular relaxations in the high temperature plastic phase of the* $CH_3NH_3PbBr_3$ *hybrid perovskite.* The Journal of Physical Chemistry Letters, vol. 7, no. 19, pages 3776–3784, 2016. (Cited on page 21.)

[Li 2008] Chonghea Li, Xionggang Lu, Weizhong Ding, Liming Feng, Yonghui Gao and Ziming Guo. *Formability of* ABX_3 *(x= F, Cl, Br, I) halide perovskites.* Acta Crystallographica Section B: Structural Science, vol. 64, no. 6, pages 702–707, 2008. (Cited on page 5.)

[Li 2021] Xiaotong Li, Justin M Hoffman and Mercouri G Kanatzidis. *The 2D halide perovskite rulebook: how the spacer influences everything from the structure* *to optoelectronic device efficiency.* Chemical Reviews, vol. 121, no. 4, pages 2230–2291, 2021. (Cited on pages 6 and 11.)

[Li 2022] Ludong Li, Yurui Wang, Xiaoyu Wang, Renxing Lin, Xin Luo, Zhou Liu, Kun Zhou, Shaobing Xiong, Qinye Bao, Gang Chen*et al.* *Flexible all-perovskite tandem solar cells approaching 25% efficiency with molecule-bridged hole-selective contact.* Nature Energy, vol. 7, no. 8, pages 708–717, 2022. (Cited on pages 2 and 3.)

[Liang 2016] Dong Liang, Yuelin Peng, Yongping Fu, Melinda J Shearer, Jingjing Zhang, Jianyuan Zhai, Yi Zhang, Robert J Hamers, Trisha L Andrew and Song Jin. *Color-pure violet-light-emitting diodes based on layered lead halide perovskite nanoplates.* ACS Nano, vol. 10, no. 7, pages 6897–6904, 2016. (Cited on page 3.)

[Liao 2017] Yuqin Liao, Hefei Liu, Wenjia Zhou, Dongwen Yang, Yuequn Shang, Zhifang Shi, Binghan Li, Xianyuan Jiang, Lijun Zhang, Li Na Quan*et al.* *Highly oriented low-dimensional tin halide perovskites with enhanced stability and photovoltaic performance.* Journal of the American Chemical Society, vol. 139, no. 19, pages 6693–6699, 2017. (Cited on page 3.)

[Liu 2019] Yuhang Liu, Seckin Akin, Linfeng Pan, Ryusuke Uchida, Neha Arora, Jovana V Milić, Alexander Hinderhofer, Frank Schreiber, Alexander R Uhl, Shaik M Zakeeruddin*et al.* *Ultrahydrophobic 3D/2D fluoroarene bilayer-based water-resistant perovskite solar cells with efficiencies exceeding 22%.* Science Advances, vol. 5, no. 6, page eaaw2543, 2019. (Cited on pages 1 and 5.)

[Liu 2021] Albert Liu, Diogo B Almeida, Luiz G Bonato, Gabriel Nagamine, Luiz F Zagonel, Ana F Nogueira, Lazaro A Padilha and ST Cundiff. *Multidimensional coherent spectroscopy reveals triplet state coherences in cesium lead-halide perovskite nanocrystals.* Science Advances, vol. 7, no. 1, page eabb3594, 2021. (Cited on page 26.)

[Liu 2023] Sanwan Liu, Vasudevan P Biju, Yabing Qi, Wei Chen and Zonghao Liu. *Recent progress in the development of high-efficiency inverted perovskite solar cells.* NPG Asia Materials, vol. 15, no. 1, page 27, 2023. (Cited on page 1.)

[Liu 2024] Jiang Liu, Yongcai He, Lei Ding, Hua Zhang, Qiaoyan Li, Lingbo Jia, Jia Yu, Ting Wai Lau, Minghui Li, Yuan Qin*et al.* *Perovskite/silicon tandem solar cells with bilayer interface passivation.* Nature, vol. 635, no. 8039, pages 596–603, 2024. (Cited on page 2.)

[Lu 2020] Haipeng Lu, Chuanxiao Xiao, Ruyi Song, Tianyang Li, Annalise E Maughan, Andrew Levin, Roman Brunecky, Joseph J Berry, David B Mitzi, Volker Blum*et al.* *Highly distorted chiral two-dimensional tin iodide perovskites for spin polarized charge transport.* Journal of the American Chemical Society, vol. 142, no. 30, pages 13030–13040, 2020. (Cited on page 12.)

[Ma 2023] Fei Ma, Yang Zhao, Zihan Qu and Jingbi You. *Developments of highly efficient perovskite solar cells.* Accounts of Materials Research, vol. 4, no. 8, pages 716–725, 2023. (Cited on page 1.)

[Mao 2018a] Lingling Mao, Weijun Ke, Laurent Pedesseau, Yilei Wu, Claudine Katan, Jacky Even, Michael R Wasielewski, Constantinos C Stoumpos and Mercouri G Kanatzidis. *Hybrid Dion–Jacobson 2D lead iodide perovskites.* Journal of the American Chemical Society, vol. 140, no. 10, pages 3775–3783, 2018. (Cited on page 7.)

[Mao 2018b] Lingling Mao, Constantinos C Stoumpos and Mercouri G Kanatzidis. *Two-dimensional hybrid halide perovskites: principles and promises.* Journal of the American Chemical Society, vol. 141, no. 3, pages 1171–1190, 2018. (Cited on page 6.)

[Matsushima 2016] Toshinori Matsushima, Sunbin Hwang, AS Sandanayaka, Chuanjiang Qin, Shinobu Terakawa, Takashi Fujihara, Masayuki Yahiro and Chihaya Adachi. *Solution-Processed Organic-Inorganic Perovskite Field-Effect Transistors with High Hole Mobilities.* Advanced Materials (Deerfield Beach, Fla.), vol. 28, no. 46, pages 10275–10281, 2016. (Cited on page 3.)

[Meltzer 2005] RS Meltzer. *Line broadening mechanisms and their measurement.* In Spectroscopic properties of rare earths in optical materials, pages 191–265. Springer, 2005. (Cited on page 56.)

[Menahem 2021] Matan Menahem, Zhenbang Dai, Sigalit Aharon, Rituraj Sharma, Maor Asher, Yael Diskin-Posner, Roman Korobko, Andrew M Rappe and Omer Yaffe. *Strongly anharmonic octahedral tilting in two-dimensional hybrid halide perovskites.* ACS Nano, vol. 15, no. 6, pages 10153–10162, 2021. (Cited on page 12.)

[Min 2018] Kathy Kyaw Min, Phyoe Sandar Win, Hla Myo Tun, Zaw Min Naing and Win Khaing Moe. *Photoluminescence and Lifetime Measurement for the Excitation and Temperature Dependence of Carrier Relaxation in III-V Semiconductors.* Materials Science, 2018. (Cited on page 40.)

[Mitzi 2001] David B Mitzi. *Templating and structural engineering in organic–inorganic perovskites.* Journal of the Chemical Society, Dalton Transactions, no. 1, pages 1–12, 2001. (Cited on pages 5 and 11.)

[Miura 2007] Noboru Miura. Physics of semiconductors in high magnetic fields, volume 15. OUP Oxford, 2007. (Cited on pages 31 and 78.)

[Molas 2017] Maciej R Molas, Clement Faugeras, Autur O Slobodeniuk, Karol Nogajewski, Miroslav Bartos, DM Basko and Marek Potemski. *Brightening of dark excitons in monolayers of semiconducting transition metal dichalcogenides.* 2D Materials, vol. 4, no. 2, page 021003, 2017. (Cited on pages 32 and 63.)

[Møller 1957] Chr Kn Møller. *A phase transition in cæsium plumbochloride.* Nature, vol. 180, no. 4593, pages 981–982, 1957. (Cited on page 25.)

[Momma 2011] Koichi Momma and Fujio Izumi. *VESTA 3 for three-dimensional visualization of crystal, volumetric and morphology data.* Journal of Applied Crystallography, vol. 44, no. 6, pages 1272–1276, 2011. (Cited on pages 4, 7, 12 and 35.)

[Moore 1996] WJ Moore and RT Holm. *Infrared dielectric constant of gallium arsenide.* Journal of Applied Physics, vol. 80, no. 12, pages 6939–6942, 1996. (Cited on page 21.)

[Moseley 2021] Oliver DI Moseley, Tiarnan AS Doherty, Richard Parmee, Miguel Anaya and Samuel D Stranks. *Halide perovskites scintillators: unique promise and current limitations.* Journal of Materials Chemistry C, vol. 9, no. 35, pages 11588–11604, 2021. (Cited on page 1.)

[Mott 1938] NF Mott. *Conduction in polar crystals. II. The conduction band and ultra-violet absorption of alkali-halide crystals.* Transactions of the Faraday Society, vol. 34, pages 500–506, 1938. (Cited on page 14.)

[Movilla 2023] Jose L Movilla, Josep Planelles and Juan I Climente. *Excitons in metal halide perovskite nanoplatelets: an effective mass description of polaronic, dielectric and quantum confinement effects.* Nanoscale Advances, vol. 5, no. 22, pages 6093–6101, 2023. (Cited on page 22.)

[Munson 2018] Kyle T Munson, Eric R Kennehan, Grayson S Doucette and John B Asbury. *Dynamic disorder dominates delocalization, transport, and recombination in halide perovskites.* Chem, vol. 4, no. 12, pages 2826–2843, 2018. (Cited on page 21.)

[Nestoklon 2018] MO Nestoklon, SV Goupalov, RI Dzhioev, OS Ken, VL Korenev, Yu G Kusrayev, VF Sapega, Chris de Weerd, Leyre Gomez, Tom Gregorkiewicz*et al.* *Optical orientation and alignment of excitons in ensembles of inorganic perovskite nanocrystals.* Physical Review B, vol. 97, no. 23, page 235304, 2018. (Cited on page 75.)

[Nestoklon 2023] Mikhail O Nestoklon, Erik Kirstein, Dmitri R Yakovlev, Evgeny A Zhukov, Mikhail M Glazov, Marina A Semina, Eugeniyus L Ivchenko, Elena V Kolobkova, Maria S Kuznetsova and Manfred Bayer. *Tailoring the electron and hole Landé factors in lead halide perovskite nanocrystals by quantum confinement and halide exchange.* Nano Letters, vol. 23, no. 17, pages 8218–8224, 2023. (Cited on page 80.)

[Ni 2017] Limeng Ni, Uyen Huynh, Alexandre Cheminal, Tudor H Thomas, Ravichandran Shivanna, Ture F Hinrichsen, Shahab Ahmad, Aditya Sadhanala and Akshay Rao. *Real-time observation of exciton–phonon coupling* *dynamics in self-assembled hybrid perovskite quantum wells.* ACS Nano, vol. 11, no. 11, pages 10834–10843, 2017. (Cited on page 12.)

[Niu 2014] Wendy Niu, Anna Eiden, G Vijaya Prakash and Jeremy J Baumberg. *Exfoliation of self-assembled 2D organic-inorganic perovskite semiconductors.* Applied Physics Letters, vol. 104, no. 17, 2014. (Cited on page 8.)

[Optics] Edmund Optics. *Understanding Waveplates and Retarders.* (Cited on pages 47 and 48.)

[Otero-Martínez 2022] Clara Otero-Martínez, Junzhi Ye, Jooyoung Sung, Isabel Pastoriza-Santos, Jorge Pérez-Juste, Zhiguo Xia, Akshay Rao, Robert LZ Hoye and Lakshminarayana Polavarapu. *Colloidal metal-halide perovskite nanoplatelets: thickness-controlled synthesis, properties, and application in light-emitting diodes.* Advanced Materials, vol. 34, no. 10, page 2107105, 2022. (Cited on page 10.)

[Ou 2019] Qingdong Ou, Xiaozhi Bao, Yinan Zhang, Huaiyu Shao, Guichuan Xing, Xiangping Li, Liyang Shao and Qiaoliang Bao. *Band structure engineering in metal halide perovskite nanostructures for optoelectronic applications.* Nano Materials Science, vol. 1, no. 4, pages 268–287, 2019. (Cited on pages 2, 8 and 9.)

[O'donnell 1991] Kevin P O'donnell and Xie Chen. *Temperature dependence of semiconductor band gaps.* Applied Physics Letters, vol. 58, no. 25, pages 2924–2926, 1991. (Cited on page 52.)

[Paritmongkol 2019] Watcharaphol Paritmongkol, Nabeel S Dahod, Alexia Stollmann, Nannan Mao, Charles Settens, Shao-Liang Zheng and William A Tisdale. *Synthetic variation and structural trends in layered two-dimensional alkylammonium lead halide perovskites.* Chemistry of Materials, vol. 31, no. 15, pages 5592–5607, 2019. (Cited on pages 11, 36 and 37.)

[Pedesseau 2016] Laurent Pedesseau, Daniel Sapori, Boubacar Traore, Roberto Robles, Hong-Hua Fang, Maria Antonietta Loi, Hsinhan Tsai, Wanyi Nie, Jean-Christophe Blancon, Amanda Neukirch*et al. Advances and promises of layered halide hybrid perovskite semiconductors.* ACS Nano, vol. 10, no. 11, pages 9776–9786, 2016. (Cited on pages 3, 12 and 22.)

[Peksa 2024] Paulina Peksa, Arthur Maufort, Michał Baranowski, Alessandro Surrente, Laurence Lutsen, Paulina Płochocka, Wouter TM Van Gompel and Mateusz Dyksik. *Engineering the Effective Mass in 2D Perovskites via Octahedral Distortion.* The Journal of Physical Chemistry C, vol. 128, no. 42, pages 17984–17989, 2024. (Cited on page 12.)

[Pelant 2012] Ivan Pelant and Jan Valenta. Luminescence spectroscopy of semiconductors. OUP Oxford, 2012. (Cited on page 41.)

[Peng 2017] Wei Peng, Jun Yin, Kang-Ting Ho, Olivier Ouellette, Michele De Bastiani, Banavoth Murali, Omar El Tall, Chao Shen, Xiaohe Miao, Jun Pan*et al.* *Ultralow self-doping in two-dimensional hybrid perovskite single crystals.* Nano letters, vol. 17, no. 8, pages 4759–4767, 2017. (Cited on page 36.)

[Philippe 2015] Bertrand Philippe, Byung-Wook Park, Rebecka Lindblad, Johan Oscarsson, Sareh Ahmadi, Erik MJ Johansson and Hakan Rensmo. *Chemical and Electronic Structure Characterization of Lead Halide Perovskites and Stability Behavior under Different Exposures – A Photoelectron Spectroscopy Investigation.* Chemistry of Materials, vol. 27, no. 5, pages 1720–1731, 2015. (Cited on page 5.)

[Plumhof 2012] Johannes D Plumhof, Rinaldo Trotta, Armando Rastelli and Oliver G Schmidt. *Experimental methods of post-growth tuning of the excitonic fine structure splitting in semiconductor quantum dots.* Nanoscale Research Letters, vol. 7, pages 1–11, 2012. (Cited on page 25.)

[Poglitsch 1987] Albrecht Poglitsch and Daniel Weber. *Dynamic disorder in methylammoniumtrihalogenoplumbates (II) observed by millimeter-wave spectroscopy.* The Journal of Chemical Physics, vol. 87, no. 11, pages 6373–6378, 1987. (Cited on pages 9 and 25.)

[Pollmann 1977] J Pollmann and H Büttner. *Effective Hamiltonians and bindings energies of Wannier excitons in polar semiconductors.* Physical Review B, vol. 16, no. 10, page 4480, 1977. (Cited on page 22.)

[Posmyk 2022] Katarzyna Posmyk, Natalia Zawadzka, Mateusz Dyksik, Alessandro Surrente, Duncan K Maude, Tomasz Kazimierczuk, Adam Babinski, Maciej R Molas, Watcharaphol Paritmongkol, Mirosław Maczka*et al.* *Quantification of exciton fine structure splitting in a two-dimensional perovskite compound.* The Journal of Physical Chemistry Letters, vol. 13, no. 20, pages 4463–4469, 2022. (Cited on pages 26 and 39.)

[Posmyk 2024a] Katarzyna Posmyk, Mateusz Dyksik, Alessandro Surrente, Duncan K Maude, Natalia Zawadzka, Adam Babiński, Maciej R Molas, Watcharaphol Paritmongkol, Mirosław Mączka, William A Tisdale*et al.* *Exciton Fine Structure in 2D Perovskites: The Out-of-Plane Excitonic State.* Advanced Optical Materials, vol. 12, no. 8, page 2300877, 2024. (Cited on pages 26, 29, 31, 46 and 71.)

[Posmyk 2024b] Katarzyna Posmyk, Natalia Zawadzka, Lucja Kipczak, Mateusz Dyksik, Alessandro Surrente, Duncan K Maude, Tomasz Kazimierczuk, Adam Babinski, Maciej R Molas, Wakul Bumrungsan*et al.* *Bright Excitonic Fine Structure in Metal-Halide Perovskites: From Two-Dimensional to Bulk.* Journal of the American Chemical Society, vol. 146, no. 7, pages 4687–4694, 2024. (Cited on pages 38, 72 and 79.)

[Protesescu 2015] Loredana Protesescu, Sergii Yakunin, Maryna I Bodnarchuk, Franziska Krieg, Riccarda Caputo, Christopher H Hendon, Ruo Xi Yang, Aron Walsh and Maksym V Kovalenko. *Nanocrystals of cesium lead halide perovskites (CsPbX$_3$, X= Cl, Br, and I): novel optoelectronic materials showing bright emission with wide color gamut.* Nano Letters, vol. 15, no. 6, pages 3692–3696, 2015. (Cited on pages 3 and 10.)

[Quan 2016] Li Na Quan, Mingjian Yuan, Riccardo Comin, Oleksandr Voznyy, Dong Ha Kim and Edward H Sargent. *Quasi-2D perovskites for efficient solar cells and LEDs.* SPIE Newsroom, 2016. (Cited on page 35.)

[Quarti 2020] Claudio Quarti, Claudine Katan and Jacky Even. *Physical properties of bulk, defective, 2D and 0D metal halide perovskite semiconductors from a symmetry perspective.* Journal of Physics: Materials, vol. 3, no. 4, page 042001, 2020. (Cited on pages 12 and 26.)

[Quarti 2024] Claudio Quarti, Giacomo Giorgi, Claudine Katan, Jacky Even and Maurizia Palummo. *Exciton ground state fine structure and excited states landscape in layered halide perovskites from combined BSE simulations and symmetry analysis.* Advanced Optical Materials, vol. 12, no. 8, page 2202801, 2024. (Cited on pages 12, 23, 26, 33, 60, 65 and 67.)

[Ramade 2018] Julien Ramade, Léon Marcel Andriambariarijaona, Violette Steinmetz, Nicolas Goubet, Laurent Legrand, Thierry Barisien, Frédérick Bernardot, Christophe Testelin, Emmanuel Lhuillier, Alberto Bramati*et al.* *Fine structure of excitons and electron–hole exchange energy in polymorphic CsPbBr$_3$ single nanocrystals.* Nanoscale, vol. 10, no. 14, pages 6393–6401, 2018. (Cited on page 75.)

[Rong 2018] Yaoguang Rong, Yue Hu, Anyi Mei, Hairen Tan, Makhsud I Saidaminov, Sang Il Seok, Michael D McGehee, Edward H Sargent and Hongwei Han. *Challenges for commercializing perovskite solar cells.* Science, vol. 361, no. 6408, page eaat8235, 2018. (Cited on page 1.)

[Ruddlesden 1957] SN Ruddlesden and PJAC Popper. *New compounds of the K$_2$NiF$_4$ type.* Acta Crystallographica, vol. 10, no. 8, pages 538–539, 1957. (Cited on page 6.)

[Ruddlesden 1958] SN Ruddlesden and Paul Popper. *The compound Sr$_3$Ti$_2$O$_7$ and its structure.* Acta Crystallographica, vol. 11, no. 1, pages 54–55, 1958. (Cited on page 6.)

[Rytova 2018] Natalia S Rytova. *Screened potential of a point charge in a thin film.* arXiv preprint arXiv:1806.00976, 2018. (Cited on page 19.)

[Schilcher 2021] Maximilian J Schilcher, Paul J Robinson, David J Abramovitch, Liang Z Tan, Andrew M Rappe, David R Reichman and David A Egger.

The significance of polarons and dynamic disorder in halide perovskites. ACS Energy Letters, vol. 6, no. 6, pages 2162–2173, 2021. (Cited on page 20.)

[Schlipf 2019] Johannes Schlipf, Yinghong Hu, Shambhavi Pratap, Lorenz Bießmann, Nuri Hohn, Lionel Porcar, Thomas Bein, Pablo Docampo and Peter Muller-Buschbaum. *Shedding light on the moisture stability of 3D/2D hybrid perovskite heterojunction thin films.* ACS Applied Energy Materials, vol. 2, no. 2, pages 1011–1018, 2019. (Cited on page 4.)

[Sendner 2016] Michael Sendner, Pabitra K Nayak, David A Egger, Sebastian Beck, Christian Müller, Bernd Epding, Wolfgang Kowalsky, Leeor Kronik, Henry J Snaith, Annemarie Pucci*et al.* *Optical phonons in methylammonium lead halide perovskites and implications for charge transport.* Materials Horizons, vol. 3, no. 6, pages 613–620, 2016. (Cited on page 21.)

[Sercel 2019] Peter C Sercel, John L Lyons, Darshana Wickramaratne, Roman Vaxenburg, Noam Bernstein and Alexander L Efros. *Exciton fine structure in perovskite nanocrystals.* Nano letters, vol. 19, no. 6, pages 4068–4077, 2019. (Cited on pages 26 and 33.)

[Sercel 2025] Peter C Sercel, Matthew P Hautzinger, Ruyi Song, Volker Blum and Matthew C Beard. *Optical activity of chiral excitons.* Advanced Materials, page 2415901, 2025. (Cited on page 56.)

[Singh 2007] Jasprit Singh. Electronic and optoelectronic properties of semiconductor structures. Cambridge University Press, 2007. (Cited on pages 17, 40, 41 and 52.)

[Smith 2014] Ian C Smith, Eric T Hoke, Diego Solis-Ibarra, Michael D McGehee and Hemamala I Karunadasa. *A layered hybrid perovskite solar-cell absorber with enhanced moisture stability.* Angewandte Chemie International Edition, vol. 53, no. 42, pages 11232–11235, 2014. (Cited on page 3.)

[Soe 2017] Chan Myae Myae Soe, Constantinos C Stoumpos, Mikaël Kepenekian, Boubacar Traoré, Hsinhan Tsai, Wanyi Nie, Binghao Wang, Claudine Katan, Ram Seshadri, Aditya D Mohite*et al.* *New type of 2D perovskites with alternating cations in the interlayer space,*$(C(NH_2)_3)(CH_3NH_3)_nPb_nI_{3n+1}$*: Structure, properties, and photovoltaic performance.* Journal of the American Chemical Society, vol. 139, no. 45, pages 16297–16309, 2017. (Cited on page 7.)

[Spina 2017] Massimo Spina, Ayat Karimi, Wanda Andreoni, Carlo A Pignedoli, Bálint Náfrádi, László Forró and Endre Horváth. *Mechanical signatures of degradation of the photovoltaic perovskite* $CH_3NH_3PbI_3$ *upon water vapor exposure.* Applied Physics Letters, vol. 110, no. 12, 2017. (Cited on page 3.)

[Srimath Kandada 2020] A. Ram Srimath Kandada and Carlos Silva. *Exciton Polarons in Two-Dimensional Hybrid Metal–Halide Perovskites.* The Journal of Physical Chemistry Letters, vol. 11, no. 1, pages 317–326, 2020. (Cited on page 56.)

[Steger 2022] Mark Steger, Svenja M Janke, Peter C Sercel, Bryon W Larson, Haipeng Lu, Xixi Qin, Victor Wen-zhe Yu, Volker Blum and Jeffrey L Blackburn. *On the optical anisotropy in 2D metal-halide perovskites.* Nanoscale, vol. 14, no. 3, pages 752–765, 2022. (Cited on page 26.)

[Stoumpos 2016] Constantinos C Stoumpos, Duyen H Cao, Daniel J Clark, Joshua Young, James M Rondinelli, Joon I Jang, Joseph T Hupp and Mercouri G Kanatzidis. *Ruddlesden–Popper hybrid lead iodide perovskite 2D homologous semiconductors.* Chemistry of Materials, vol. 28, no. 8, pages 2852–2867, 2016. (Cited on page 36.)

[Stoumpos 2017] Constantinos C Stoumpos, Chan Myae Myae Soe, Hsinhan Tsai, Wanyi Nie, Jean-Christophe Blancon, Duyen H Cao, Fangze Liu, Boubacar Traoré, Claudine Katan, Jacky Even*et al.* *High members of the 2D Ruddlesden-Popper halide perovskites: synthesis, optical properties, and solar cells of* $(CH_3(CH_2)_3NH_3)_2$ $(CH_3NH_3)_4Pb_5I_{16}$. Chem, vol. 2, no. 3, pages 427–440, 2017. (Cited on page 36.)

[Straus 2016] Daniel B Straus, Sebastian Hurtado Parra, Natasha Iotov, Julian Gebhardt, Andrew M Rappe, Joseph E Subotnik, James M Kikkawa and Cherie R Kagan. *Direct observation of electron–phonon coupling and slow vibrational relaxation in organic–inorganic hybrid perovskites.* Journal of the American Chemical Society, vol. 138, no. 42, pages 13798–13801, 2016. (Cited on page 12.)

[Sun 2023] Yuqi Sun, Lishuang Ge, Linjie Dai, Changsoon Cho, Jordi Ferrer Orri, Kangyu Ji, Szymon J Zelewski, Yun Liu, Alessandro J Mirabelli, Youcheng Zhang*et al.* *Bright and stable perovskite light-emitting diodes in the near-infrared range.* Nature, vol. 615, no. 7954, pages 830–835, 2023. (Cited on page 1.)

[Sutherland 2016] Brandon R Sutherland and Edward H Sargent. *Perovskite photonic sources.* Nature Photonics, vol. 10, no. 5, pages 295–302, 2016. (Cited on page 9.)

[Tamarat 2019] Philippe Tamarat, Maryna I Bodnarchuk, Jean-Baptiste Trebbia, Rolf Erni, Maksym V Kovalenko, Jacky Even and Brahim Lounis. *The ground exciton state of formamidinium lead bromide perovskite nanocrystals is a singlet dark state.* Nature Materials, vol. 18, no. 7, pages 717–724, 2019. (Cited on pages 26, 33 and 71.)

[Tan 2016] Zhenjun Tan, Yue Wu, Hao Hong, Jianbo Yin, Jincan Zhang, Li Lin, Mingzhan Wang, Xiao Sun, Luzhao Sun, Yucheng Huang*et al.* *Two-dimensional* $(C_4H_9NH_3)_2PbBr_4$ *perovskite crystals for high-performance* *photodetector*. Journal of the American Chemical Society, vol. 138, no. 51, pages 16612–16615, 2016. (Cited on page 3.)

[Tanaka 2005] Kenichiro Tanaka, Takayuki Takahashi, Takashi Kondo, Kenichi Umeda, Kazuhiro Ema, Tsutomu Umebayashi, Keisuke Asai, Kazuhito Uchida and Noboru Miura. *Electronic and excitonic structures of inorganic–organic perovskite-type quantum-well crystal* $(C_4H_9NH_3)_2PbBr_4$. Japanese Journal of Applied Physics, vol. 44, no. 8R, page 5923, 2005. (Cited on pages 12, 13, 26, 33, 56 and 67.)

[Tao 2021] Weijian Tao, Chi Zhang, Qiaohui Zhou, Yida Zhao and Haiming Zhu. *Momentarily trapped exciton polaron in two-dimensional lead halide perovskites*. Nature Communications, vol. 12, no. 1, page 1400, 2021. (Cited on page 72.)

[Thomson 2018] Stuart Thomson. *Observing phase transitions in a halide perovskite using temperature dependent photoluminescence spectroscopy*. Livingston: Edinburgh Instruments, AN_P45, 2018. (Cited on page 10.)

[Thorlabs] Thorlabs. *Choosing a Wave Plate*. (Cited on page 47.)

[Tian 2024] Ruijia Tian, Shujing Zhou, Yuanyuan Meng, Chang Liu and Ziyi Ge. *Material and device design of flexible perovskite solar cells for next-generation power supplies*. Advanced Materials, page 2311473, 2024. (Cited on page 2.)

[Umebayashi 2003] T Umebayashi, K Asai, T Kondo and AJPRB Nakao. *Electronic structures of lead iodide based low-dimensional crystals*. Physical Review B, vol. 67, no. 15, page 155405, 2003. (Cited on page 13.)

[Urban 2020] Joanna M Urban, Gabriel Chehade, Mateusz Dyksik, Matan Menahem, Alessandro Surrente, Gaëlle Trippé-Allard, Duncan K Maude, Damien Garrot, Omer Yaffe, Emmanuelle Deleporte*et al. Revealing excitonic phonon coupling in* $(PEA)_2(MA)_{n-1}Pb_nI_{3n+1}$ *2D layered perovskites*. The journal of physical chemistry letters, vol. 11, no. 15, pages 5830–5835, 2020. (Cited on pages 59, 66, 77 and 78.)

[Vasileiadou 2021a] Eugenia S Vasileiadou, Ido Hadar, Mikael Kepenekian, Jacky Even, Qing Tu, Christos D Malliakas, Daniel Friedrich, Ioannis Spanopoulos, Justin M Hoffman, Vinayak P Dravid*et al. Shedding light on the stability and structure–property relationships of two-dimensional hybrid lead bromide perovskites*. Chemistry of Materials, vol. 33, no. 13, pages 5085–5107, 2021. (Cited on page 5.)

[Vasileiadou 2021b] Eugenia S Vasileiadou, Bin Wang, Ioannis Spanopoulos, Ido Hadar, Alexandra Navrotsky and Mercouri G Kanatzidis. *Insight on the stability of thick layers in 2D Ruddlesden–Popper and Dion–Jacobson lead* *iodide perovskites.* Journal of the American Chemical Society, vol. 143, no. 6, pages 2523–2536, 2021. (Cited on page 5.)

[Wang 2020] Qixing Wang, Qi Zhang, Xin Luo, Junyong Wang, Rui Zhu, Qijie Liang, Lei Zhang, Justin Zhou Yong, Calvin Pei Yu Wong, Goki Eda*et al.* *Optoelectronic properties of a van der Waals WS_2 monolayer/2D perovskite vertical heterostructure.* ACS Applied Materials & Interfaces, vol. 12, no. 40, pages 45235–45242, 2020. (Cited on page 8.)

[Wannier 1937] Gregory H Wannier. *The structure of electronic excitation levels in insulating crystals.* Physical Review, vol. 52, no. 3, page 191, 1937. (Cited on page 14.)

[Wei 2014] Yi Wei, Pierre Audebert, Laurent Galmiche, Jean-Sébastien Lauret and Emmanuelle Deleporte. *Photostability of 2D organic-inorganic hybrid perovskites.* Materials, vol. 7, no. 6, pages 4789–4802, 2014. (Cited on page 35.)

[Weidman 2016] Mark C Weidman, Michael Seitz, Samuel D Stranks and William A Tisdale. *Highly tunable colloidal perovskite nanoplatelets through variable cation, metal, and halide composition.* ACS Nano, vol. 10, no. 8, pages 7830–7839, 2016. (Cited on page 10.)

[Whitfield 2016] PS Whitfield, N Herron, WE Guise, K Page, YQ Cheng, I Milas and MK Crawford. *Structures, phase transitions and tricritical behavior of the hybrid perovskite methyl ammonium lead iodide.* Scientific Reports, vol. 6, no. 1, page 35685, 2016. (Cited on pages 9, 10 and 12.)

[Wibowo 2023] Arie Wibowo, Md Abdul Kuddus Sheikh, Lina Jaya Diguna, Muhammad Bagas Ananda, Maradhana Agung Marsudi, Arramel Arramel, Shuwen Zeng, Liang Jie Wong and Muhammad Danang Birowosuto. *Development and challenges in perovskite scintillators for high-resolution imaging and timing applications.* Communications Materials, vol. 4, no. 1, page 21, 2023. (Cited on page 1.)

[Williams 1990] RT Williams and KS Song. *The self-trapped exciton.* Journal of Physics and Chemistry of Solids, vol. 51, no. 7, pages 679–716, 1990. (Cited on page 21.)

[Wright 2016] Adam D Wright, Carla Verdi, Rebecca L Milot, Giles E Eperon, Miguel A Pérez-Osorio, Henry J Snaith, Feliciano Giustino, Michael B Johnston and Laura M Herz. *Electron–phonon coupling in hybrid lead halide perovskites.* Nature Communications, vol. 7, no. 1, page 11755, 2016. (Cited on page 3.)

[Wygant 2019] Bryan R Wygant, Alexandre Z Ye, Andrei Dolocan, Quyen Vu, David M Abbot and C Buddie Mullins. *Probing the degradation chemistry and enhanced stability of 2D organolead halide perovskites.* Journal of the American Chemical Society, vol. 141, no. 45, pages 18170–18181, 2019. (Cited on pages 4, 5 and 12.)

[Xing 2024] Shiyu Xing, Yucai Yuan, Gan Zhang, Shiang Zhang, Yaxiao Lian, Weidong Tang, Ke Zhou, Shengnan Liu, Yuxiang Gao, Zhixiang Ren*et al. Energy-efficient perovskite LEDs with Rec. 2020 compliance.* ACS Energy Letters, vol. 9, no. 8, pages 3643–3651, 2024. (Cited on page 1.)

[Xiong 2023] Wentao Xiong, Chen Zou, Weidong Tang, Shiyu Xing, Zhaoyi Wang, Baodan Zhao and Dawei Di. *Efficient and bright blue perovskite LEDs enabled by a carbazole-phosphonic acid interface.* ACS Energy Letters, vol. 8, no. 7, pages 2897–2903, 2023. (Cited on pages 1 and 2.)

[Yang 1991] XL Yang, SH Guo, FT Chan, KW Wong and WY Ching. *Analytic solution of a two-dimensional hydrogen atom. I. Nonrelativistic theory.* Physical Review A, vol. 43, no. 3, page 1186, 1991. (Cited on page 18.)

[Yang 2017] Zhuo Yang, Alessandro Surrente, Krzysztof Galkowski, Atsuhiko Miyata, Oliver Portugall, RJ Sutton, AA Haghighirad, HJ Snaith, DK Maude, P Plochocka and RJ Nicholas. *Impact of the halide cage on the electronic properties of fully inorganic cesium lead halide perovskites.* ACS Energy Letters, vol. 2, no. 7, pages 1621–1627, 2017. (Cited on page 27.)

[Yang 2018] Yi Yang, Fei Gao, Shiwu Gao and Su-Huai Wei. *Origin of the stability of two-dimensional perovskites: a first-principles study.* Journal of Materials Chemistry A, vol. 6, no. 30, pages 14949–14955, 2018. (Cited on page 5.)

[Yang 2019] Arky Yang, Jean-Christophe Blancon, Wei Jiang, Hao Zhang, Joeson Wong, Ellen Yan, Yi-Rung Lin, Jared Crochet, Mercouri G Kanatzidis, Deep Jariwala*et al. Giant enhancement of photoluminescence emission in* WS_2*-two-dimensional perovskite heterostructures.* Nano Letters, vol. 19, no. 8, pages 4852–4860, 2019. (Cited on page 8.)

[Yang 2023] Xiaoyu Yang, Li Ma, Maotao Yu, Hao-Hsin Chen, Yongqiang Ji, An Hu, Qixuan Zhong, Xiaohan Jia, Yanju Wang, Yuzhuo Zhang*et al. Focus on perovskite emitters in blue light-emitting diodes.* Light: Science & Applications, vol. 12, no. 1, page 177, 2023. (Cited on page 1.)

[Yin 2017] Chunyang Yin, Liyang Chen, Nan Song, Yan Lv, Fengrui Hu, Chun Sun, William W Yu, Chunfeng Zhang, Xiaoyong Wang, Yu Zhang*et al. Bright-exciton fine-structure splittings in single perovskite nanocrystals.* Physical Review Letters, vol. 119, no. 2, page 026401, 2017. (Cited on page 75.)

[Yu 2010] Peter Yu and Manuel Cardona. Fundamentals of semiconductors: physics and materials properties. Springer Science & Business Media, 2010. (Cited on pages 15, 16, 21, 40, 41, 42 and 52.)

[Yu 2016] ZG Yu. *Effective-mass model and magneto-optical properties in hybrid perovskites.* Scientific Reports, vol. 6, no. 1, page 28576, 2016. (Cited on pages 23, 27, 28, 32, 48, 64 and 65.)

[Yuan 2016] Mingjian Yuan, Li Na Quan, Riccardo Comin, Grant Walters, Randy Sabatini, Oleksandr Voznyy, Sjoerd Hoogland, Yongbiao Zhao, Eric M Beauregard, Pongsakorn Kanjanaboos*et al. Perovskite energy funnels for efficient light-emitting diodes.* Nature Nanotechnology, vol. 11, no. 10, pages 872–877, 2016. (Cited on page 3.)

[Zhai 2017] Yaxin Zhai, Sangita Baniya, Chuang Zhang, Junwen Li, Paul Haney, Chuan-Xiang Sheng, Eitan Ehrenfreund and Zeev Valy Vardeny. *Giant Rashba splitting in 2D organic-inorganic halide perovskites measured by transient spectroscopies.* Science Advances, vol. 3, no. 7, page e1700704, 2017. (Cited on page 35.)

[Zhang 2009] Sanjun Zhang, Gaëtan Lanty, Jean-Sébastien Lauret, Emmanuelle Deleporte, Pierre Audebert and Laurent Galmiche. *Synthesis and optical properties of novel organic–inorganic hybrid nanolayer structure semiconductors.* Acta Materialia, vol. 57, no. 11, pages 3301–3309, 2009. (Cited on pages 32 and 35.)

[Zhang 2017] Xiao-Xiao Zhang, Ting Cao, Zhengguang Lu, Yu-Chuan Lin, Fan Zhang, Ying Wang, Zhiqiang Li, James C Hone, Joshua A Robinson, Dmitry Smirnov*et al. Magnetic brightening and control of dark excitons in monolayer* WSe_2. Nature nanotechnology, vol. 12, no. 9, pages 883–888, 2017. (Cited on pages 63 and 64.)

[Zhao 2022] Xiaoming Zhao, Tianran Liu and Yueh-Lin Loo. *Advancing 2D perovskites for efficient and stable solar cells: challenges and opportunities.* Advanced Materials, vol. 34, no. 3, page 2105849, 2022. (Cited on page 5.)

[Zheleva 1994] Tsvetanka Zheleva, K Jagannadham and J Narayan. *Epitaxial growth in large-lattice-mismatch systems.* Journal of Applied Physics, vol. 75, no. 2, pages 860–871, 1994. (Cited on page 2.)

[Zhu 2015] X-Y Zhu and V Podzorov. *Charge carriers in hybrid organic–inorganic lead halide perovskites might be protected as large polarons.* The Journal of Physical Chemistry Letters, vol. 6, no. 23, pages 4758–4761, 2015. (Cited on page 21.)

[Zhu 2020] Xudan Zhu, Junbo He, Rongjun Zhang, Chunxiao Cong, Yuxiang Zheng, Hao Zhang, Shanwen Zhang and Liangyao Chen. *Effects of dielectric screening on the excitonic and critical points properties of* WS_2/MoS_2 *heterostructures.* Nanoscale, vol. 12, no. 46, pages 23732–23739, 2020. (Cited on page 19.)

[Zuri 2023] Shahar Zuri, Arthur Shapiro, Leeor Kronik and Efrat Lifshitz. *Uncovering multiple intrinsic chiral phases in* $(PEA)_2PbI_4$ *halide perovskites.* The Journal of Physical Chemistry Letters, vol. 14, no. 21, pages 4901–4907, 2023. (Cited on page 72.)